

© 2011 by ADITYA AVINASH PARANJAPE.

DYNAMICS AND CONTROL OF ROBOTIC AIRCRAFT WITH ARTICULATED
WINGS

BY

ADITYA AVINASH PARANJAPE

DISSERTATION

Submitted in partial fulfillment of the requirements
for the degree of Doctor of Philosophy in Aerospace Engineering
in the Graduate College of the
University of Illinois at Urbana-Champaign, 2011

Urbana, Illinois

Doctoral Committee:

Assistant Professor Soon-Jo Chung, Director of Research and Chair
Professor Lawrence A. Bergman
Professor Emeritus Harry H. Hilton
Associate Professor Prashant G. Mehta
Associate Professor Michael S. Selig

Abstract

There is a considerable interest in developing robotic aircraft, inspired by birds, for a variety of missions covering reconnaissance and surveillance. Flapping wing aircraft concepts have been put forth in light of the efficiency of flapping flight at small scales. These aircraft are naturally equipped with the ability to rotate their wings about the root, a form of wing articulation. This thesis covers some problems concerning the performance, stability and control of robotic aircraft with articulated wings in gliding flight. Specifically, we are interested in aircraft without a vertical tail, which would then use wing articulation for longitudinal as well as lateral-directional control.

Although the dynamics and control of articulated wing aircraft share several common features with conventional fixed wing aircraft, the presence of wing articulation presents several unique benefits as well as limitations from the perspective of performance and control. One of the objective of this thesis is to understand these features using a combination of theoretical and numerical tools.

The aircraft concept envisioned in this thesis uses the wing dihedral angles for longitudinal and lateral-directional control. Aircraft with flexible articulated wings are also investigated. We derive a complete nonlinear model of the flight dynamics incorporating dynamic CG location and the changing moment of inertia. We show that symmetric dihedral configuration, along with a conventional horizontal tail, can be used to control flight speed and flight path angle independently of each other. This characteristic is very useful for initiating an efficient perching maneuver.

It is shown that wing dihedral angles alone can effectively regulate sideslip during rapid turns and generate a wide range of equilibrium turn rates while maintaining a constant flight speed and regulating sideslip. We compute the turning performance limitations that arise due to the use of wing dihedral for yaw control, and compare the steady state performance of rigid and flexible-winged aircraft. We present an intuitive but very useful notion, called the effective dihedral, which allows us to extend some of the stability and performance results derived for rigid aircraft to

flexible aircraft. In the process, we identify the extent of flexibility needed to induce substantial performance benefits, and conversely the extent to which results derived for rigid aircraft apply to a flexible aircraft. We demonstrate, interestingly enough, that wing flexibility actually causes a deterioration in the maximum achievable turn rate when the sideslip is regulated.

We also present experimental results which help demonstrate the capability of wing dihedral for control and for executing maneuvers such as slow, rapid descent and perching. Open loop as well as closed loop experiments are performed to demonstrate (a) the effectiveness of symmetric dihedral for flight path angle control, (b) yaw control using asymmetric dihedral, and (c) the elements of perching.

Using a simple order of magnitude analysis, we derive conditions under which the wing is structurally statically stable, as well as conditions under which there exists time scale separation between the bending and twisting dynamics. We show that the time scale separation depends on the geometry of the wing cross section, the Poisson's ratio of the wing material, the flight speed and the aspect ratio of the wing. We design independent control laws for bending and twisting. A key contribution of this thesis is the formulation of a partial differential equation (PDE) boundary control problem for wing deformation. PDE-backstepping is used to derive tracking and exponentially stabilizing boundary control laws for wing twist which ensure that a weighted integral of the wing twist (net lift or the rolling moment) tracks the desired time-varying reference input. We show that a control law which only ensures tracking of a weighted integral improves the stability margin of the twisting dynamics sixteen fold. A tracking control law is derived for the wing tip displacement which uses motion planning and a novel two-stage perturbation observer. This work on PDE-based control of wing deformation allows for the use of highly flexible wings on MAVs.

Put together, the thesis provides a comprehensive understanding of the flight dynamics of a robotic aircraft equipped with articulated wings, and provides a set of control laws for performing agile maneuvers and for honing the benefits of using highly flexible wings.

To my grandfather, who passed away 10 years ago. He would feel proud to see this thesis.

Acknowledgments

This project would not have been possible without the support of many people. Many thanks to my adviser, Soon-Jo Chung, for all that he has taught me over the last two years, read my numerous revisions patiently, and put up with my antics. During the last three years, I had the opportunity to work with Harry Hilton, Naira Hovakimyan, Michael Selig, Miroslav Krstic (UCSD), Animesh Chakravarthy (Wichita State University) and Vishwesh Kulkarni (U. Minnesota). I owe them much gratitude for all that I learned from them. I also thank my committee members, Lawrence Bergman and Prashant Mehta, for their guidance and for their insightful comments on this thesis. Dr. Narayan Ananthkrishnan, formerly from IIT Bombay, has been a constant source of wisdom - be it research or other worldly matters. I learned flight dynamics and control from him while I was an undergraduate student at IIT Bombay. I owe much of my interest and competence in these areas to his teachings. The same can be said about philosophy, spirituality, and scientific debate. He has been a Guru in the fullest (Sanskritic, for the lack of a better phrase) sense of this Sanskrit word whose usage in English leaves a lot to be desired. Finally, it is a pleasure to express my heartfelt gratitude to parents, family and friends, particularly my current and former lab mates, who endured me and always offered support, love and, when occasionally required, honest words of stern admonition.

Table of Contents

List of Tables	ix
List of Figures	x
List of Symbols	xiii
Chapter 1 Introduction	1
1.1 Literature Review	4
1.2 Main Contributions	6
1.2.1 Performance and Stability	6
1.2.2 Control	8
1.3 Tools for Modelling, Analysis and Control	9
1.4 Organization	10
Chapter 2 Equations of Motion for an Articulated Wing Aircraft	12
2.1 Notation	12
2.2 Coordinate Frames of Reference	12
2.3 Calculating the Velocity at a Spanwise Station	14
2.4 Aircraft Equations of Motion	15
2.4.1 Structural Dynamics	18
2.5 Fuselage Kinematics	19
2.6 Forces	20
2.7 Trim Equations	23
2.8 Specialization to a Rigid Aircraft	24
2.9 Aerodynamic Model for Trim Calculations	25
2.10 Chapter Summary	28
Chapter 3 Performance and Stability of a Rigid Aircraft	29
3.1 Comparison With the Vertical Tail	29
3.2 Theoretical Analysis of the Role of Wing Dihedral	32
3.2.1 Analytical Approximations to Lateral-Directional Stability	32
3.2.2 Lateral-Directional Stability	34
3.2.3 Control Effectiveness for Turning	35
3.3 Trim and Stability Analysis	37
3.3.1 Stability and Longitudinal Performance of Symmetric Configurations	37
3.3.2 Lateral Stability and Performance	40
3.3.3 Generalizations and Trade-Offs	47
3.4 Chapter Summary	49

Chapter 4 Performance and Stability of a Flexible Aircraft	50
4.1 Analysis of the Wing and Effective Dihedral	50
4.2 Feasibility of Using Wing Tension	51
4.3 Bending and Twist Natural Frequencies	54
4.4 Bifurcation Analysis of Turning Flight	55
4.4.1 Reduction in Sideslip (Variable $\theta_L; \theta_R = -\theta_L = -\theta_a; \delta_L = \delta_R$)	55
4.4.2 Coordinated Turn ($\theta_L = \theta_R = 0; \delta_L, \delta_R$ variable)	58
4.4.3 Discussion	60
4.5 Chapter Summary	60
Chapter 5 Experiments, Control Design and Perching	61
5.1 Experimental Setup	61
5.2 Open Loop Experimental Results	63
5.2.1 Symmetric Configuration	63
5.2.2 Lateral-Directional Motion	64
5.3 Control Law Design	65
5.3.1 Case for PI(D) Control	66
5.3.2 Simulations	69
5.3.3 Angle of Attack Control	69
5.3.4 Yaw Control by Asymmetric Wing Dihedral	72
5.3.5 Perching Guidance Loop	74
5.4 Closed Loop Experiments	75
5.4.1 Angle of Attack Control for Perching	75
5.4.2 Lateral-Directional Control for Perching	75
5.4.3 Flight Path Control for Perching	76
5.5 Perching	77
5.5.1 C_L for Perching	77
5.5.2 Experimental Demonstration of a Perching Maneuver	83
5.6 Use of Trailing Edge Flaps for Mitigating Control Effectiveness Problems	83
5.7 Chapter Summary	85
Chapter 6 PDE Boundary Control of Flexible Wings	88
6.1 Motivation	88
6.2 Problem Formulation	90
6.3 Boundary Control of Twisting Motion: Root Control	91
6.3.1 Boundary Condition when $H(t) \equiv H$	92
6.3.2 Backstepping for Regulation to a Steady State	93
6.3.3 Discussion	95
6.3.4 Local Linear Analysis	95
6.3.5 Lyapunov-based Analysis for Spatially-Varying $M(y)$	97
6.4 Tracking Controller for Twist	101
6.5 Boundary Control of Twisting Motion: Wing Tip Control	106
6.5.1 Tip Boundary Control when All Parameters are Known	106
6.5.2 Tracking and Stability	107
6.5.3 Adaptive Control for Wing Tip Actuator	108
6.5.4 Control of Rolling Moment	110
6.6 Root Boundary Control of Wing Bending	111

6.6.1	Time Scales of Wing Twist and Bending	112
6.6.2	Open Loop Stability of Bending	114
6.6.3	Perturbation Observer for Root Control of Bending	115
6.6.4	Motion Planning for the Homogeneous Component of the Observer ($\hat{\xi}_h$)	119
6.7	Simulations	120
6.8	Chapter Summary	123
Chapter 7	Conclusions and Open Problems	127
7.1	Conclusions	127
7.2	Future Work	128
References		129

List of Tables

3.1	Stability derivatives for a tailless aircraft with an articulated wing	33
3.2	Four cases considered in this section and their physical significance	40
5.1	Physical Properties of the MAV	62
5.2	A summary of the turning performance. The aileron deflection has been denoted by δ_a . The negative sign implies that the aircraft rolls to the left.	65

List of Figures

1.1	Figure (a) shows a robotic aircraft with flexible wings controlled at the wing root (by servo actuators) and the tip (by flaps). Figure (b) shows a robotic bat testbed where the control laws proposed in this thesis can be tested [42, 15].	2
1.2	Chart showing the organization of the thesis, with arrows denoting the flow of material and interconnections between the chapters.	11
2.1	A schematic of the aircraft showing the dimensions and the coordinate systems used to model the aircraft.	13
2.2	The figure on the left shows ParkZone®Vapor, the aircraft model used for numerical analysis. The size of the Vapor is similar to that of small birds such as the barn swallow shown on the right.	26
2.3	Experimentally obtained aerodynamic data [102].	27
3.1	Illustration of the physics underlying the use of dihedral as a control. The dark conspicuous dot in the figures is the aircraft CG.	30
3.2	Root locus plot showing lateral-directional eigenvalues as functions of the angle of attack for candidate symmetric wing dihedral deflections. The roll mode is not shown in the root locus plot. The real part of the right most eigenvalue is a measure of the stability margin when the system is stable.	34
3.3	Plots showing the sign of the control effectiveness, $\text{sign}\left(\frac{\Delta N}{\Delta(\delta_L - \delta_R)}\right)$, as a function of the angle of attack, roll rate and yaw rate.	36
3.4	Bifurcation diagrams showing γ and α versus symmetric dihedral (i.e., $\delta_R = \delta_L = \delta$), and the corresponding elevator deflection to hold the speed fixed at $V = 2.8$ m/s. An asterisk (*) denotes equilibria where eigenvalues with positive real parts are all real. Circles (\circ) denote equilibria where all eigenvalues with positive real parts have non-zero imaginary parts.	38
3.5	Simulated time history of the aircraft motion with the dihedral angle of both wings fixed at 10 deg. All lateral variables, namely the sidelip, roll rate, yaw rate and the Euler roll angle, were initialized at zero.	39
3.6	Case 1: Turn rate, sideslip and flight speed as functions of the anti-symmetric wing incidence. The wing dihedral angles were fixed at 29 deg.	41
3.7	Case 2: Coordinated turn trims as a function of anti-symmetric wing incidence. . . .	42
3.8	Case 3: Coordinated turn trims as functions of the left wing dihedral. The short arrow indicates a reference solution, while the long arrows track ω , V and δ_R as δ_L is varied. Points A, B, C and D are Hopf bifurcations.	44

3.9	Case 4: Coordinated turn trims with left and right wing dihedrals varied asymmetrically. Each plot carries two arrows. The short arrow denotes a reference solution, while the long arrow helps track the variation of the turn rate and δ_R starting from the reference solution.	45
3.10	3-D plot of the turn rate and the wing dihedral angles when the sideslip is held fixed at 0 and the flight speed at 3.0 m/s.	47
3.11	Turn rate as a function of anti-symmetric wing incidence with the constraints $\beta = 0$ and $V = 2.8$ m/s. Recall that asterisks '*' and empty circles 'o' denote equilibria where all eigenvalues with positive real parts are real and complex conjugate, respectively.	47
4.1	Effective dihedral as a function of the dihedral angle at the wing root for two different values of the Young's modulus. Each plot shows the effective dihedral for three values of wing tip twist (θ): 0, 0.1 rad and 0.2 rad. This plot was obtained for $V = 2.5$ m/s and $\alpha = 10$ deg.	52
4.2	Effect of tension on the effective dihedral. The curves corresponding to a tension of zero, 5 g., and 10 g. are plotted. This flight speeds was set to $V = 2.5$ m/s and the angle of attack was $\alpha = 10$ deg.	53
4.3	A comparison of the sideslip and turn rate as functions of anti-symmetric wing twist for otherwise identical airframes equipped with rigid and flexible wings. The wings have a Young's modulus of 5 MPa. The equilibria are marked with a red asterisk to denote that the Jacobian has a single positive real eigenvalue. In both cases, the dihedral angle at both wing roots was set to 25 deg. The flight speed was set to 2.8 m/s and the elevator was fixed at -11 deg and $\delta_L = \delta_R = 29$ deg (0.5 rad).	56
4.4	Turn rate and sideslip as functions of anti-symmetric wing twist when the $\delta_L = \delta_R = 0$. Blue circles denote equilibria where the Jacobian has a pair of complex conjugate eigenvalues with positive real parts, while pink dots denote equilibria where the Jacobian has three eigenvalues with positive real parts: one real and a complex conjugate pair. The Young's modulus was set to $E = 5$ MPa. The flight speed was set to 2.8 m/s. The elevator deflection was set to -11 deg.	57
4.5	A comparison of the turn rate as a function of the left wing dihedral angle, and the right wing dihedral angle required to maintain zero sideslip, for otherwise identical airframes equipped with rigid and flexible wings. In both cases, the elevator deflection was fixed at -11 deg, and $\theta_R = \theta_L = 0$. The flexible wings have a Young's modulus of 5 MPa. The Jacobian of equilibria marked by pink dots have three eigenvalues with positive real parts: one real and a complex conjugate pair. The flight speed and angle of attack are within the range of validity of the aerodynamic data.	59
5.1	The Plantraco Kolibri Pocket Plane, used for open loop experiments described in this chapter.	61
5.2	Representative configurations showing the asymmetric dihedral capability of the wings. The foam table on which the aircraft is resting is not part of the airframe.	63
5.3	Steady state values of the longitudinal flight parameters as functions of the wing dihedral.	64
5.4	Schematic of the controller, where χ denotes the aircraft heading.	66
5.5	Simulated time histories of the aircraft in a disturbance-free flight. A 12 deg (0.2 rad jump in the angle of attack, α , is commanded. The resulting disturbances are rejected by the control law.)	70

5.6	Simulated time histories of the aircraft in a persistent periodic lateral-directional disturbance field. A 12 deg (0.2 rad jump in the angle of attack, α , is commanded.)	71
5.7	Experimental results showing the longitudinal flight parameters. In particular, α settles down at the desired value within 2 s.	75
5.8	Experimental results showing the sideslip, velocity heading and the Euler angles measured during a yaw control test of the aircraft with a vertical tail. Parameters appear to be regulating during the short experiment	76
5.9	Snapshots showing an owl in various stages of a perching maneuver, from BBC's Life of Birds. The video was processed using Matlab.	78
5.10	Angle of attack, flight path angle and pitch angle measurements from the BBC video of a perching owl. The maneuver was completed at $t = 1.5$ s.	79
5.11	The C_L required for perching, starting with $V_0 = 5$ m/s for different values of γ_0 and x_f . The value of C_L has been calculated using Eq. (5.25). The arrow indicates the direction of increasing x_f	81
5.12	Perching trajectory, and time histories of state and control variables for a high drag configuration [62].	82
5.13	Flight parameters during a perching attempt that was triggered at 1.5m above the ground	84
5.14	Effect of using a TE flap, $0 \leq \delta_f \leq 10$ deg. The nondimensional control effectiveness, Non-dimensional $N_{\delta_{\text{asym}}} = C_L x_a / c + C_{m,ac}$	86
6.1	Figure showing the problems addressed in this chapter.	89
6.2	Block diagram showing the tracking controller for twist (θ) dynamics. This structure is identical to the classic strict feedback structure for systems described by ODEs [39].	105
6.3	Torsional divergence speed as a function of the Young's modulus of the wing. The blue curve is the open loop divergence speed, while the red curve is the divergence speed after adding the tip controller from section 6.5.	112
6.4	Block diagram for the perturbation observer coupled to the system dynamics. The control signal, $u(t)$, is generated from motion planning, while $R(t)$ is the desired reference signal from (6.7).	117
6.5	Regulation of the twist dynamics using the backstepping controller in equation (6.18), with the transformation in equations (6.15) and (6.17). The plots were obtained for $M/a = 8$, while p was increased to ensure stability. Each plot is a collection of snapshots, where the lines get darker with time.	122
6.6	Twist profile of the wing as a function of time when the adaptive controller in equation (6.73) is applied at the wing tip. Three cases have been examined here, with $\int_0^L \theta(t, y) dy = 0.05$ as the desired output. Each plot shows appropriately chosen snapshots, with lines getting darker with time.	124
6.7	Time histories of the error $e(t)$ and the control signal $u(t)$ for the case of spatially varying, unknown $M(y)$ with unstable open loop dynamics.	125
6.8	Time history of the wing tip displacement for two classes of reference signals: a pulse and a sine wave. The first two plots were obtained with the right hand side set to zero, while the third plot was obtained for a time varying $F(t, y)$ in equation (6.83). .	126

List of Symbols

b, c	wing span and chord length.
D, L, Y	drag, lift, and side force.
E, G	Young's modulus and modulus of rigidity of a material.
I_b, I_p, \tilde{J}	second moment of area about the in-plane axis along the direction of bending, polar moment of area, and torsional stiffness of a cross section of the wing.
$\mathbf{J}_R, \mathbf{J}_L, \mathbf{J}$	moment of inertia tensor of the right and left wings, and the aircraft body respectively, in the aircraft body frame.
\mathbf{J}_s	second moment of area of a cross section with components in the local wing station frame.
$\tilde{m}_R, \tilde{m}_L, m$	mass per unit span of the right and left wings, total mass of aircraft.
\mathbf{r}_{CG}	position vector of the aircraft center of gravity.
$S(\mathbf{p})\mathbf{q}$	cross product $\mathbf{p} \times \mathbf{q}$, where $\mathbf{p}, \mathbf{q} \in \mathbb{R}^3$.
T	axial tension in the wing.
\mathbf{T}_{FG}	rotation matrix from frame G to frame F.
$\mathbf{u}_B = (u \ v \ w)$	body axis aircraft wind velocity components.
$\mathbf{u}_f = (0 \ 0 \ \dot{\xi}_f)$	rate of change of bending displacement ξ_f in the local wing frame.
$\mathbf{V}(y), V(y), V_\infty$	local wind velocity vector, local wind speed, freestream speed.
(x_a, x_e)	distance of aerodynamic center and center of gravity from the twist axis at a given station along the wing span, and normalized with respect to c .
X, Y, Z	position of the aircraft in the ground frame.
X_A, Y_A, Z_A	body frame components of the aerodynamic force per unit span.
X_B, Y_B, Z_B	body frame components of the net aerodynamic and gravitational forces.

α, β	angle of attack and sideslip.
β_R, β_L	sweep angle of right and left wing.
γ, χ	flight path angle, wind axis heading angle.
δ_R, δ_L	right and left wing dihedral angles.
$\theta_R, \theta_L, \theta_a$	right and left wing root twist angles, anti-symmetric wing twist ($\theta_R = -\theta_L$).
$\theta_s(y)$	sectional wing twist from wing flexibility.
ϕ, θ, ψ	Euler angles.
ν	distance of flow separation point from the leading edge, measured along the wing chord.
ω	Turn rate ($\dot{\chi}$).
ρ_w	density of the wing.
$\boldsymbol{\omega}_B = (p \ q \ r)^T$	angular velocity of the airframe, body axis components (roll, pitch, yaw).
$\boldsymbol{\omega}_R, \boldsymbol{\omega}_L$	angular velocity of the wings about the root, body axis components.
$\boldsymbol{\omega}_s = (0 \ \dot{\theta}_s \ 0)$	twist rate of a wing station, components in the wing station frame.
Subscripts	
B	body.
R	wing root (used to denote a coordinate axis frame situated at the wing root).
s	wing station.

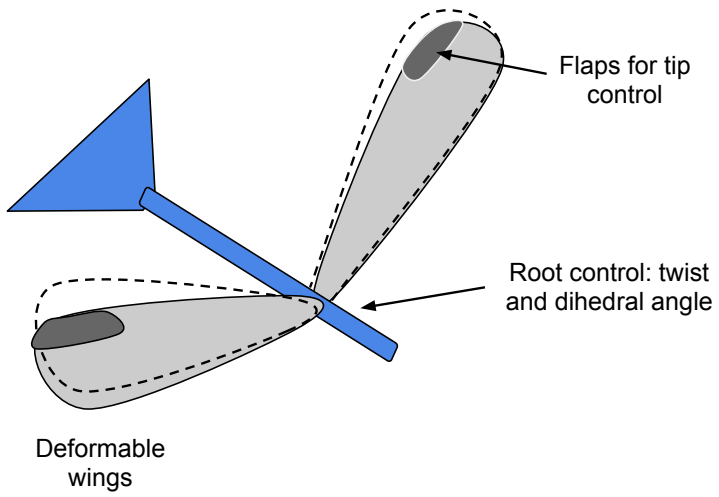
Chapter 1

Introduction

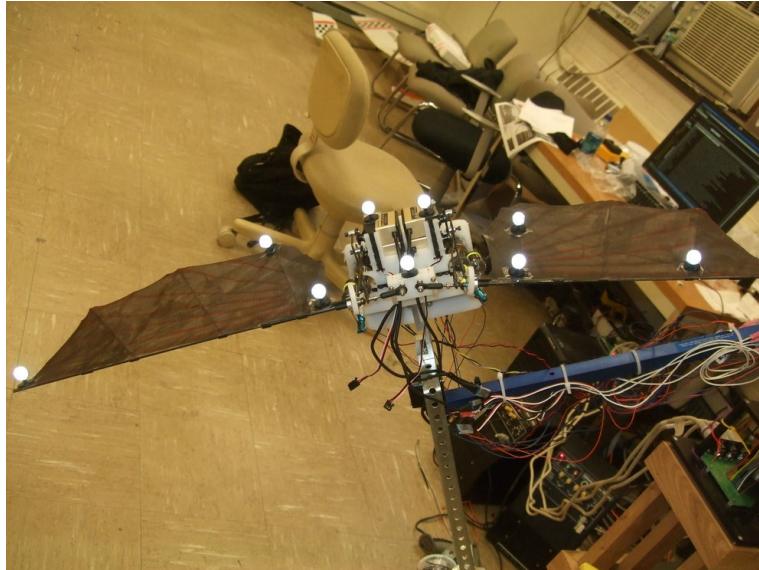
There is a considerable interest in developing robotic aircraft inspired by birds and bats [42, 15, 29] and insects [23, 21, 20, 109]. In contrast with insects whose wings are well modeled as simple rigid wings, both wing flexibility and wing articulation are believed to play a key role in flight performance and agility for bird and bat flight [94]. The broader goal is to learn and mimic avian flight with the ultimate objective of designing unmanned aerial vehicles which are autonomous, agile and capable of flying in constrained environments [56]. Birds are natural role models for designing robotic micro air vehicles (MAVs) wherein the aforementioned attributes can be engineered. MAVs typically fly in a low Reynolds number range of $10^3 - 10^5$ [53] which coincides with that of the birds. Therefore, it is worth investigating the mechanics of avian flight and making an attempt to reverse-engineer them. Conversely, a study of the flight mechanics of MAVs can shed light on several aspects of bird flight.

Birds lack a vertical tail. Instead, the wing dihedral and incidence angles are controlled actively as birds execute agile and even spatially constrained maneuvers. Birds are known to have a very complex wing structure, with a wide range of “actuators.” The wings can flap, twist and change the sweep angle on demand. They have a wide range of feathers which serve as flaps and spoilers. The hair on bird wings can sense local flow conditions, and feedback from these sensors is sent to the feathers which are, either passively or actively, oriented to optimize the flow conditions on the wing for stability and maneuverability.

Over-actuation to the extent seen in birds is difficult to engineer in aircraft because of well understood considerations such as weight penalty, actuator limitations, sensor design, etc. Therefore, it is necessary to abstract out the underlying phenomena and understand their implications for stability and control. That way, they can be engineered onto actual aircraft. This is the motivation behind this thesis.



(a) Robotic aircraft concept



(b) Robotic bat at UIUC

Figure 1.1: Figure (a) shows a robotic aircraft with flexible wings controlled at the wing root (by servo actuators) and the tip (by flaps). Figure (b) shows a robotic bat testbed where the control laws proposed in this thesis can be tested [42, 15].

This thesis contributes to the broader problem of developing a flapping MAV capable of agile flight in constrained environments, such as the conceptual MAV in Fig. 1.1(a). Chung and Dorothy

[15] studied a neurobiologically-inspired controller for flapping flight, and demonstrated it on a robotic testbed shown in Fig. 1.1(b). Their controller could switch in a stable and smooth fashion between flapping and gliding flight. Gliding is essential during soaring, landing and perching. This thesis aims to provide the analytical foundations for using wing articulation to perform agile maneuvers while gliding and landing.

Like any problem in flight mechanics and control, this thesis approaches the chosen problem along three directions: performance, stability and control. Each facet has been addressed in the thesis:

- Performance: we focus on steady state performance metrics such as the turn rate, gliding angle and speed. Turn rate is of particular interest because this performance metric would be most affected by the absence of a vertical tail. We also analyse the influence of wing flexibility on the performance metrics.
- Stability: we use bifurcation analysis to study the nature of stability of the turn and wings level equilibria. We derive literal approximations to some lateral stability indicators.
- Control: we demonstrate control and control-related issues through a combination of theoretical analysis and experiments on an actual MAV. We also design PDE-based control schemes to control the deformation of a flexible wing. The control design process makes use of several features of MAV geometry and flight regime.

One point that is particularly worth highlighting is the restriction of our analysis to MAVs. This restriction comes about due to the fact that wing articulation proposed in this thesis would be impractical for larger aircraft. The low flight speed and small size of MAVs lead to several interesting consequences. The low flight speeds imply that the local angle of attack distribution on the wing is a nonlinear function of the angular velocity of the aircraft. The nonlinearity manifests itself in, for example, the peculiar relation between the turn rate and the commanded dihedral as described later in the thesis. The low flight speed and the Young's modulus together lead to time scale separation between the twisting and bending dynamics of a flexible wing, which simplifies the control design process significantly in practical situations.

The problems that we have considered in the thesis have several novel elements. Before stating the contributions of the thesis, we will review the state of the art.

1.1 Literature Review

Fixed and flapping wing MAVs have been extensively studied in the literature. The reader is referred to an excellent compendium of papers [53] which showcases some of the work done in this area until circa 2000. The idea of using cant-angle winglets for control was investigated experimentally by Bourdin, Gatto and Friswell [9, 26] for larger aircraft operating at high Reynolds numbers. However, their analysis was restricted to calculating the aerodynamic moments arising from the use of cant-angle winglets. Wickenheiser and Garcia [107, 108] studied the dynamics of morphing aircraft and demonstrated perching using, among other forms of articulation, variable wing incidence. Reich *et al.* [78] experimentally studied the aerodynamic performance of a wing of variable incidence for perching. Crowther [17] showed that a perched landing can be achieved using a simple pitch-up maneuver, and a similar conclusion was obtained after optimization by Cory and Tedrake [16].

Stenfelt and Ringertz [95, 96] studied the stability and control of tailless aircraft equipped with a split flap mechanism. Shtessel, Buffington and Banda [90] designed a sliding mode-based controller for tailless fighter aircraft, while Patel and co-authors [68] designed a robust adaptive controller for tailless aircraft in the presence of actuator failures. Recently, Obradovic and Subbarao [55] investigated the power requirement for morphing, and used it as a basis to compare wing morphing and the traditional aileron-based control in different flight regimes. The lateral stability and control of birds, and in particular, the role of wing dihedral, have been studied extensively by Sachs and co-authors [83, 81, 82]. Sachs has demonstrated that for air vehicles whose size and speed (and hence, the Reynolds number) are similar to those of birds, wings are sufficient to provide lateral stability thereby reducing, if not eliminating altogether, the need for a vertical tail. Tran and Lind [101] numerically computed the stability of an aircraft equipped with variable symmetric dihedral and incidence. Their wing model consisted of an assemblage of rigid segments.

A variety of aircraft models incorporating wing and fuselage flexibility have been proposed in the literature, although most of these models do not consider wing articulation. Waszak and

Schmidt [106] derived a complete nonlinear model of an aircraft with flexible wings. Their aerodynamic model, however, assumed a steady flow, and their frame of reference consisted of the so-called *mean axes* which are hard to locate in a practical situation. Tuzcu and Meirovitch [51] extended their model in several ways: they used a more intuitive reference frame (the conventional body axes) and a more accurate Theodorsen’s unsteady aerodynamics theory for computing the forces and moments [99]. Recently, Nguyen and Tuzcu [54] presented a dynamic model for a fully flexible aircraft. These papers worked with a small-strain, small-displacement beam theory. In contrast, Patil and co-authors [69, 73] derived a geometrically exact (large displacement) small-strain nonlinear beam model, and used it to study the dynamics and stability of flying wings. Shearer and Cesnik [89] and Su and Cesnik [98] used nonlinear flight dynamic and structural models to investigate the effects of structural nonlinearities on the dynamic stability of aircraft characterized by large aspect ratio wings and blended wing-body configurations, respectively. Baghdadi and co-authors [3] used bifurcation analysis to study the performance and stability of a flexible aircraft model based on Ref. [106] and concluded that flexibility must be accounted for carefully during the control design process. They also demonstrated that a control law designed assuming a rigid configuration could trigger instabilities in an otherwise identical aircraft with flexible wings. Rodden [79] derived analytical expressions, backed by experimental approximations, for increments in the rolling moment derivatives arising from aeroelastic effects.

It has been demonstrated in the literature that aeroelastic instabilities such as wing divergence and flutter can be mitigated using flap-based effectors [5, 76] or passive energy sinks (for flutter) [33]. There is a substantial amount of literature on boundary control theory of PDEs (see Refs. [80, 41, 40, 13, 14, 46] for material pertinent to this thesis and the references cited therein). There are two sets of methods for boundary control of PDEs. The first set consists of methods that seek to convert the PDEs into ordinary differential equations using approximation methods such as those of Galerkin or Rayleigh-Ritz [14, 31], or using operator theory [18, 10]. The second set consists of methods that keep the PDEs intact, and use a “model-following” approach as described in a recent book by Krstic and Smyshlyaev [40].

If a PDE is approximated by Galerkin’s method, or converted into an ODE form using operator theory, the problem of achieving an integral objective reduces to a standard output control problem.

Whereas solutions to output control problems in an ODE setting are abundantly known, an ODE-based approximation to PDEs usually leads to systems having large orders. The ODE-based control design process usually becomes tedious, the control laws become non-intuitive, and the tracking errors could be large for a class of inputs when a poor choice is made for the basis functions which capture the time-varying boundary conditions. Ref. [13] also points out that a finite-state approximation may wrongly render fundamental system theoretic properties like controllability and observability to be functions of the approximation. Stability analysis based on finite state approximation is vulnerable to spillover instabilities which arise due to inadequate accounting of the residual modes [4, 50].

On the other hand, keeping PDEs intact makes the control law design more intuitive. It has been used in the past for maneuvering robotic arms [72, 40], controlling the Navier-Stokes model [104] and suppressing vibrations in a flexible beam [30]. A gain-scheduling based approach for nonlinear PDEs has been presented in Ref. [92], while Krstic and Smyshlyaev [41] derived an adaptive controller for parabolic PDEs.

1.2 Main Contributions

1.2.1 Performance and Stability

As we stated earlier, this thesis is dedicated to MAVs whose speed and size present several distinct characteristics from the point of view of control and stability. The small size of MAV wings makes wing articulation practically feasible. Unlike conventional fixed wing aircraft, an articulated wing aircraft changes its configuration routinely and, therefore, stability is closely tied to the nature of the maneuver being executed. We use bifurcation analysis [28, 47, 67] to explore the dynamics of tailless aircraft equipped with articulated wings. Bifurcation analysis not only measures the stability characteristics of the aircraft, but also helps predict the performance limitations that arise because of the use of asymmetric dihedral. We study a rigid aircraft model to gain a foothold, and then perform a similar analysis on an aircraft with flexible wings for comparison.

The thesis includes detailed theoretical and linear computational analyses of the lateral dynamics. Longitudinal dynamics are not affected by the absence of a vertical stabilizer. Analytical

expressions for lateral-directional aerodynamic force and moment derivatives offer valuable insight into the maneuver-dependence of stability and help identify the source of lateral-directional instability, which is subsequently verified computationally. The analytical expressions also help identify potentially dangerous situations where the control effectiveness of the dihedral may switch sign in the midst of certain maneuvers.

It is known that the wing dihedral angle can be varied to perform slow, steep descents [83, 100]. We compute the gliding flight equilibria numerically along with their stability to identify bounds on longitudinal performance. A knowledge of the longitudinal trims can help formulate landing and perching strategies in spatially-constrained environments without resorting to maneuvers like spin [77] and aid the design of control laws for perching [11].

Next, we compare select performance metrics and stability of the rigid MAV with those of a similar MAV equipped with flexible wings. The purpose of this analysis is two-fold. First, it helps to identify the benefits and limitations of using wing flexibility. Second, and less obviously, it helps to identify the extent to which a rigid MAV model can accurately capture the dynamics of a flexible wing MAV. The flight dynamics will be rendered unstable if the wing is structurally unstable. On the other hand, if the structural stability of the wing can be guaranteed, then the performance and stability of the motion can be computed reliably by considering “macroscopic” parameters like the resultant forces which depend on the shape, rather than stability, of the wing. Therefore, an analysis like the one in this thesis would depend largely on the wing geometry (which is usually well known *a priori*) rather than a precise knowledge of the elastic parameters.

The specific questions answered for a flexible-winged MAV include:

1. For the wing of a typical bird-sized MAV, what value of Young’s modulus (E) should the wing have in order for the MAV to offer a significant performance improvement over a rigid wing MAV? Equivalently, until what point is the open loop analysis of a rigid aircraft relevant to a flexible-winged aircraft? The notion of effective dihedral is introduced in a bid to answer these questions.
2. A stiff wing may be required for certain maneuvers. Axial tension in the wing is an intuitive stiffener. How effective and useful is it? We answer this question in the negative - it is effective, but of limited utility.

3. How is the stability of the motion altered in the presence of flexible wings? The wings are assumed to be quasi-statically deformed and, therefore, the structural dynamics of the wings have no bearing on the conclusion. In other words, the wing is assumed to be structurally stable and its dynamics sufficiently faster than the aircraft.
4. Is there a measurable improvement in the steady state turning performance? Steady state turn rate is the only agility metric which is based entirely on a steady maneuver [61]. It is also an important benchmark to evaluate the efficacy of a yaw control mechanism.

1.2.2 Control

The ideas discussed above were subjected to experimental validation involving open loop as well as closed loop flight tests. The purpose of the experiments is to demonstrate (a) the effectiveness of symmetric dihedral for flight path angle control, (b) yaw control using asymmetric dihedral, and (c) some elements of a perching maneuver [24].

One of the key contributions of this thesis is a boundary control problem for wing twist which could be extended to a wider class of hyperbolic partial differential equations (PDEs). We also consider motion planning for the bending dynamics of an Euler-Bernoulli beam using a novel estimator-based scheme. The problem of controlling a flexible wing presents unique problems as well as helpful features. A flexible wing represents a coupled twist-bending problem in the simplest case, and a coupled twist-bending-rigid-motion problem in the most general case. Either way, problems with coupled PDEs are difficult to solve because the only unified approach to assembling a system of diverse PDEs requires that they be converted into an equivalent or approximate ODE system. This is a cumbersome route.

We show that the twisting dynamics of the MAV wing are faster than the bending dynamics, and the time scale separation depends on the aspect ratio of the wing. We design independent tracking controllers for twist and bending, which can be applied effectively to control the coupled twist-bending dynamics. We also identify the extent of flexibility required to trigger a structural instability in an MAV at routine flight speeds.

We show that wing twist can be stabilized rapidly using a root-based actuator driven by a PDE backstepping controller. The procedure is called backstepping because it involves a Volterra oper-

ator with a lower triangular structure similar to backstepping transforms for ordinary differential equations [39, 40]. It is a continuum analogue of the backstepping transformations in ODEs and allows the controller acting at the boundary to compensate for the undesired (unmatched) dynamics. We also design a tracking control (which is considerably harder when the actuator is located only at the boundary) based on motion-planning which can be added on top of the backstepping controller.

For a class of input-output combinations, we show that the twist dynamics have a finite relative degree which permits a more traditional approach to control design. We show that the tracking controller renders the cantilever wing into the form of a clamped-clamped beam, which improves the stability margin of the twist dynamics by a factor of sixteen. An adaptive controller for a limited class of parametric uncertainties is also derived for tip-based actuators in general, and root-based actuators when the output is the rolling moment.

There are several controller designs in the literature for stabilizing and controlling beam bending (see, for example, [30, 92, 103, 25, 38]). We design a perturbation observer-based controller to facilitate a motion planning-based tracking controller for bending. The output of interest is the displacement of the wing tip. As the name suggests, the perturbation observer designed here uses adaptation to estimate the external forces acting on the system. The observer is split into a “particular” and a “homogeneous” component (the notions are made more precise later). Since the homogeneous component is stable and not driven directly by external feedback, it is simpler to design a control law for it. The same control signal is sent to the actual system, whose states then converge exponentially rapidly to a bounded envelope around the observer states.

1.3 Tools for Modelling, Analysis and Control

In this section, we briefly mention the tools employed in this thesis for modelling and analyzing the flight dynamics, and for control design. A more detailed exposition will be provided in the relevant chapters.

A nonlinear six degree-of-freedom model incorporating dynamic center of gravity (CG) variation and wing flexibility is derived. It can be used for flapping wing aircraft as well, and it is substantially more complete than flapping models in the literature [15, 2]. The wings are assumed to be linearly

elastic and an Euler-Bernoulli beam model is used for modelling wing deformation. The linear model can be replaced readily with a nonlinear deformation model [69] within the framework established here.

Aerodynamic forces on the aircraft wings and the horizontal tail are modelled using strip theory, and in this sense it may be viewed as extension of models used in the flapping wing literature [15, 19, 44]. For a general aeroelastic analysis, we recommend the aerodynamic model proposed by Goman and Khrabrov [27]. For numerical trim computation, we use the aerodynamic data from Uhlig *et al.* [102]

A combination of linear stability theory and bifurcation analysis [67] is used to study the performance and stability of a six degree-of-freedom aircraft model. Co-ordinated turns are studied using a modified version of the constrained bifurcation analysis [60, 67]. Performance metrics of interest are (a) trim angle of attack, velocity, and flight path angle for longitudinal flight assessment, and (b) sideslip angle and turn rate for the lateral-directional motion.

We use PI and PID controllers for experiments. We demonstrate how they can be tuned using a dynamic inversion-based approach [32]. For controlling wing deformation, we use a combination of PDE backstepping [40], adaptive control, and PDE motion planning.

1.4 Organization

The organization of the thesis is given in Fig. 1.2. It shows the flow of the material in the thesis. The complete 6-dof equations of motion for an MAV with flexible articulated wings are derived in Chapter 2. In chapter 3, we analyse the flight dynamics of a rigid aircraft equipped with articulated wings. Chapter 4 is dedicated to the trim and stability analysis of a flexible-winged aircraft. We describe our experiments in Chapter 5. Boundary control of flexible wings has been described in Chapter 6, and Chapter 7 concludes the thesis with a summary of the accomplishments as well as some open problems.

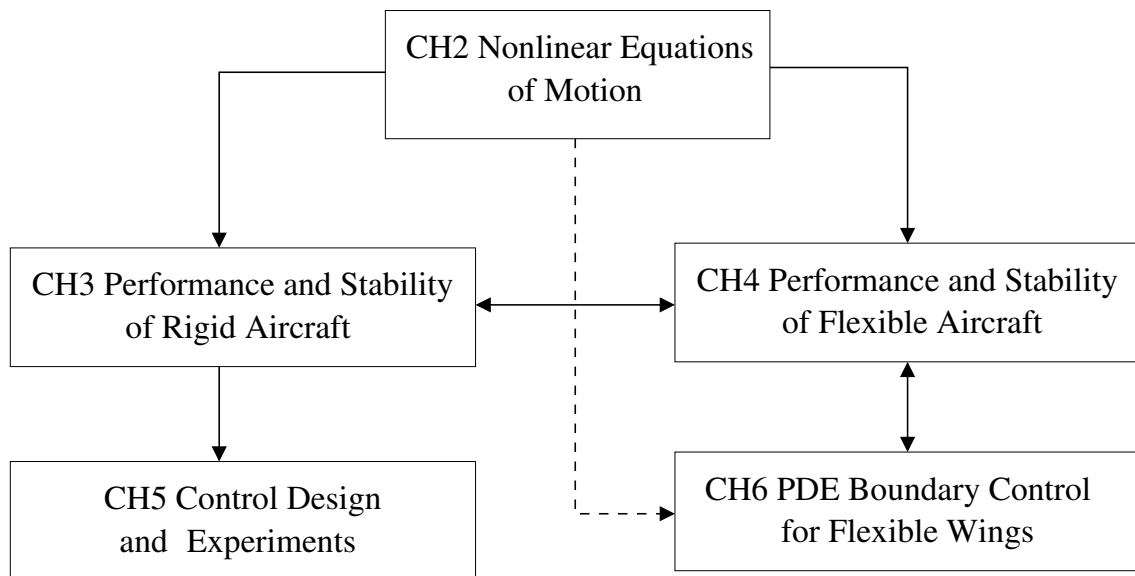


Figure 1.2: Chart showing the organization of the thesis, with arrows denoting the flow of material and interconnections between the chapters.

Chapter 2

Equations of Motion for an Articulated Wing Aircraft

The dynamic model derived in this chapter is general enough that it can be applied to a wider class of problems such as flapping and a complete aeroelastic analysis of aircraft. This chapter consists of two sections. The equations of motion for a flexible aircraft are derived in the first section, and specialized to a rigid aircraft in the second section.

2.1 Notation

Capital letters are reserved for forces, matrices, and for denoting coordinate frames. Small letters are used for scalars when not in bold, and for vectors when used with bold font. Given a vector $\mathbf{x} \in \mathbb{R}^3$, $S(\mathbf{x})$ denotes the cross product operator, i.e.; for any two vectors $\mathbf{x}, \mathbf{y} \in \mathbb{R}^3$, $S(\mathbf{x})\mathbf{y} \triangleq \mathbf{x} \times \mathbf{y}$. Similarly, $S^2(\mathbf{x})\mathbf{y} = S(\mathbf{x})(S(\mathbf{x})\mathbf{y}) = \mathbf{x} \times (\mathbf{x} \times \mathbf{y})$. Given a variable $p(t, y)$, its time derivative is denoted by $\dot{p}(t, y) \triangleq \frac{\partial p(t, y)}{\partial t}$. Its spatial derivative is denoted by $p'(t, y) \triangleq \frac{\partial p(t, y)}{\partial y}$. Note that when $p(t, y) \equiv p(t)$, $\dot{p}(t) = \frac{dp(t)}{dt}$.

2.2 Coordinate Frames of Reference

Given frames F and G , the matrix \mathbf{T}_{FG} is a rotation matrix which transforms the components of a vector from the G frame to F . The body frame, denoted by B , is attached to the body with the $x - z$ plane coincident with the aircraft plane of symmetry when the wings are undeflected. The x axis points towards the aircraft nose. The z axis points downwards, and the y is defined to create a right handed coordinate system. The coordinate frames have been illustrated in Fig 2.1, together with the dimensions of the aircraft considered for numerical analysis.

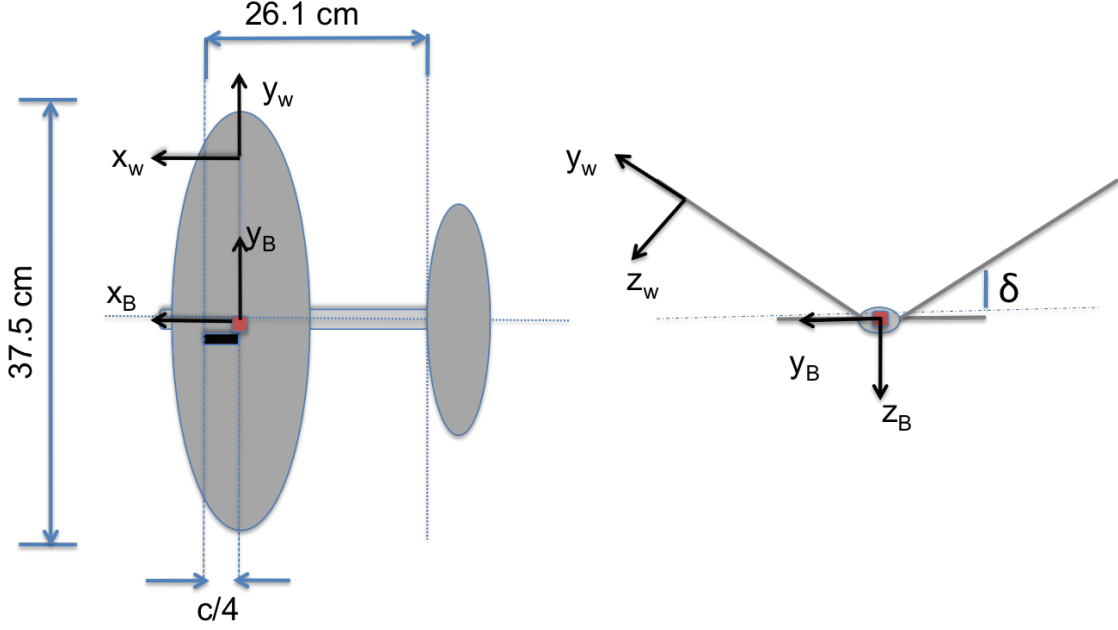


Figure 2.1: A schematic of the aircraft showing the dimensions and the coordinate systems used to model the aircraft.

Consider the frame R based at the right wing root. Its origin coincides with that of the B frame, which is akin to neglecting the fuselage width. This assumption does not alter the rotation matrices in any way. The frame R is related to the B frame via three rotations at the wing root: a sweep rotation β_R about the z -axis, followed by a dihedral rotation δ_R about the $-x$ -axis, and a rotation θ_R about the y axis. The y axis points along the wing elastic axis. Thus,

$$\mathbf{T}_{BR} = \begin{bmatrix} \cos \beta_R & -\sin \beta_R & 0 \\ \sin \beta_R & \cos \beta_R & 0 \\ 0 & 0 & 1 \end{bmatrix} \begin{bmatrix} 1 & 0 & 0 \\ 0 & \cos \delta_R & \sin \delta_R \\ 0 & -\sin \delta_R & \cos \delta_R \end{bmatrix} \begin{bmatrix} \cos \theta_R & 0 & \sin \theta_R \\ 0 & 1 & 0 \\ -\sin \theta_R & 0 & \cos \theta_R \end{bmatrix} \quad (2.1)$$

A similar matrix can be defined for the left wing. The matrix \mathbf{T}_{BR} is introduced here in the most general form, i.e., no rotation is ignored, which makes it applicable to flapping flight dynamics. From hereon, we assume that $\beta_R = \beta_L = 0$.

The frame $S \equiv S(y)$ is the frame located at a spanwise wing station with origin at the elastic center, and y axis pointing along the elastic axis. The frame S is related to R via two rotations: a rotation about the x axis through the strain $\xi'(y)$, and a rotation (twist) $\theta_s(y)$ about the y axis.

Thus,

$$\mathbf{T}_{RS} = \begin{bmatrix} \cos \theta_s(y) & 0 & \sin \theta_s(y) \\ \sin(\xi'(y)) \sin \theta_s(y) & \cos(\xi'(y)) & -\sin(\xi'(y)) \cos \theta_s(y) \\ -\cos(\xi'(y)) \sin \theta_s(y) & \sin(\xi'(y)) & \cos(\xi'(y)) \cos \theta_s(y) \end{bmatrix} \quad (2.2)$$

In the interests of analytical tractability, for the purposes of computing the velocities and acceleration terms, it will be assumed that $\mathbf{T}_{BS} = \mathbf{T}_{BR}$, i.e., the deformations are small enough that they do not alter the coordinate transformations. However, in Sec. 2.6, this assumption is relaxed for computing the aerodynamic forces and moments. This is the primary source of the difference in the forces and moments produced by rigid and flexible wings.

2.3 Calculating the Velocity at a Spanwise Station

The angular velocity of the right wing, $\boldsymbol{\omega}_R$ with components in the body frame, is given by

$$\boldsymbol{\omega}_R = \begin{bmatrix} -\cos \beta_R & -\cos \delta_R \sin \beta_R & 0 \\ -\sin \beta_R & \cos \delta_R \cos \beta_R & 0 \\ 0 & \sin \delta_R & 1 \end{bmatrix} \begin{bmatrix} \dot{\beta}_R \\ \dot{\theta}_R \\ \dot{\beta}_R \end{bmatrix} \quad (2.3)$$

It is calculated using a 3-1-2 Euler angle sequence which is also used to calculate \mathbf{T}_{BR} . The same sequence can be used to model a flapping wing, in which case, the amplitude and phase of the motion corresponding to each degree of freedom needs to be prescribed. In contrast, most flapping wing models prefer to identify a stroke plane in which the flapping motion is constrained, and which also contains the twist axis (see Refs. [15, 7, 91] and the references cited therein).

Let $\mathbf{y} = [0 \ y \ \xi]^T$ denote the coordinates of a spanwise station on the wing along the twisting axis. Then the local wind velocity, with components in the local station frame, is given by

$$\mathbf{V} = \mathbf{T}_{SB}\mathbf{u}_B + \mathbf{u}_f + \mathbf{T}_{SB}S(\boldsymbol{\omega}_B + \boldsymbol{\omega}_R)\mathbf{T}_{BR}\mathbf{y} \quad (2.4)$$

A similar expression can be determined for the angular velocity of the left wing at the root, $\boldsymbol{\omega}_L$, and the local velocity at a spanwise station on the left wing.

The aerodynamic center is assumed to be located at the quarter chord point. The velocity at

the 3/4-chord point of a spanwise station is used for calculating the angle of attack, and it is given by

$$\mathbf{V}_{3/4}(y) = \mathbf{V} + S(\boldsymbol{\omega}_s)\mathbf{x}_{3/4} \quad (2.5)$$

where $\mathbf{x}_{3/4} = [(x_a - 0.5)c \ 0 \ 0]^T$. Let $[u_{3/4}(y), \ v_{3/4}(y), \ w_{3/4}(y)]$ denote the components of $\mathbf{V}_{3/4}$ in the local station frame, and $V_{3/4}$ its magnitude. Then, the local angle of attack and sideslip can be calculated using

$$\tan \alpha(y) = \frac{w_{3/4}}{u_{3/4}}, \quad \sin \beta(y) = \frac{v_{3/4}}{V_{3/4}} \quad (2.6)$$

2.4 Aircraft Equations of Motion

Let m_R and m_L denote the masses of the right wing and left wing, respectively. Let \tilde{m}_R and \tilde{m}_L denote the masses per unit length of the right wing and left wing, respectively. Let \mathbf{r}_{CG} denote the position of the center of gravity of the aircraft. Let $\mathbf{r}_s = [x_e c, 0, 0]^T$ denote location of the center of gravity with respect to the wing twist, and let $\mathbf{y} = [x_e c \cos \theta_s(y), \ y, \ \xi - x_e c \sin \theta_s(y)]^T$ denote the position of the center of gravity of a wing station in the wing root frame. Let $\boldsymbol{\omega}_s \triangleq [0 \ \dot{\theta}_s \ 0]^T$ denote the angular velocity of a given wing station due to twisting. The total linear momentum of the aircraft is the sum of the momenta of the fuselage and the two wings. The momentum and force vectors are written with respect to the body axes, fixed at the wing root. The linear momentum of the aircraft is given by

$$\begin{aligned} \mathbf{p} = & m(\mathbf{u}_B + S(\boldsymbol{\omega}_B)\mathbf{r}_{CG}) + \tilde{m}_R \int_0^{b/2} (S(\boldsymbol{\omega}_R)\mathbf{T}_{BR}\mathbf{y}) dy + \tilde{m}_L \int_{-b/2}^0 (S(\boldsymbol{\omega}_L)\mathbf{T}_{BR}\mathbf{y}) dy \\ & + \tilde{m}_R \int_0^{b/2} (\mathbf{T}_{BR}\mathbf{u}_f(y) + \mathbf{T}_{BR}S(\boldsymbol{\omega}_s)\mathbf{r}_s) dy + \tilde{m}_L \int_{-b/2}^0 (\mathbf{T}_{BS}\mathbf{u}_f(y) + \mathbf{T}_{BR}S(\boldsymbol{\omega}_s)\mathbf{r}_s) dy \end{aligned} \quad (2.7)$$

where m is the total mass of the aircraft, including the masses of the fuselage and the horizontal tail. In Eq. (2.7), it is assumed that the wing has a constant mass per unit span. It must be noted that this assumption is, strictly speaking, not essential for the derivation of the aircraft equations of motion since no spatial derivatives are involved. In the present case, it only serves the purpose

of succinctness. Differentiating the right hand side with time, and setting $\left[\frac{d\mathbf{p}}{dt} \right]_I = \mathbf{F}_b$, we get

$$\begin{aligned}
& m(\dot{\mathbf{u}}_B + S(\boldsymbol{\omega}_B)\mathbf{u}_B + S(\dot{\boldsymbol{\omega}}_B)\mathbf{r}_{CG} + S^2(\boldsymbol{\omega}_B)\mathbf{r}_{CG} + S(\boldsymbol{\omega}_B)\dot{\mathbf{r}}_{CG}) + \\
& \tilde{m}_R \int_0^{b/2} ((S(\boldsymbol{\omega}_R + \boldsymbol{\omega}_B)S(\boldsymbol{\omega}_R) + S(\dot{\boldsymbol{\omega}}_R))\mathbf{T}_{BR}\mathbf{y} + S(\boldsymbol{\omega}_R)\mathbf{T}_{BR}\mathbf{u}_f) dy \\
& + \tilde{m}_L \int_{-b/2}^0 ((S(\boldsymbol{\omega}_L + \boldsymbol{\omega}_B)S(\boldsymbol{\omega}_L) + S(\dot{\boldsymbol{\omega}}_L))\mathbf{T}_{BR}\mathbf{y} + S(\boldsymbol{\omega}_L)\mathbf{T}_{BR}\mathbf{u}_f) dy \\
& + \tilde{m}_R \int_0^{b/2} (\mathbf{T}_{BR}\dot{\mathbf{u}}_f(y) + S(\boldsymbol{\omega}_B + \boldsymbol{\omega}_R + \mathbf{T}_{BR}\boldsymbol{\omega}_s)\mathbf{T}_{BR}(\mathbf{u}_f + S(\boldsymbol{\omega}_s)\mathbf{r}_s) + \mathbf{T}_{BR}S(\boldsymbol{\omega}_s)\mathbf{r}_s) dy \\
& + \tilde{m}_L \int_{-b/2}^0 (\mathbf{T}_{BR}\dot{\mathbf{u}}_f(y) + S(\boldsymbol{\omega}_B + \boldsymbol{\omega}_L + \mathbf{T}_{BR}\boldsymbol{\omega}_s)\mathbf{T}_{BR}(\mathbf{u}_f + S(\boldsymbol{\omega}_s)\mathbf{r}_s) + \mathbf{T}_{BR}(S(\boldsymbol{\omega}_s)\mathbf{r}_s) dy = [X_B \ Y_B \ Z_B]^T
\end{aligned} \tag{2.8}$$

where $[X_B, Y_B, Z_B]$ is the net force acting on the aircraft (aerodynamic plus gravitational), with components in the body frame. An expression for the net force is given Sec. 2.6. The position vector of the center of gravity (CG) is given by

$$\dot{\mathbf{r}}_{CG} = \frac{1}{m} \left(\tilde{m}_R \int_0^{b/2} (\mathbf{u}_f + S(\boldsymbol{\omega}_R)\mathbf{T}_{BR}\mathbf{y}) dy + \tilde{m}_L \int_{-b/2}^0 (\mathbf{u}_f + S(\boldsymbol{\omega}_L)\mathbf{T}_{BR}\mathbf{y}) dy \right) \tag{2.9}$$

For highly flexible or rapidly flapping wings, the dynamics of the CG serve to couple the translational and rotational dynamics tightly. The CG location can be changed using an actuated mass, such as the bob weight in Doman, Oppenheimer, and Sighorsson [22], for controlling the aircraft attitude.

The total angular momentum of the aircraft is given by

$$\begin{aligned}
\mathbf{h} &= \mathbf{J}\boldsymbol{\omega}_B + mS(\mathbf{r}_{CG})\mathbf{u}_B \\
&- \int_0^{b/2} (S(\mathbf{T}_{BR}\mathbf{y} + \mathbf{T}_{BR}\mathbf{x}))\mathbf{u}_f + S(\mathbf{T}_{BR}\mathbf{y} + \mathbf{T}_{BR}\mathbf{x})(S(\mathbf{T}_{BR}\mathbf{y} + \mathbf{T}_{BR}\mathbf{x})(\boldsymbol{\omega}_B + \boldsymbol{\omega}_R) + S(\mathbf{T}_{BR}\mathbf{x})\boldsymbol{\omega}_s)) dm \\
&- \int_{-b/2}^0 (S(\mathbf{T}_{BR}\mathbf{y} + \mathbf{T}_{BR}\mathbf{x}))\mathbf{u}_f + S(\mathbf{T}_{BR}\mathbf{y} + \mathbf{T}_{BR}\mathbf{x})(S(\mathbf{T}_{BR}\mathbf{y} + \mathbf{T}_{BR}\mathbf{x})(\boldsymbol{\omega}_B + \boldsymbol{\omega}_L) + S(\mathbf{T}_{BR}\mathbf{x})\boldsymbol{\omega}_s)) dm
\end{aligned}$$

where \mathbf{x} represents the coordinates of a point on the cross section of the wing in the local station frame. The moment of inertia of the right wing is given by

$$\mathbf{J}_R = - \int_0^{b/2} S^2(\mathbf{T}_{BR}\mathbf{y} + \mathbf{T}_{BR}\mathbf{x}) dm \tag{2.10}$$

and \mathbf{J}_L is defined similarly. It follows that

$$\begin{aligned} \mathbf{h} = & \mathbf{J}\boldsymbol{\omega}_B + \mathbf{J}_R\boldsymbol{\omega}_R + \mathbf{J}_L\boldsymbol{\omega}_L + mS(\mathbf{r}_{CG})\mathbf{u}_B - \int_0^{b/2} S(\mathbf{T}_{BR}\mathbf{y} + \mathbf{T}_{BR}\mathbf{x})\mathbf{T}_{BR}(\mathbf{u}_f + S(\mathbf{x})\boldsymbol{\omega}_s)dm \\ & - \int_{-b/2}^0 S(\mathbf{T}_{BR}\mathbf{y} + \mathbf{T}_{BR}\mathbf{x})\mathbf{T}_{BR}(\mathbf{u}_f + S(\mathbf{x})\boldsymbol{\omega}_s)dm \end{aligned} \quad (2.11)$$

where $\rho_{w,R}$ and $\rho_{w,L}$ denote the densities of the right and left wing, respectively, and \mathbf{J} is the total moment of inertia of the aircraft. The reader would be correct in judging that differentiating this expression would yield a cumbersome set of equations for the rotational dynamics. In order to keep the expression tractable, it has been assumed that the moment of inertia of the wing is constant in magnitude, i.e., the effect of wing bending and twist on the net moment of inertia of the aircraft is ignored. Subject to this assumption, the following dynamic equation for rotational motion is obtained:

$$\begin{aligned} & \mathbf{J}\dot{\boldsymbol{\omega}}_B + S(\boldsymbol{\omega}_B)\mathbf{J}\boldsymbol{\omega}_B + mS(\boldsymbol{\omega}_B)S(\mathbf{r}_{CG})\mathbf{u}_B + mS(\mathbf{r}_{CG})\dot{\mathbf{u}}_B + S(\dot{\mathbf{r}}_{CG})\mathbf{u}_B + \mathbf{J}_R\dot{\boldsymbol{\omega}}_R + \mathbf{J}_L\dot{\boldsymbol{\omega}}_L \\ & + S(\boldsymbol{\omega}_B)(\mathbf{J}_R\boldsymbol{\omega}_R + \mathbf{J}_L\boldsymbol{\omega}_L) + (S(\boldsymbol{\omega}_R)\mathbf{J}_R - \mathbf{J}_RS(\boldsymbol{\omega}_R))(\boldsymbol{\omega}_B + \boldsymbol{\omega}_R) + (S(\boldsymbol{\omega}_L)\mathbf{J}_L - \mathbf{J}_LS(\boldsymbol{\omega}_L))(\boldsymbol{\omega}_B + \boldsymbol{\omega}_L) \\ & - \tilde{m}_R \int_0^{b/2} \left(S(\boldsymbol{\omega}_B + \boldsymbol{\omega}_R)S(\mathbf{T}_{BR}\mathbf{y})\mathbf{T}_{BR}(\mathbf{u}_f + S(\mathbf{r}_s)\boldsymbol{\omega}_s) + S(\mathbf{T}_{BR}\mathbf{y})\mathbf{T}_{BR}(\dot{\mathbf{u}}_f + S(\mathbf{r}_s)\dot{\boldsymbol{\omega}}_s) \right) dy \\ & - \tilde{m}_L \int_{-b/2}^0 \left(S(\boldsymbol{\omega}_B + \boldsymbol{\omega}_L)S(\mathbf{T}_{BR}\mathbf{y})\mathbf{T}_{BR}(\mathbf{u}_f + S(\mathbf{r}_s)\boldsymbol{\omega}_s) + S(\mathbf{T}_{BR}\mathbf{y})\mathbf{T}_{BR}(\dot{\mathbf{u}}_f + S(\mathbf{r}_s)\dot{\boldsymbol{\omega}}_s) \right) dy \\ & + \int_0^{b/2} (\rho_{w,R}(\mathbf{T}_{BR}\mathbf{J}_s\dot{\boldsymbol{\omega}}_s + S(\boldsymbol{\omega}_B + \boldsymbol{\omega}_R)\mathbf{T}_{BR}\mathbf{J}_s\boldsymbol{\omega}_s) - \tilde{m}_RS(\mathbf{T}_{BR}\mathbf{u}_f)\mathbf{T}_{BR}S(\mathbf{r}_s)\boldsymbol{\omega}_s) dy \\ & + \int_{-b/2}^0 (\rho_{w,L}(\mathbf{T}_{BR}\mathbf{J}_s\dot{\boldsymbol{\omega}}_s + S(\boldsymbol{\omega}_B + \boldsymbol{\omega}_L)\mathbf{T}_{BR}\mathbf{J}_s\boldsymbol{\omega}_s) - \tilde{m}_LS(\mathbf{T}_{BR}\mathbf{u}_f)\mathbf{T}_{BR}S(\mathbf{r}_s)\boldsymbol{\omega}_s) dy = [L \ M \ N]^T \end{aligned} \quad (2.12)$$

where $\mathbf{J}_s(y) = - \int \int_S S^2(\mathbf{x})dA$ denotes the second moment of area matrix of a cross section of the wing. An expression for the net moment ($[L \ M \ N]$) is given Sec. 2.6. Note that if the terms arising from flexibility are ignored along with the wing root angular velocity, then, with the additional assumption that $\mathbf{r}_{CG} = 0$, Euler's equations are recovered as one would expect. The equations of motion derived in this equation incorporate wing rotation (see Eq. (2.3) which expresses $\boldsymbol{\omega}_R$ in terms of the flapping rates) and therefore, this model can be used for a study of flexible flapping wings as well.

2.4.1 Structural Dynamics

The bending and twisting elastic equations of motion for the right wing are given by

$$\begin{bmatrix} \tilde{m}_R & -\tilde{m}_R x_e c \\ -\tilde{m}_R x_e c & I_p \end{bmatrix} \begin{bmatrix} [\dot{\mathbf{V}}]_3 \\ [\dot{\boldsymbol{\Omega}}]_2 \end{bmatrix} + \begin{bmatrix} \eta(EI_b \dot{\xi}'')'' + (EI_b \xi'')'' - T \xi'' \\ -\eta(G \tilde{J} \dot{\theta}_s')' - (G \tilde{J} \theta_s')' \end{bmatrix} = \begin{bmatrix} \mathbf{F}_{s,3} \\ \mathbf{M}_{s,2} \end{bmatrix} \quad (2.13)$$

where

$$\dot{\boldsymbol{\Omega}} = \dot{\boldsymbol{\omega}}_s + \mathbf{T}_{SB}(\dot{\boldsymbol{\omega}}_B + \dot{\boldsymbol{\omega}}_R), \quad (2.14)$$

and

$$\begin{aligned} \dot{\mathbf{V}} &= \mathbf{T}_{SB}\dot{\mathbf{u}}_B + \dot{\mathbf{u}}_f + S(\boldsymbol{\omega}_B + \boldsymbol{\omega}_R)(\mathbf{T}_{SB}\mathbf{u}_B + \mathbf{u}_f) + \mathbf{T}_{SB}S(\boldsymbol{\omega}_B + \boldsymbol{\omega}_R)\mathbf{T}_{BR}\mathbf{u}_f \\ &\quad + \mathbf{T}_{SB}(S(\dot{\boldsymbol{\omega}}_B + \dot{\boldsymbol{\omega}}_R) + S^2(\boldsymbol{\omega}_B + \boldsymbol{\omega}_R))\mathbf{T}_{BR}\mathbf{y} \\ \xi &= \xi_f - y\delta_R \\ \mathbf{u}_f &= [0 \ 0 \ \dot{\xi}_f]^T, \end{aligned} \quad (2.15)$$

Remark: The displacement ξ should be viewed as comprised of the deformation ξ_f , and a rigid component, $y\delta_R$, i.e., $\xi = \xi_f(y) - y\delta_R$, with $\xi'_f(0) = 0$. This perspective is helpful from the point of view of practical implementation of boundary control schemes. Likewise, one may consider θ_s as the sum of flexible and rigid twist contributions (denoted by θ_R), instead of a pure deformation. Then, the wing may be viewed as being clamped at the root, with $\theta_s(0) = \theta_R + 0$ (zero deformation at the root). This decomposition of ξ and θ_s changes neither the governing equations nor the boundary conditions, because the rigid terms do not affect the stiffness and damping terms, while they are already incorporated into the accelerations and the right hand side.

Note that $I_p = \rho_w \mathbf{J}_s(2, 2)$ and $I_b = \mathbf{J}_s(1, 1)$, where ρ_w denotes the density of the wing. Furthermore, $\mathbf{F}_{s,3} \triangleq \mathbf{F}_{s,3}(\alpha, \dot{\alpha}, V_\infty, \mathbf{u}_f, \theta, \dot{\theta})$ is the total force acting in the local z direction (hence the subscripts ‘s’ and ‘3’), while $\mathbf{M}_{s,2} \triangleq \mathbf{M}_{s,2}(\alpha, \dot{\alpha}, V_\infty, \mathbf{u}_f, \theta, \dot{\theta})$ is the local pitching moment. The arguments of \mathbf{F} and \mathbf{M} listed here are by no means exhaustive; rather, they are the primary contributors. The term $[\dot{\mathbf{V}}]_3$ denotes the z -component of the local acceleration, and $[\dot{\boldsymbol{\omega}}]_2$ is the y -component of the local angular acceleration. Expressions for the net force and moment are given in Sec. 2.6. The Kelvin-Voigt damping coefficient is obtained by scaling EI_b and $G\tilde{J}$ by a factor of

η in the bending and twist equations, respectively.

Remark: The scaling term η will not be equal for both cases, viz., bending and twist, in the most general case. Furthermore, it is common among structural dynamicists to model the damping coefficient as a linear combination of the mass (or moment of inertia) and stiffness.

Remark: The linear model presented here can be readily replaced by a nonlinear model in the proposed coordinates to match the requirements of the problem at hand.

The boundary conditions are given by the following expressions.

- At the wing root: $\xi = 0$, while ξ' and θ_s can be set arbitrarily (within admissible limits) as the dihedral angle and the twist, respectively, at the wing root.
- At the wing tip: $\xi'' = 0$, $(EI_b\xi'')' - T\xi' = 0$ and $\theta'_s = 0$ (i.e., free end boundary conditions).

Remark: If the tension T is spatially varying, i.e., $T \equiv T(y)$, then an additional term, $T'\xi'_f$, needs to be added alongside $T\xi''$ in Eq. (2.13).

Boundary conditions at the wing root, in particular $\theta_s(0)$ and $\xi'(0)$, can be controlled actively via dedicated actuators for stabilizing an unstable wing or for ensuring that the net force on the wing or its components achieve the desired value for specific maneuvers [64].

2.5 Fuselage Kinematics

The fuselage attitude is described by the Euler angles ψ , θ and ϕ . The kinematic equations are given by

$$\begin{aligned}\dot{\phi} &= p + q \tan \theta \sin \phi + r \tan \theta \cos \phi, \\ \dot{\theta} &= q \cos \phi - r \sin \phi, \\ \dot{\psi} &= (q \sin \phi + r \cos \phi) \sec \theta\end{aligned}\tag{2.16}$$

The equations which relate the position of the aircraft to its translational velocity are essentially decoupled from the flight dynamics, and are given by

$$\begin{aligned}\dot{X} &= V_{\text{gn}} \cos \gamma \cos \chi \\ \dot{Y} &= V_{\text{gn}} \cos \gamma \sin \chi \\ \dot{Z} &= -V_{\text{gn}} \sin \gamma\end{aligned}\tag{2.17}$$

where V_{gn} is the ground speed of the aircraft (obtained by subtracting the velocity of the wind from that of the aircraft). The flight path angle (γ) and the wind axis heading angle (χ) in Eq. (2.17) are defined as follows:

$$\begin{aligned}\sin \gamma &= \cos \alpha \cos \beta \sin \theta - \sin \beta \sin \phi \cos \theta - \sin \alpha \cos \beta \cos \phi \cos \theta \\ \sin \chi \cos \gamma &= \cos \alpha \cos \beta \cos \theta \sin \psi + \sin \beta (\sin \phi \sin \theta \sin \psi + \cos \phi \cos \psi) \\ &\quad + \sin \alpha \cos \beta (\cos \phi \sin \theta \sin \psi - \sin \phi \cos \psi)\end{aligned}\tag{2.18}$$

The turn rate is given by $\omega = \dot{\chi}$. If $\dot{\theta} = \dot{\phi} = \dot{\beta} = 0$, it follows that

$$\omega = \dot{\psi} = (q \sin \phi + r \cos \phi) \sec \theta\tag{2.19}$$

2.6 Forces

The net force on the aircraft consists primarily of contributions from aerodynamic and gravitational forces. For numerical analysis, the aerodynamic forces and moments are calculated using strip theory. As a method, strip theory is used for aircraft aeroelastic simulations [110] and routinely for blade element theory in the rotorcraft field [34]. Strip theory approaches have also been applied to wings in a trailing vortex flow and aircraft spin prediction (see references [49, 71, 58, 57] and others cited therein). It seems that only recently has the general strip theory approach been applied in realtime simulation for fixed-wing force and moment calculations [97, 36, 35, 86, 87]. Strip theory methods have also been applied to flapping wing aircraft [19, 44, 15].

The wing is divided into chord-wise strips. The lift, drag, and the quarter chord aerodynamic

moment at each strip can be computed by using a suitable aerodynamic model, and these can be summed over the entire wing to yield the net aerodynamic force and moment. A similar calculation is performed for the horizontal tail and added to the wing contributions. The aerodynamic contributions of the fuselage are ignored with the understanding that they can be added readily to the model.

Since the model developed is intended to be as generic as possible, the model proposed by Goman and Khrabrov [27] is presented in this section as a candidate model for computing the lift and the quarter chord moment while drag is estimated assuming the classic drag polar. In the authors' estimate, Goman and Khrabrov's model offers at least two advantages over the existing models (such as Theodorsen [99] or Peters [70]). First, the model is cast in the form of a single ordinary differential equation (ODE) and two algebraic equations, one each for lift and the quarter chord pitching moment. The state variable for the ODE corresponds, physically, to the chordwise location of flow separation on the airfoil. Therefore, the model is quite easy to implement as part of a numerical routine. Second, the model is inherently nonlinear and applicable to post-stall flight.

The following equation describes the movement of the separation point for unsteady flow conditions

$$\tau_1 \dot{\nu} + \nu = \nu_0(\alpha - \tau_2 \dot{\alpha}) \quad (2.20)$$

where ν denotes the position of the separation point, τ_1 is the relaxation time constant, and τ_2 captures the time delay effects due to the flow, while ν_0 is an expression for the nominal position of the separation point. These three parameters need to be identified experimentally or using CFD for the particular airfoil under consideration. The coefficients of lift and quarter-chord moment are then given by

$$\begin{aligned} C_l^* &= \frac{\pi}{2} \sin(\alpha(1 + \nu + 2\sqrt{\nu})) \\ C_{m_{ac}}^* &= \frac{\pi}{2} \sin(\alpha(1 + \nu + 2\sqrt{\nu})) \left[\frac{5 + 5\nu - 6\sqrt{\nu}}{16} \right] \end{aligned} \quad (2.21)$$

The lift force and the quarter chord moment per unit span are then given by

$$\begin{aligned} L(y) &= 0.5\rho V(y)^2 c C_l^* + \frac{\pi}{4} \rho c^2 \left(\ddot{\xi} + V_\infty \dot{\alpha} - (x_a - 0.25) c \ddot{\alpha} \right) \\ M(y) &= 0.5\rho V(y)^2 c^2 C_{m_{ac}}^* + \frac{\pi}{4} \rho c^2 \left(V_\infty \dot{\xi} + \frac{(x_a - 0.25) c \ddot{\xi}}{2} + V_\infty^2 \alpha - c^2 \left(\frac{1}{32} + (x_a - 0.25)^2 \right) \ddot{\alpha} \right) \end{aligned} \quad (2.22)$$

where α is the local angle of attack, and ρ denotes the density of air. Furthermore, $V = \|\mathbf{V}\|$ is the local wind speed with \mathbf{V} defined in Eq. (2.4), and V_∞ is the freestream speed of the aircraft given by $V_\infty = \|\mathbf{u}_B\|$. The last term of each expression was added to Goman's original model [27] and corresponds to the apparent mass effect [19].

There is, unfortunately, no simple expression for the sectional drag coefficient. The sectional drag coefficient can be written as

$$C_d = \frac{0.664}{\sqrt{Re}} + \frac{1}{\pi e A_R} C_l^2, \quad (2.23)$$

where $C_l = \frac{L(y)}{0.5\rho V(y)^2 c}$, A_R is the aspect ratio of the wing, Re denotes the chordwise Reynolds number, and e is Oswald's efficiency factor. The skin friction term [43] assumes laminar flow over the wing and may need to be replaced with a different approximation (see DeLaurier [19] for instance). The drag model is quasi-steady in nature so that dynamic stall effects are not included. A refined model for calculating drag, incorporating dynamic stall, may be found in DeLaurier [19].

The local aerodynamic force on each wing can be written in the body axis system

$$\begin{bmatrix} X_A(y) \\ Y_A(y) \\ Z_A(y) \end{bmatrix} = \mathbf{T}_{BS} \begin{bmatrix} L(y) \sin \alpha(y) - D(y) \cos \alpha(y) \\ 0 \\ -L(y) \cos \alpha(y) - D(y) \sin \alpha(y) \end{bmatrix} \quad (2.24)$$

Note that \mathbf{T}_{BS} is used instead of \mathbf{T}_{BR} and this is the most important source of the difference between the resultant of the forces and moments on a flexible wing vis-a-vis a rigid wing. The components of the gravitational force are given by

$$X_g = -mg \sin \theta, \quad Y_g = mg \cos \theta \sin \phi, \quad Z_g = mg \cos \theta \cos \phi \quad (2.25)$$

and the corresponding moment is given by $S(\mathbf{r}_{cg})[X_g \ Y_g \ Z_g]^T$.

The net aerodynamic force on two wings is given by

$$\begin{bmatrix} X_B \\ Y_B \\ Z_B \end{bmatrix}_{\text{wing}} = \int_0^{b/2} \begin{bmatrix} X_A(y) \\ Y_A(y) \\ Z_A(y) \end{bmatrix}_{\text{right}} dy + \int_0^{b/2} \begin{bmatrix} X_A(y) \\ Y_A(y) \\ Z_A(y) \end{bmatrix}_{\text{left}} dy \quad (2.26)$$

The net aerodynamic moment due to the two wings is given by

$$\begin{bmatrix} L \\ M \\ N \end{bmatrix}_{\text{wing}} = \int_0^{b/2} S(\mathbf{y}) \begin{bmatrix} X_A(y) \\ Y_A(y) \\ Z_A(y) \end{bmatrix}_{\text{right}} dy + \int_0^{b/2} S(\mathbf{y}) \begin{bmatrix} X_A(y) \\ Y_A(y) \\ Z_A(y) \end{bmatrix}_{\text{left}} dy \quad (2.27)$$

A similar calculation can be performed for the horizontal tail. The net force and moment on the aircraft themselves are the sum of the contributions from the wing, the horizontal tail and gravity:

$$\begin{aligned} \begin{bmatrix} X_B \\ Y_B \\ Z_B \end{bmatrix} &= \begin{bmatrix} X_B \\ Y_B \\ Z_B \end{bmatrix}_{\text{wing}} + \begin{bmatrix} X_B \\ Y_B \\ Z_B \end{bmatrix}_{\text{tail}} + \begin{bmatrix} X_g \\ Y_g \\ Z_g \end{bmatrix} \\ \begin{bmatrix} L \\ M \\ N \end{bmatrix} &= \begin{bmatrix} L \\ M \\ N \end{bmatrix}_{\text{wing}} + \begin{bmatrix} L \\ M \\ N \end{bmatrix}_{\text{tail}} + S(\mathbf{r}_{cg}) \begin{bmatrix} X_g \\ Y_g \\ Z_g \end{bmatrix} \end{aligned} \quad (2.28)$$

This completes the formulation of the equations of motion.

2.7 Trim Equations

The rigid body equations of motion and the structural dynamic equations are coupled because of acceleration terms. Therefore, for the purpose of locating equilibrium flight conditions (or trims), the rigid body equations of motion and the structural dynamic equations can be decoupled. Specifically, the structural dynamic equations themselves split into bending and twisting equations, which give rise to boundary value problems.

Trims are computed for the flexible-winged aircraft using the `fsolve` routine in MATLAB.

The structural mechanic boundary value problem is solved in-the-loop using MATLAB's built-in boundary value problem solver called `bvp4c` [88]. The wings are assumed to be quasi-statically deformed which allows for stability computation of the aircraft motion using the flight dynamic equations.

2.8 Specialization to a Rigid Aircraft

In this section, we specialize the equations of motion derived in the Sec. 2.4 to a rigid aircraft. In the process, we simply ignore the terms that arise due to wing deformation.

The equations of translational motion are derived first. Let \mathbf{r}_{cg} denote the position vector of the centre of gravity (CG) of the aircraft, while $\mathbf{r}_{cg,R}$ and $\mathbf{r}_{cg,L}$ denote the position vectors of the CG of the right and left wings, respectively. Then, the total translational momentum is given by

$$\mathbf{p} = m(\mathbf{u}_B + S(\boldsymbol{\omega}_B)\mathbf{r}_{cg}) + m_w(S(\boldsymbol{\omega}_R)\mathbf{T}_{BR}\mathbf{r}_{cg,R} + S(\boldsymbol{\omega}_L)\mathbf{T}_{BL}\mathbf{r}_{cg,L}) \quad (2.29)$$

Using Newton's second law, we obtain

$$\begin{aligned} \mathbf{F} = & m(\dot{\mathbf{u}}_B + S(\boldsymbol{\omega}_B)\mathbf{u}_B + S(\dot{\boldsymbol{\omega}}_B)\mathbf{r}_{cg} + S(\boldsymbol{\omega}_B)\dot{\mathbf{r}}_{cg} + (S^2(\boldsymbol{\omega}_B)\mathbf{r}_{cg}) \\ & + m_w S(\dot{\boldsymbol{\omega}}_R)\mathbf{T}_{BR}\mathbf{r}_{cg,R} + m_w S^2(\boldsymbol{\omega}_R)\mathbf{T}_{BR}\mathbf{r}_{cg,R} \\ & + m_w S(\dot{\boldsymbol{\omega}}_L)\mathbf{T}_{BL}\mathbf{r}_{cg,L} + m_w S^2(\boldsymbol{\omega}_L)\mathbf{T}_{BL}\mathbf{r}_{cg,L}, \end{aligned} \quad (2.30)$$

and the CG variation is given by

$$\dot{\mathbf{r}}_{cg} = \frac{m_w}{m}(S(\boldsymbol{\omega}_R)\mathbf{T}_{BR}\mathbf{r}_{cg,R} + S(\boldsymbol{\omega}_L)\mathbf{T}_{BL}\mathbf{r}_{cg,L}) \quad (2.31)$$

This CG variation could play an important role in cases where the wing weight is substantial and where the CG position is used as a control variable, as in [22].

The total angular momentum is given by

$$\begin{aligned} \mathbf{h} = & mS(\mathbf{r}_{cg})\mathbf{u}_B + \mathbf{J}\boldsymbol{\omega}_B + \mathbf{J}_R\boldsymbol{\omega}_R + \mathbf{J}_L\boldsymbol{\omega}_L, \\ \mathbf{J}_R = & \mathbf{T}_{BR}\mathbf{J}_{R,R}\mathbf{T}_{BR}^\top, \mathbf{J}_L = \mathbf{T}_{BL}\mathbf{J}_{L,L}\mathbf{T}_{BL}^\top \end{aligned} \quad (2.32)$$

Therefore, the dynamical equations are given by

$$\begin{aligned}\mathbf{M} = & mS(\dot{\mathbf{r}}_{cg})\mathbf{u}_B + mS(\mathbf{r}_{cg})\dot{\mathbf{u}}_B + mS(\boldsymbol{\omega}_B)S(\mathbf{r}_{cg})\mathbf{u}_B + \mathbf{J}\dot{\boldsymbol{\omega}}_B + \dot{\mathbf{J}}\boldsymbol{\omega}_B \\ & + S(\boldsymbol{\omega}_B)\mathbf{J}\boldsymbol{\omega}_B + \mathbf{J}_R\dot{\boldsymbol{\omega}}_R + \dot{\mathbf{J}}_R\boldsymbol{\omega}_R + S(\boldsymbol{\omega}_B)\mathbf{J}_R\boldsymbol{\omega}_R \\ & + \mathbf{J}_L\dot{\boldsymbol{\omega}}_L + \dot{\mathbf{J}}_L\boldsymbol{\omega}_L + S(\boldsymbol{\omega}_B)\mathbf{J}_L\boldsymbol{\omega}_L,\end{aligned}\quad (2.33)$$

where

$$\begin{aligned}\dot{\mathbf{J}}_R &= \mathbf{T}_{BR}(S(\boldsymbol{\omega}_R)\mathbf{J}_{R,R} - \mathbf{J}_{R,R}S(\boldsymbol{\omega}_R))\mathbf{T}_{BR}^\top, \\ \dot{\mathbf{J}}_L &= \mathbf{T}_{BL}(S(\boldsymbol{\omega}_L)\mathbf{J}_{L,L} - \mathbf{J}_{L,L}S(\boldsymbol{\omega}_L))\mathbf{T}_{BL}^\top, \\ \dot{\mathbf{J}} &= \dot{\mathbf{J}}_R + \dot{\mathbf{J}}_L,\end{aligned}\quad (2.34)$$

and

$$\mathbf{M} = \mathbf{M}_{\text{aero}} + S(\mathbf{r}_{cg})m \begin{bmatrix} -g \sin \theta \\ g \cos \theta \sin \phi \\ g \cos \theta \cos \phi \end{bmatrix}\quad (2.35)$$

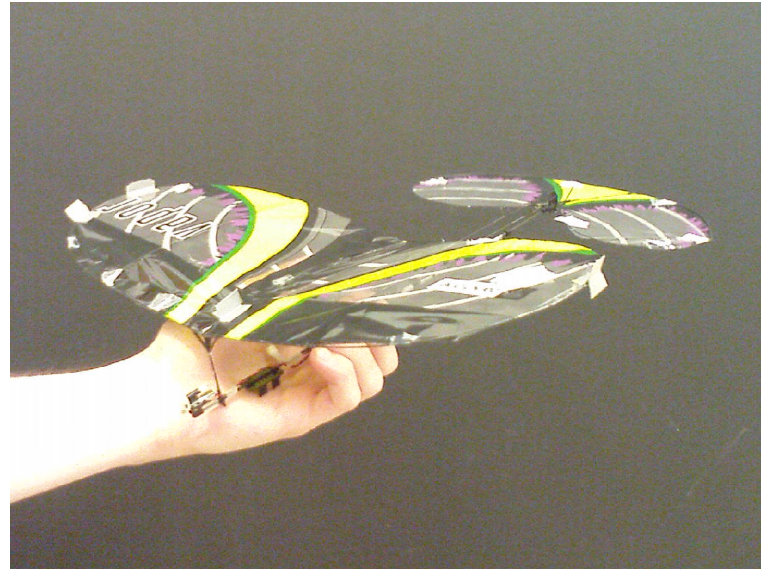
In the above equations, $\mathbf{J}_{R,R}$ and $\mathbf{J}_{L,L}$ denote the moments of inertia of the right and left wings, respectively, in their respective local coordinate frames based at the wing root.

2.9 Aerodynamic Model for Trim Calculations

The aircraft model considered in this chapter is derived from the Vapor shown in figure 2.2(a)* by removing the vertical tail and the propeller. To simplify the analysis, the aerodynamic contributions of the fuselage and the propulsive mechanism are neglected with the understanding that they can be readily added within the conceptual framework of this chapter. The wings have an elliptic planform. As explained in the next section, the problem of adverse yaw in the absence of a vertical tail may be ameliorated by placing the CG behind the wing AC. The dimensions of the Vapor are similar to those of small birds such as the barn swallow shown in figure 2.2(b) †. The lift and drag coefficients of the wing and tail airfoils, adapted from values determined experimentally [102] for

*<http://www.parkzone.com/Products/Default.aspx?ProdID=PKZ3380>.

†http://commons.wikimedia.org/wiki/File:Barn_swallow_6909.jpg.



(a) ParkZone®Vapor: the aircraft model considered in the chapter
(without the vertical tail).



(b) A barn swallow (source:wikimedia.org)

Figure 2.2: The figure on the left shows ParkZone®Vapor, the aircraft model used for numerical analysis. The size of the Vapor is similar to that of small birds such as the barn swallow shown on the right.

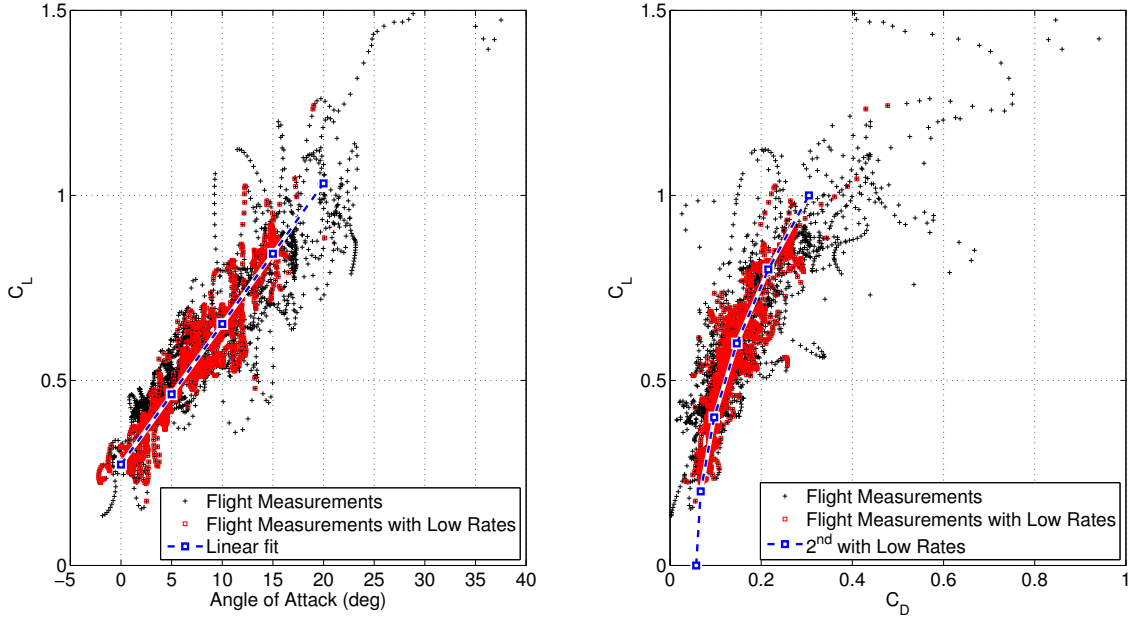


Figure 2.3: Experimentally obtained aerodynamic data [102].

the Vapor itself (shown in figure 2.2(a)) at a Reynolds number of 20000, are given by

$$C_L = 0.28295 + 2.00417\alpha, \quad C_D = 0.0346 + 0.3438C_L^2, \quad (2.36)$$

where α is measured in radians. Using thin airfoil theory [48], it was determined that $C_{mac} = -0.1311$. The actual experimental plot has been shown in figure 2.3. The C_L and C_D expressions in equation (2.36) are obtained by averaging *only* over the red points in figure 2.3. The rest of the points in figure 2.3 (marked in black) represent data collected at high values of pitch rate and $\dot{\alpha}$, and are not relevant to the discussion. During the experiments, for $\alpha > 25$ deg, $\dot{\alpha}$ was seen to be substantial, and therefore, the coefficients in equation (2.36) are reliable only up to $\alpha = 25$ deg.

The aircraft weighs 12 grams, including a ballast mass added to the nose of the aircraft for placing the CG around half-wing-chord under nominal conditions; i.e., when the wing dihedral and incidence are both zero. The aircraft is 29.7 cm long from nose to tail, and under nominal conditions, the distance between the AC and the CG is $x_{ac} = 3.6$ cm. The horizontal tail is located 26.1 cm behind the wing root AC. The limiting value of the horizontal tail deflection is assumed to be 30 deg in both directions. The limiting value of the wing dihedral is assumed to be 60 deg on either side, while that of the wing incidence is 15 deg.

2.10 Chapter Summary

In this chapter, we derived the equations of motion for an MAV with flexible articulated wings. The dynamics model was complete in that it accounted for the nonlinear equations of motion, effects of CG movement, contributions from wing deformation as well as nonlinear aerodynamics. In the next two chapters, we use the model described above for a trim and stability analysis of the articulated wing MAV described in the previous section.

Chapter 3

Performance and Stability of a Rigid Aircraft

This chapter describes the main results for the dynamics of a rigid aircraft. The effectiveness of wing dihedral for yaw control is compared with that of the vertical tail in Section 3.1. Sections 3.2.1 and 3.2.2 describe a linear analysis of lateral-directional stability and lay the foundation for a formal analysis of the control effectiveness of wing dihedral for yaw control in section 3.2.3 as well as the bifurcation analysis in sections 3.3.1 (longitudinal flight) and 3.3.2 (turning flight).

3.1 Comparison With the Vertical Tail

Figure 3.1 illustrates the physics underlying the use of wing dihedral as a control. Increasing the wing dihedral reduces the force acting in the body z -direction, and generates a side force. The reduced z -force affects the aircraft flight path angle and angle of attack, and hence the flight speed. On the other hand, the side force can be used for providing the centripetal force for turning, and as a source of the yawing moment. In particular, if the CG is located behind the line of action of the side force, then a positive side force produces a positive yawing moment and vice-versa (see figure 2.1 for the sign conventions). It follows that a positive rolling moment (wherein the lift on the left wing is higher than the right wing) is accompanied by a positive yawing moment if the wings have a positive dihedral deflection. Consequently, the adverse yaw produced due to rolling is reduced.

Figure 3.1 qualitatively suggests candidate dihedral deflections of the two wings in order to perform a turn. For example, to turn right, the left wing could be deflected upwards and the right wing downwards about a symmetric setting. While such a setting would provide the required side force, it could lead to an adverse yaw moment arising from the z -axis projections of the pitching moments about the AC of the two wings. The adverse yaw moment, which would be produced by

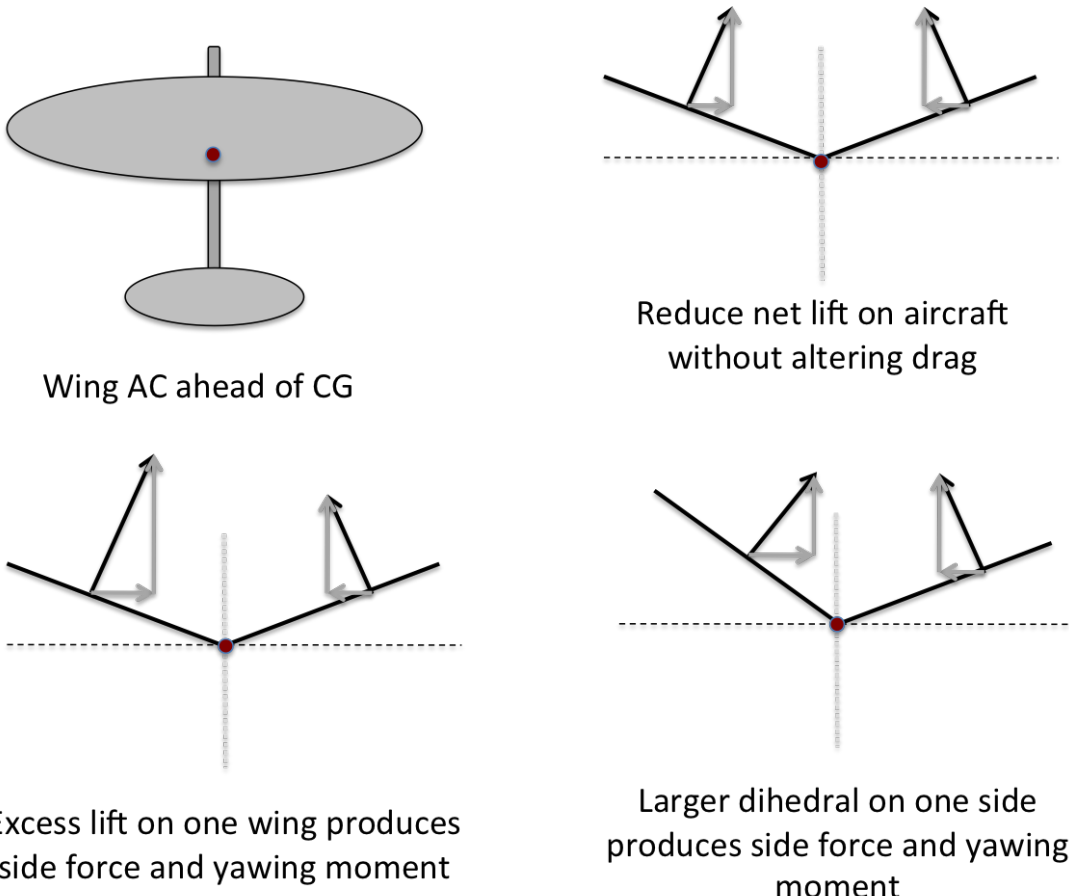


Figure 3.1: Illustration of the physics underlying the use of dihedral as a control. The dark conspicuous dot in the figures is the aircraft CG.

wings with substantial positive camber, could potentially inhibit the turn.

In order to appreciate the utility and the limitations of using differential dihedral as a yaw control mechanism, the yawing moment produced by the differential dihedral should be compared with that of a conventional vertical tail. In order to provide a basis for a fair comparison, the deflection of the tail and the differential dihedral are kept identical. Consider a rectangular vertical tail with a span b_t , chord c_t , area $S_t = b_t c_t$, and located at a distance l_t behind the CG. The wing has a semi-span $b/2$ and chord c . Let the S_w denote the area of each wing, and let l_w denote the x component of the moment arm of the side force with respect to the CG, where $l_w > 0$ is the wing AC is ahead of the CG. The yawing moment produced by the vertical tail is calculated by assuming that the dihedral deflection of both wings is zero. In order to simplify the analysis, let α_w denote the effective angle of attack of the wing; i.e., $C_L(\alpha) = C_{L\alpha} \alpha_w$. Generally, $\alpha_w \neq \alpha$ for

cambered wings.

Assuming a linear relation between the lift and the angle of attack, the yawing moment generated by the tail for a deflection $\beta_t > 0$ is equal to $N_t = q_\infty S_t l_t C_{L_\alpha} \beta_t$, where q_∞ is the dynamic pressure. The moment generated by a dihedral deflection, δ , of the left wing, while that of the right wing is zero, is given by

$$N_w = q_\infty S_w (l_w C_{L_\alpha} \alpha_w + c C_{m_{ac}}) \delta \quad (3.1)$$

If $\beta_t = \delta$, then the dihedral effectiveness ratio, $\zeta = N_w/N_t$, is given by

$$\zeta = \frac{S_w l_w}{S_t l_t} \alpha_w + \frac{S_w c}{S_t l_t} \frac{C_{m_{ac}}}{C_{L_\alpha}} \quad (3.2)$$

Clearly, the dihedral is more effective for yaw control at high angles of attack. Equation (3.2) also suggests that the dihedral is better than the vertical tail when l_t is small. The ability to change wing dihedral is built into birds in the form of their ability to flap their wings for propulsion. Hence, no additional mechanisms are needed for yaw control. Ornithopters, too, can benefit from differential dihedral-based yaw control in a similar manner.

Remark: For positively cambered wings, $C_{m_{ac}} < 0$. Hence the second term on the right hand side of (3.2) is negative and not only reduces ζ , but could also render it negative. In the latter case, the left wing could be deflected downwards, or the right wing could be deflected instead of the left wing. Alternately, if the wing camber can be controlled independently, the camber could be chosen to make $C_{m_{ac}}$ small enough so that the dihedral effectiveness ratio, ζ , is positive. There is no evidence in the literature to suggest whether birds perform cambering for the aforementioned purpose. It is known that cambering can be used for other purposes such as high lift generation, delaying stall and flutter prevention [8]. From a design perspective, the argument stated here suggests that the wing airfoil should be chosen with as small a camber as possible when the wing dihedral is to be employed for yaw control.

The idea of using wing dihedral for control is particularly useful when the wings are flexible, because flexible wings bend and twist spontaneously under aerodynamic loading. The dihedral angle at a given point on the wing is equal to the sum of the slope of the bending displacement

and the wing slope at the root. Since bending and twisting are coupled, wing twist can be used to bring about a passive proverse change in the wing dihedral.

3.2 Theoretical Analysis of the Role of Wing Dihedral

A brief theoretical analysis is in order before a computational analysis is performed. The objectives of the next three subsections are to (a) derive analytical expressions for estimating the contribution from the wings to force and moment derivatives, (b) identify the lateral modes using the standard fourth order model [1], and (c) estimate the sign of the control effectiveness of asymmetric dihedral for turning.

3.2.1 Analytical Approximations to Lateral-Directional Stability

The lift and drag forces produced by the wing as well as their moments about the origin of the body frame can be resolved along the body axes. In particular, summing the body axis components of the net moment due to lift and drag yield the net rolling, pitching and yawing moments. Stability of aircraft depends primarily on the three aerodynamic moments and their derivatives with respect to the aircraft angular velocity, angle of attack and sideslip.

Let α and β denote the angle of attack and sideslip; i.e., $w = u \tan \alpha$ and $v = V_\infty \sin \beta$ where u , v and w are components of the aircraft velocity along the aircraft body axes. Consider the aerodynamic center of a wing cross section, with coordinates $[x, y, 0]$ in the wing frame. Ignoring the angle of incidence of the wing with respect to the fuselage, the local wind velocity at the aerodynamic center in question is given by

$$\mathbf{v}_{\text{loc}} = \begin{bmatrix} u - y(q \sin \delta + r \cos \delta) \\ v \cos \delta - w \sin \delta + x(q \sin \delta + w \cos \delta) \\ v \sin \delta + w \cos \delta + py - x(q \cos \delta - r \sin \delta) \end{bmatrix} \quad (3.3)$$

If q is ignored to restrict the analysis to lateral-directional motion, it follows that the local angle of attack is given by

$$\alpha_{\text{loc}} \approx \frac{\beta \sin \delta + \alpha \cos \delta + \frac{py + rx \sin \delta}{u}}{1 - \frac{ry}{u} \cos \delta}, \quad (3.4)$$

which can be simplified further using binomial expansion of the denominator to yield

$$\alpha_{loc} \approx \beta \sin \delta + \alpha \cos \delta + \frac{py + rx \sin \delta}{u} + \frac{ry}{u} \alpha \cos \delta + \frac{pr y^2 \cos \delta}{u^2} \quad (3.5)$$

At low to moderate angles of attack, the net force along the body z -axis is approximated by $Z \propto \alpha_{loc}$. Furthermore, the rolling and yawing moments can be approximated by

$$L \propto Z_L - Z_R, \quad N \propto (Z_L \sin \delta_L - Z_R \sin \delta_R) \quad (3.6)$$

The lateral-directional derivatives can be approximated as follows:

$$L_\beta \propto -u^2(\delta_L + \delta_R), \quad L_p \propto -ub, \quad L_r \propto -uba \quad (3.7)$$

$$N_\beta \propto -u^2(\delta_L^2 + \delta_R^2), \quad N_p \propto -ub(\delta_L + \delta_R) + r \frac{b^2}{2}(\delta_L - \delta_R), \\ N_r \propto -uba(\delta_L + \delta_R) + \left(\frac{pb^2}{2} \right) (\delta_L - \delta_R) \quad (3.8)$$

Useful information about aircraft stability can be gleaned from equations (3.7) and (3.8), which has been tabulated in table 3.1.

Table 3.1: Stability derivatives for a tailless aircraft with an articulated wing

Derivative	Symmetric flight $(\delta_L = \delta_R = \delta)$	Turning flight $(\delta_L \approx -\delta_R)$	Stability condition
L_β	Stable	Stable when $\delta_L + \delta_R > 0$ (see section 3.2.3)	$L_\beta < 0$
L_p	Stable	Stable	$L_p < 0$
N_β	Unstable	Unstable	$N_\beta > 0$
N_r	Stable (drag reduces stability)	Unstable, but stable when $\text{sign}(p) \neq \text{sign}(\delta_L - \delta_R)$	$N_r < 0$

Based on the results in table 3.1, it is clear that the aircraft would be expected to be unstable in most flight regimes. At least two stability derivatives suggest the possibility of stability in some select turn regimes. However, in rapid turn regimes, the flight dynamics are far too strongly coupled to draw reliable conclusions from this linear, decoupled analysis. Furthermore, because the stability derivatives depend strongly on the wing dihedral angle, which is in turn a function of the aircraft maneuver, it follows that stability is tied very closely to the nature of the maneuver being executed.

The observation is peculiar to aircraft with articulated wings. In conventional aircraft with fixed wings, although stability derivatives depend on aircraft states, they are essentially independent of the control surface deflection.

3.2.2 Lateral-Directional Stability

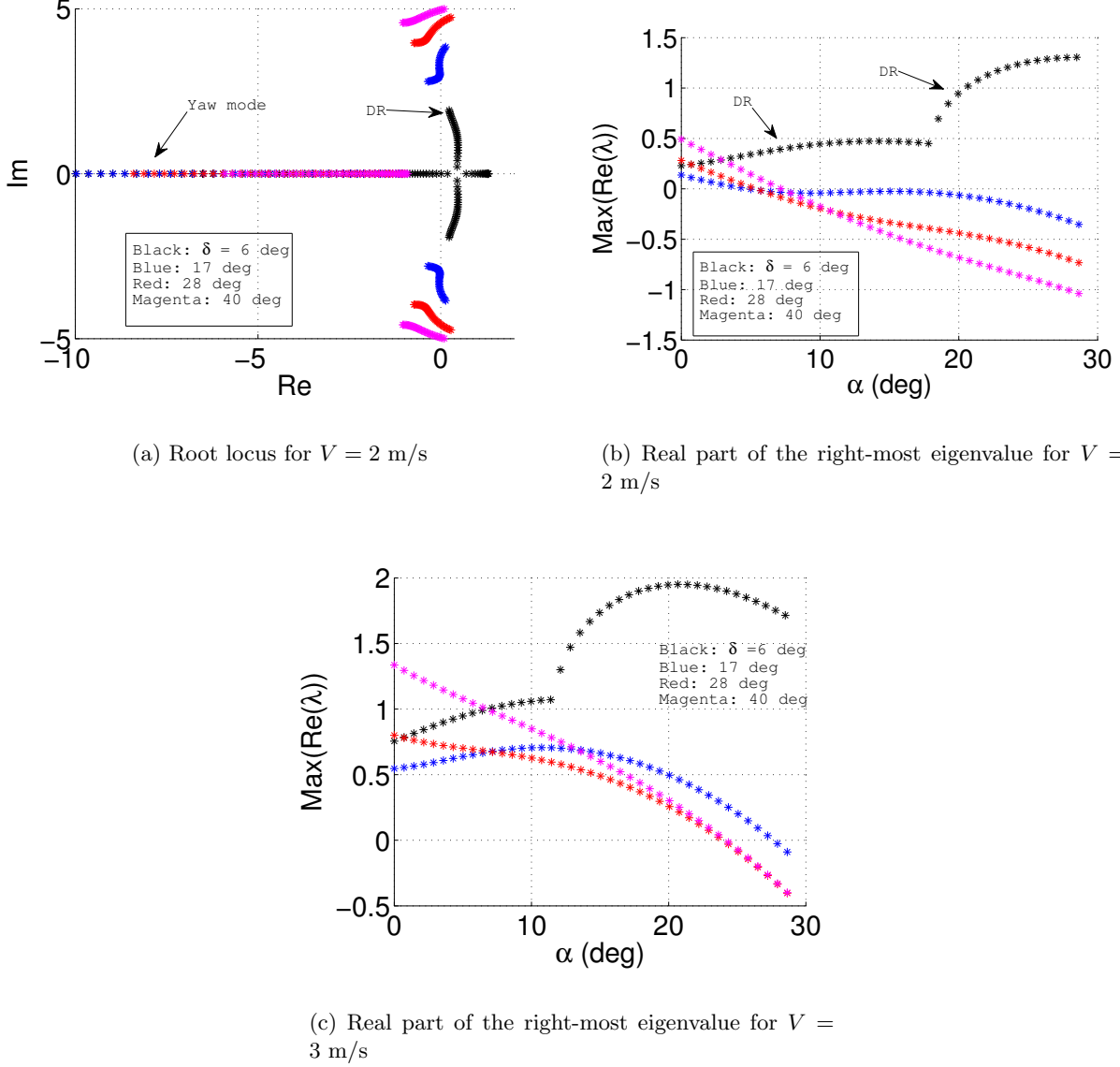


Figure 3.2: Root locus plot showing lateral-directional eigenvalues as functions of the angle of attack for candidate symmetric wing dihedral deflections. The roll mode is not shown in the root locus plot. The real part of the right most eigenvalue is a measure of the stability margin when the system is stable.

Figure 3.2(a) shows the root locus plot for a sample flight speed of 2 m/s. The highly stable roll mode is not shown here. The root locus plot is obtained by varying the angle of attack for four candidate symmetric dihedral deflections: 6 deg (black), 17 deg (blue), 28 deg (red), and 40 deg (magenta). The root locus plot helps to verify some of the observations in the section 3.2.1. The unstable stability derivatives observed in table 3.1 manifest in the form of an unstable Dutch roll mode. Figure 3.2(b) plots the real part of the right-most eigenvalue, which measures the stability margin of the dynamics. The Dutch roll mode is seen to stabilize around $\alpha = 7$ deg for three candidate dihedral deflections, except $\delta = 6$ deg. In the latter case, the complex conjugate Dutch roll eigenvalues merge on the real axis, and one eigenvalue moves to the right with increasing α worsening the instability. Clearly, the Dutch roll mode shows a qualitatively different, more desirable behaviour for large dihedral deflections.

Figure 3.2(c) is a plot of the real part of the right-most eigenvalue for $V = 3$ m/s. The effect of flight speed is summed up in the observation that the Dutch roll mode stabilizes at a much higher angle of attack for the three larger symmetric dihedral deflections. A strong dependence of stability characteristics on the flight speed is another feature of the low speed flight of MAVs. In contrast, the stability of faster, heavier fixed wing aircraft depends primarily on the angle of attack in pre-stall, incompressible flow regimes.

3.2.3 Control Effectiveness for Turning

The wing dihedral angles may be changed asymmetrically for executing turns as explained earlier in section 3.1. The challenge would be to design control laws for controlling the yaw rate and the roll rate, for which it is necessary to determine the control effectiveness of the wing dihedral. Specifically, the control effectiveness is measured in terms of incremental rolling and yawing moments generated by an incremental change in the wing dihedral angles.

A logical scheme for designing a yaw control law would be to use $\delta_L - \delta_R$ to control the turning rate. This is akin to controlling the aircraft bank angle as a function of the commanded turn rate. From equation (3.5), it is clear that the incremental change in α_{loc} is a nonlinear function of $\delta_L - \delta_R$ and it depends on angular velocity of the aircraft as well. Therefore, it is perfectly possible that the sign of the control effectiveness need not be uniform across the flight regime. The yaw control

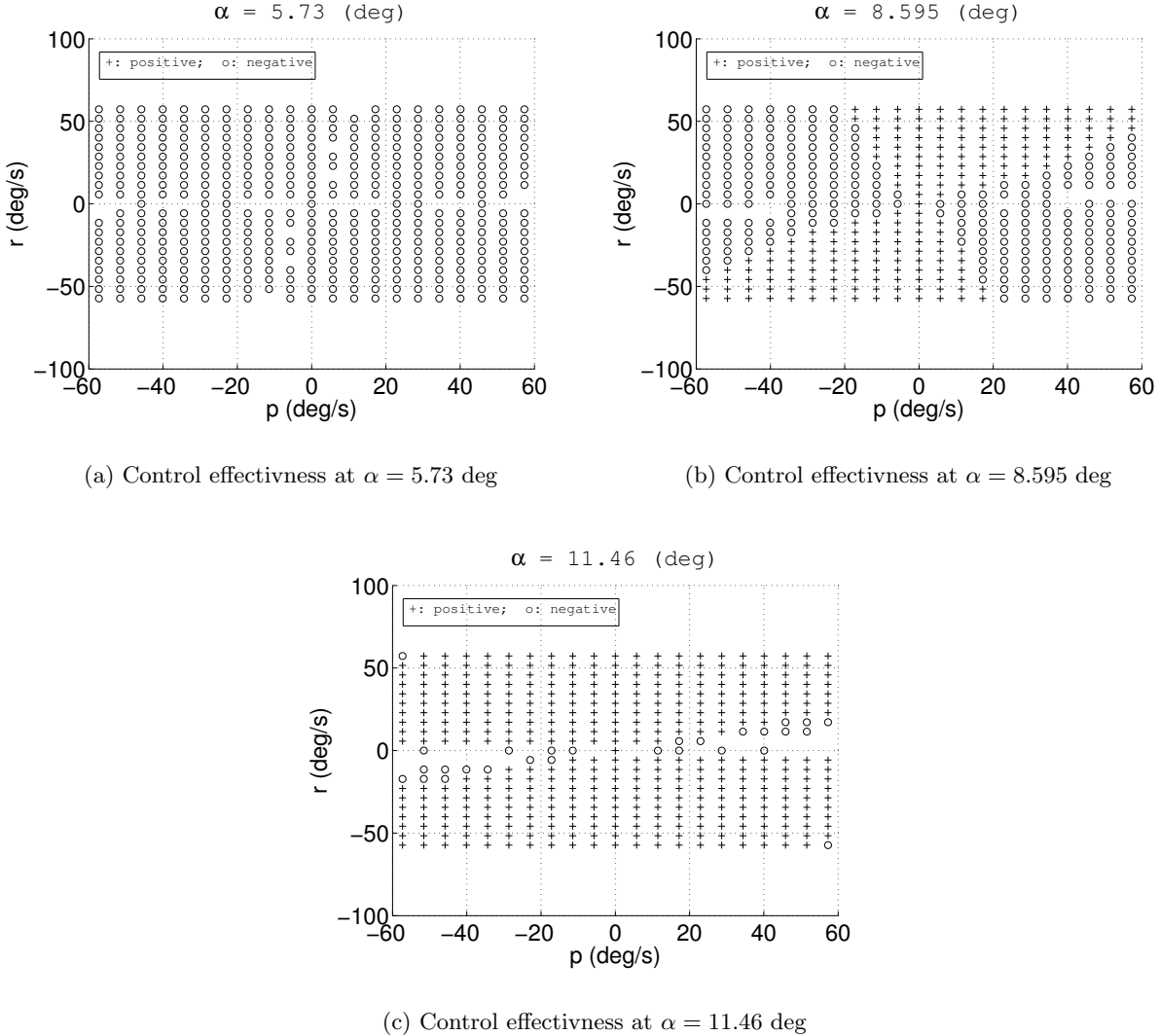


Figure 3.3: Plots showing the sign of the control effectiveness, $\text{sign}\left(\frac{\Delta N}{\Delta(\delta_L - \delta_R)}\right)$, as a function of the angle of attack, roll rate and yaw rate.

effectiveness is particularly interesting because of its strong sensitivity to the dihedral angles.

Figures 3.3(a) - 3.3(c) plot the sign of the control effectiveness, i.e., $\text{sign}\left(\frac{\Delta N}{\Delta(\delta_L - \delta_R)}\right)$, on a $p - r$ grid for angles of attack of 5.73 deg (0.1 rad), 8.595 deg (0.15 rad) and 11.46 deg (0.2 rad). The plots clearly show that the sign of the control effectiveness is negative at low angles of attack. The sign depends strongly on the angular rates between angles of attack of 6 deg and 12 deg, and it is positive uniformly thereafter. The sign of the control effectiveness is usually assumed to be known *a priori* while designing control laws. The challenge involved in designing a sound turning flight

controller is captured in figure 3.3.

3.3 Trim and Stability Analysis

3.3.1 Stability and Longitudinal Performance of Symmetric Configurations

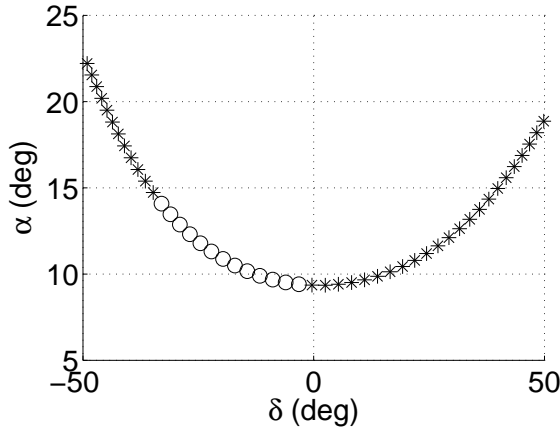
This subsection illustrates the effect of dihedral on the performance and stability when the aircraft configuration is symmetric; i.e., $\delta_R = \delta_L = \delta$. The wing incidence and sweep are both set to zero.

The following notation has been adopted for the bifurcation diagrams: an asterisk '*' denotes an unstable equilibrium where eigenvalues with positive real parts are all real. Conversely, an empty circle 'o' denotes an unstable equilibrium where the eigenvalues with positive real parts arise in complex conjugate pairs. A filled circle (.), occasionally coloured for clarity, denotes an unstable equilibrium where the eigenvalues with positive real parts consist of real as well as complex conjugate eigenvalues. Bifurcation points denote a qualitative change in the stability of the aircraft. Interestingly enough, no stable trims were observed for the aircraft.

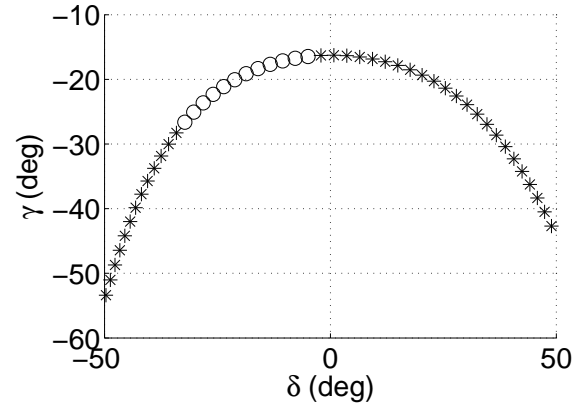
A key observation is that the use of symmetric dihedral offers the possibility of independently controlling two of the three longitudinal performance metrics, viz. the flight speed, angle of attack and the flight path angle. This cannot be achieved in fixed wing aircraft without variable thrust or variable dihedral. The Euler pitch angle would be an enterprising addition to the list of variables, with applications to airborne visual tracking of other airborne vehicles or ground-based objects.

Figures 3.4(a) and (b) show the flight path angle and the angle of attack, respectively, as functions of the wing dihedral angle when the flight speed is held at an arbitrarily chosen value 2.8 m/s. The wing dihedral is varied between -50 and 50 deg, and figure 3.4(c) shows the elevator schedule, as a function of the wing dihedral, required to maintain the aforementioned flight speed.

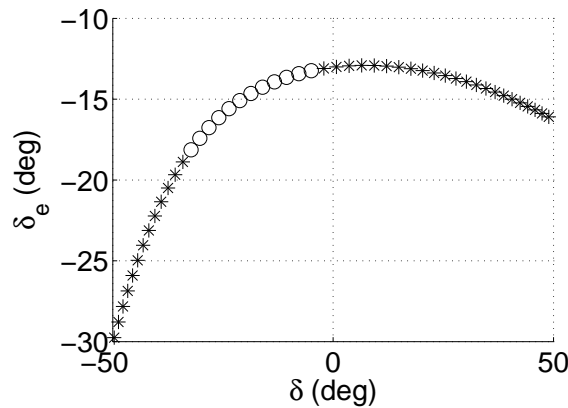
All the equilibria are laterally unstable. It is worth pointing out that the longitudinal modes are stable. The equilibria in the small patch between $\delta = -33$ deg and $\delta = 0$ are unstable with a pair of complex conjugate values, while for all other equilibria, the positive eigenvalues are real. An aircraft trimmed at any of these equilibria would diverge away from it, and the post-departure behaviour can be determined only after further trim analysis or simulations. The steady states constituting post-departure behaviour would not be routinely flown by the aircraft and, as such,



(a) Angle of attack as a function of dihedral.



(b) Flight path angle as a function of the dihedral

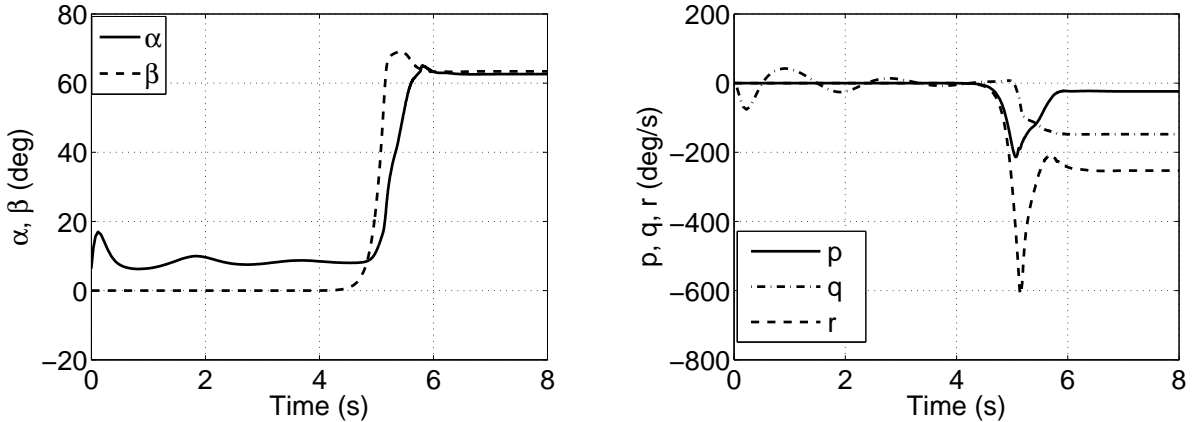


(c) Elevator as a function of the dihedral

Figure 3.4: Bifurcation diagrams showing γ and α versus symmetric dihedral (i.e., $\delta_R = \delta_L = \delta$), and the corresponding elevator deflection to hold the speed fixed at $V = 2.8$ m/s. An asterisk (*) denotes equilibria where eigenvalues with positive real parts are all real. Circles (o) denote equilibria where all eigenvalues with positive real parts have non-zero imaginary parts.

they would represent highly undesirable flight conditions. Hence, no attempt has been made to determine the post-departure steady states as part of the bifurcation analysis.

Figure 3.5 shows a simulated time history of the aircraft motion. The wing dihedral angles were both set to 10 deg, while the elevator was set to -10 deg. The initial angle of attack was 5 deg, while all the lateral variables (β, p, r, ϕ) were set to zero. The aircraft seems to stabilize for the first 4 seconds before departing rapidly into a fast spin-like dive. Since the initial value of all lateral states was zero, and the longitudinal modes are stable, the aircraft tends to stabilize itself



(a) Angle of attack and sideslip time histories.

(b) Time histories of the roll, pitch and yaw rates.

(c) Trajectory in the x, y, z plane

Figure 3.5: Simulated time history of the aircraft motion with the dihedral angle of both wings fixed at 10 deg. All lateral variables, namely the sidelip, roll rate, yaw rate and the Euler roll angle, were initialized at zero.

in the absence of any lateral inputs or disturbances. The lateral variables acquire non-zero values from numerical integration errors. The sideslip and the lateral angular rates build up due to the lateral instability, while the pitch rate and angle of attack are affected by the lateral-longitudinal coupling.

Remark: Strictly speaking, the simulation time histories in figure 3.5 are of limited accuracy because the aerodynamic data is available up to an angle of attack of 25 deg only. However, the aforementioned explanation about aircraft stability is correct because it pertains to the low- α trim

Table 3.2: Four cases considered in this section and their physical significance

Dihedral angles	Incidence angles	Constraints	Physical significance
Symmetric, non-zero	Anti-symmetric	None	Turn using just the wing incidence
$\delta_R = 0, \delta_L$ freed	Anti-symmetric	$\beta = 0$	Turn and maintain zero sideslip
$\delta_L \neq \delta_R$ (asymmetric variation)	Zero	$\beta = 0$	Turn using only the wing dihedral and maintain zero sideslip
Asymmetric	Anti-symmetric	$\beta = 0,$ V prescribed	Compute achievable turn rate for given speed and maintain zero sideslip.

states.

3.3.2 Lateral Stability and Performance

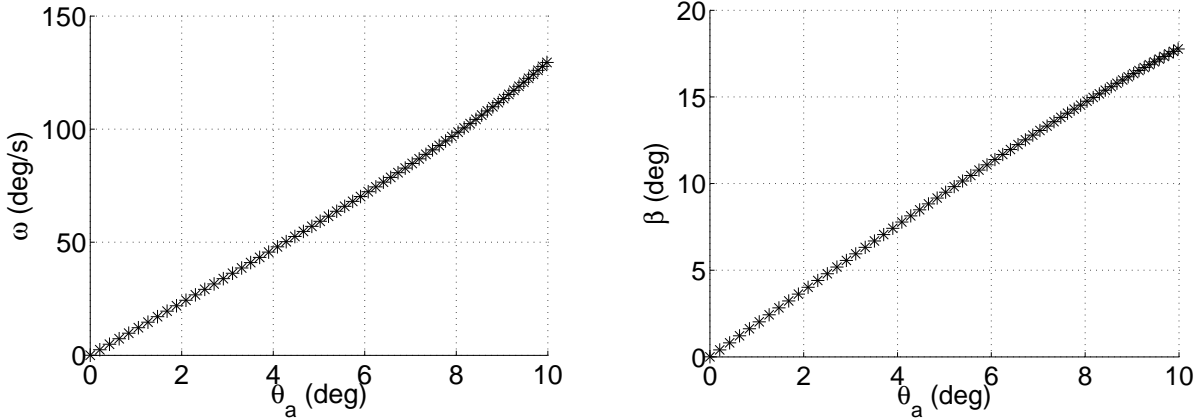
The wing incidence angles can be set anti-symmetrically on the two wings to generate rolling moment, and differential dihedral can serve as a yaw control mechanism as explained earlier in Sec. 3.1. The equilibrium turn rate, defined in equation (2.19), is an important agility metric for an aircraft [45]. Bifurcation analysis is used for analysing performance and stability for the four benchmark cases in table 3.2.

Case 1 (Variable $\theta_L; \theta_R = -\theta_L; \delta_L = \delta_R$ held fixed.)

Consider the first case where the wing incidence is varied anti-symmetrically. Physically, this case represents a turn without any dedicated yaw control mechanism. Instead, the roll rate generated by the anti-symmetric wing incidence angles, coupled with the dihedral effect modelled in section 3.2.1, leads to a yawing moment which, in turn, generates yaw rate. Because there is no dedicated yaw controller, the sideslip is not regulated and grows with increasing turn rate.

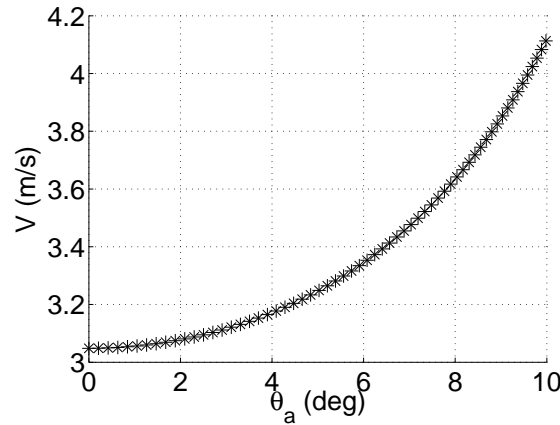
Figures 3.6(a) - (c) plot the turn rate ω , sideslip angle β and the flight speed V as functions of the incidence angle when $\delta = 29$ deg. It is observed that large values of turn rate are achieved with relatively small values of wing incidence. The sideslip angle and the flight speed increase as the turn rate increases with increasing wing incidence. The sidelip angle eventually builds up to nearly 18 deg, while the flight speed is consistently greater than 3.1 m/s. All trim solutions are seen to be unstable with a positive real eigenvalue.

Given the subsequent increase in sideslip and flight speed with increasing turn rate when the dihedral angles on the two wings are equal and constant, it is valid to ask whether rapid turns can



(a) Turn rate (ω) as a function of antisymmetric wing incidence (left wing positive)

(b) Sideslip (β) as a function of antisymmetric wing incidence



(c) Flight speed (V) as a function of antisymmetric wing incidence

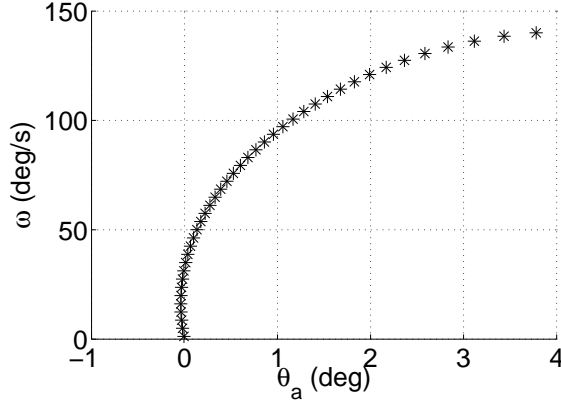
Figure 3.6: Case 1: Turn rate, sideslip and flight speed as functions of the anti-symmetric wing incidence. The wing dihedral angles were fixed at 29 deg.

be performed while maintaining zero sideslip and a prescribed flight speed. An alternate way of restating this question is to ask whether an arbitrary desired turn rate can be achieved for a given flight speed and with zero sideslip. In order to accommodate constraint equations corresponding to zero sideslip and constant flight speed, the corresponding control parameters, in this case the dihedral angles of both wings, are “freed,” i.e., treated as state variables. The resulting larger set of equations is then solved to compute the aircraft trim states and control inputs needed to achieve those trims. In order to infer the stability of the trim states, the Jacobian corresponding to the

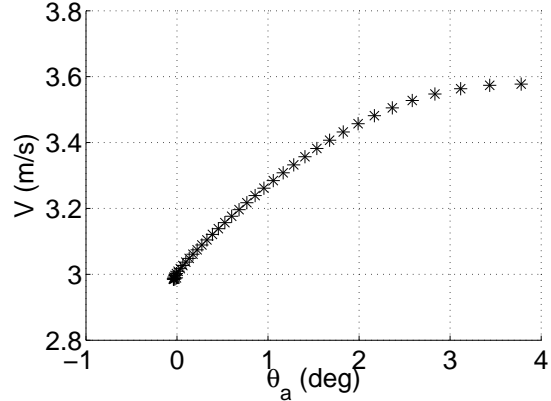
original set of differential equations is isolated, and its eigenvalues are computed.

Case 2 (Variable θ_L ; $\theta_L = -\theta_R$; δ_L free for $\beta = 0$; $\delta_R = 0$.)

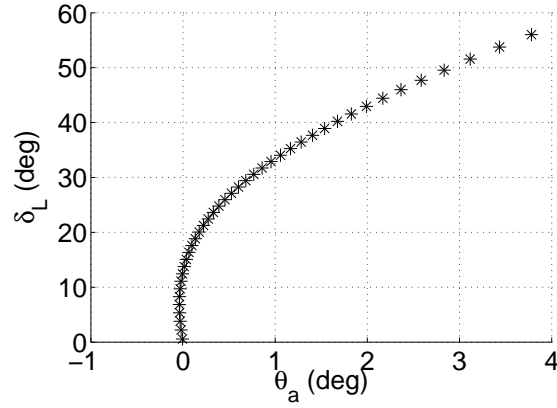
Consider the second case where the sideslip is required to be zero, while the flight speed is not constrained. The left wing dihedral is freed to provide the yawing moment necessary to regulate



(a) Turn rate (ω) as a function of antisymmetric wing incidence with constraint $\beta = 0$.



(b) Flight speed (V) as a function of antisymmetric wing incidence with constraint $\beta = 0$.



(c) Wing dihedral δ_L required to maintain $\beta = 0$.

Figure 3.7: Case 2: Coordinated turn trims as a function of anti-symmetric wing incidence.

sideslip to zero, while the right wing dihedral is held fixed at zero. As an alternative, the right dihedral may be scheduled to maintain some other flight parameter, as illustrated later in the section. Figures 3.7(a) - (c) plot the turn rate, the flight speed and the left wing dihedral as functions of the antisymmetric wing incidence. All trim solutions are seen to be unstable. Initially,

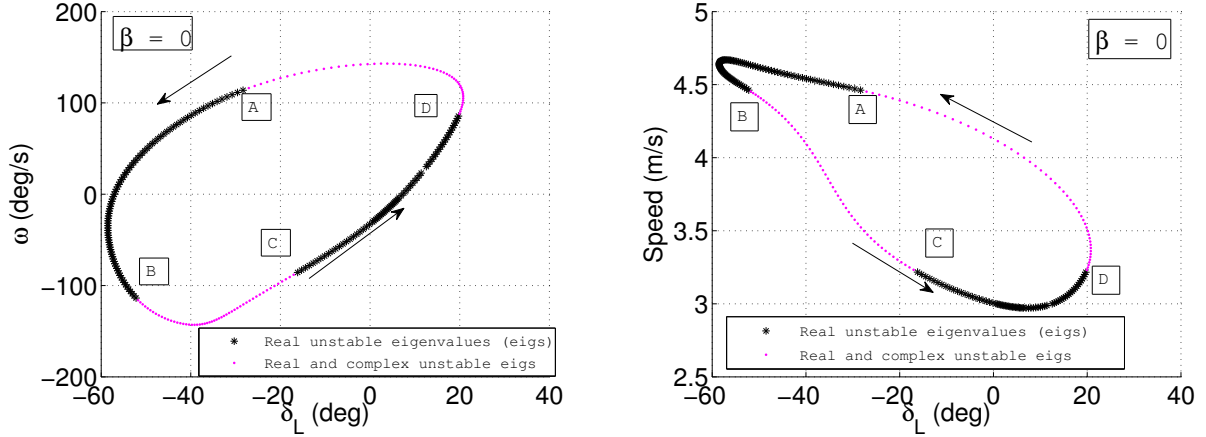
increasing ω and δ_L are accompanied by a reduction in the wing incidence. Thereafter, the turn rate and the left wing dihedral increase monotonically with the wing incidence. The dihedral angle required to maintain zero sideslip is close to its saturation value of 60 deg. when the wing incidence is 4 deg. and the corresponding value of turn rate is nearly 140 deg/s.

Remark: *This case represents the standard coordinated turn: the asymmetric wing incidence angles (like ailerons) are used to maintain roll equilibrium, while the left dihedral maintains equilibrium in yaw. The observation that the wing incidence angle is not very large suggests that controlling the wing dihedral angles alone may suffice to maintain the roll and yaw equilibrium across a range of turn rates.*

Case 3 ($\theta_L = \theta_R = 0$; Variable δ_L ; δ_R freed for $\beta = 0$)

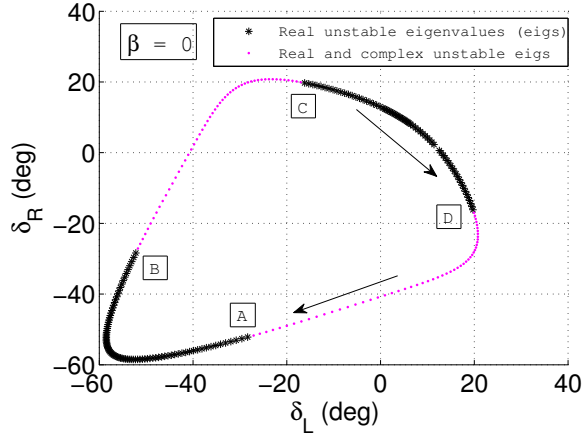
Consider the third case where the wing incidence is held fixed at zero. The left wing dihedral angle is varied independently, while the right wing dihedral is scheduled to maintain zero sideslip. This case is presented to show that the wing dihedral angles alone are capable of controlling a turn. Alternately, this case may be viewed as a redundancy to accommodate failures in the mechanism to control wing incidence. Physically, an asymmetric dihedral deflection of the wings leads to an asymmetry in the lift distribution on the two wings which, in turn, leads to rolling as well as yawing moments. The two moments can be controlled independently by choosing the wing dihedral angles appropriately.

Figures 3.8(a) - (c) plot the turn rate, flight speed and the right wing dihedral angle, respectively, as function of the left wing dihedral. The equilibrium surface topology is very different from Cases 1 and 2. The equilibrium surface is a closed loop. The left and right wing dihedral angles can be set to achieve fairly large turn rates, as evident in figure 3.8(a). Interestingly enough, a larger anhedral (negative dihedral) deflection is required of both wings as compared to the upward dihedral deflection. It is helpful to recall that a black asterisk '*' denotes an equilibrium with positive real eigenvalues, while a magenta filled circle (.) denotes an equilibrium with positive real as well as positive complex conjugate eigenvalues. It follows that the points A, B, C and D in figure 3.8 are Hopf bifurcations. In segments AD and BC, the aircraft demonstrates oscillatory behaviour with large angular rates, as in oscillatory spins. On the other hand, it diverges from segments AB and



(a) Turn rate as a function of the left wing dihedral, with $\beta = 0$.

(b) Flight speed as a function of the left wing dihedral, with $\beta = 0$.



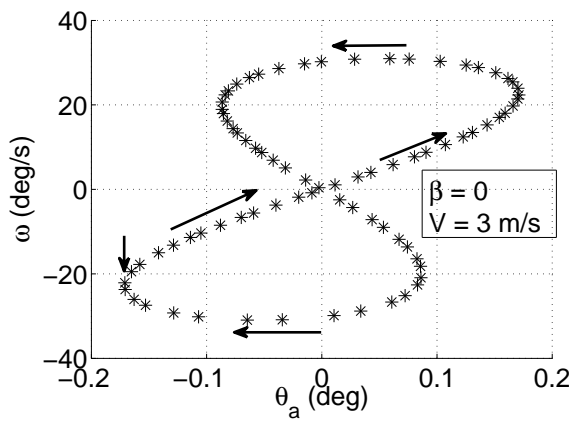
(c) Right wing dihedral required to maintain $\beta = 0$.

Figure 3.8: Case 3: Coordinated turn trims as functions of the left wing dihedral. The short arrow indicates a reference solution, while the long arrows track ω , V and δ_R as δ_L is varied. Points A, B, C and D are Hopf bifurcations.

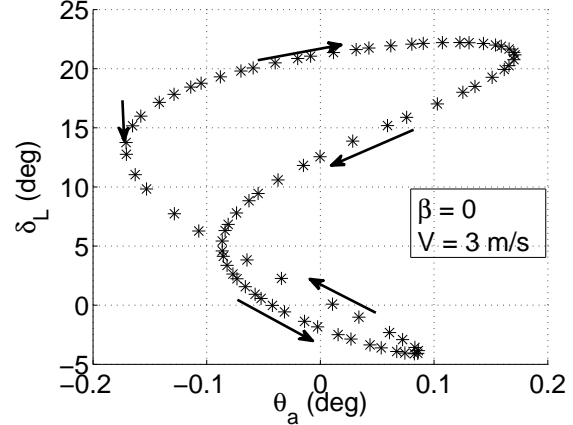
CD to *equilibrium* steady states not shown in figure 3.9.

Remark: This case serves as a useful pointer to control design. The aircraft would perform routine turns in the close vicinity of trims between the Hopf bifurcations C and D, which have a divergent yaw instability. When the trims between C and D are stabilized by linear yaw rate feedback, the following situation is observed [66]: the aircraft can be made to enter a rapid turn, but the same feedback law does not help it recover to straight and level flight. Instead, the aircraft performs limit

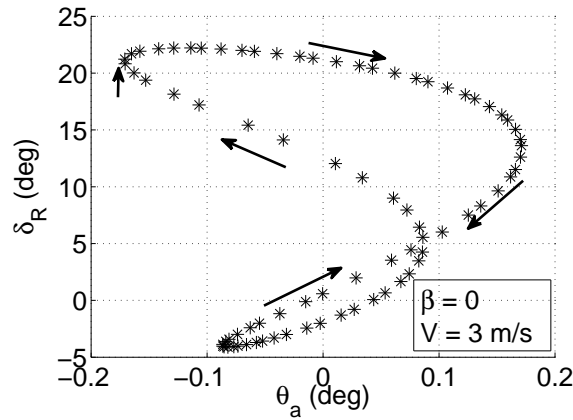
cycle oscillations, as one would expect from the existence of Hopf bifurcations C and D. Aircraft similar to the one considered here would exhibit similar nuances. Instead of a linear yaw rate feedback, a nonlinear yaw rate feedback is required to recover the aircraft to stable, wings level flight from of a turn.



(a) Turn rate as a function of the anti-symmetric wing incidence with constraints $\beta = 0$ and $V = 3 \text{ m/s}$.



(b) Left wing dihedral as a function of the anti-symmetric wing incidence with constraint $\beta = 0$ and $V = 3 \text{ m/s}$.



(c) Right wing dihedral required to maintain $\beta = 0$ and $V = 3 \text{ m/s}$.

Figure 3.9: Case 4: Coordinated turn trims with left and right wing dihedrals varied asymmetrically. Each plot carries two arrows. The short arrow denotes a reference solution, while the long arrow helps track the variation of the turn rate and δ_R starting from the reference solution.

Case 4 (Variable θ_L , $\theta_R = -\theta_L$; δ_L and δ_R freed for $\beta = 0$ and constant V)

Consider the fourth case, a turn where the flight speed is held constant at an arbitrarily chosen value of $V = 3.0$ m/s and the sideslip is regulated at zero. As in the first two cases, the wing incidence is varied as the independent parameter, while the two dihedral angles are freed to maintain the flight speed and the sideslip at their respective desired values. Figure 3.9(a) plots the turn rate as a function of the wing incidence. It is apparent that the wing incidence is much smaller than in figure 3.6, and the turn rate does not increase monotonically with wing incidence. Instead, the equilibria trace a figure-of-eight in figure 3.9(a) which limits the maximum attainable turn rate while, simultaneously, giving rise to multiple equilibrium solutions for a given value of wing incidence. All the equilibrium solutions are observed to be unstable. Figures 3.9(b) and 3.9(c) plot the left and right wing dihedral angles as functions of the wing incidence. The short arrow on each plot indicates a reference solution, and the long arrows help track ω , δ_L and δ_R as the wing incidence is varied. It is interesting to note that the wing dihedral angles become the primary drivers of the turn rate, while the wing incidence plays a secondary role in a coordinated turn at constant speed. Figure 3.10 is a 3-D plot of the turn rate and the wing dihedral angles and presents a clearer picture of the equilibrium surface topology. The projections of the closed curve in figure 3.10 onto the $\omega - \delta_L$ and $\delta_L - \delta_R$ planes are similar to figures 3.8(a) and 3.8(c).

Aircraft stability and performance are sensitive to the flight speed chosen for the turn which is, in turn, governed by the elevator deflection. In the above case, for example, in order to perform steady turns at 2.8 m/s instead of 3 m/s, the elevator deflection has to be increased beyond the previous value of -11.4 deg. The elevator was fixed at -13.7 deg (-0.24 rad) and steady turn trims were computed. Figure 3.11 shows the turn rate as a function of wing incidence when the dihedral angles on the two wings are scheduled to maintain the flight speed at 2.8 m/s and regulate the sideslip.

Remark: *Plots showing the dihedral angle variation are not included for brevity. A comparison of figures 3.9(a) and 3.11 shows that the maximum turn rate increases significantly when a lower flight speed is maintained. Furthermore, some of the turn equilibria are now unstable with a pair of positive complex conjugate eigenvalues. This could result, possibly, in an oscillatory behaviour with the resultant motion resembling spin owing to the significant turn rates.*

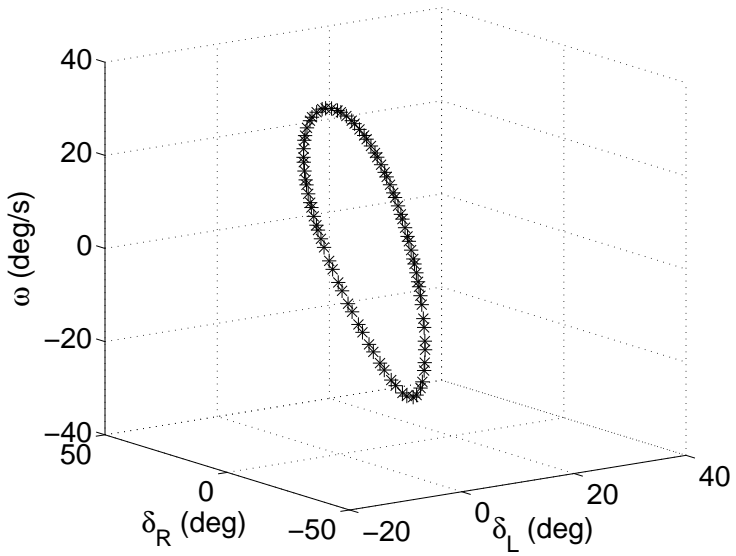


Figure 3.10: 3-D plot of the turn rate and the wing dihedral angles when the sideslip is held fixed at 0 and the flight speed at 3.0 m/s.

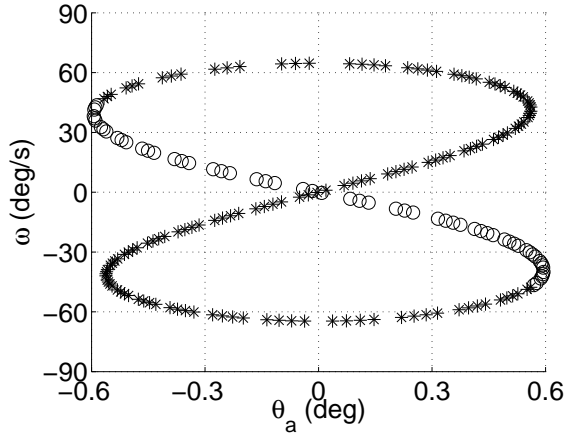


Figure 3.11: Turn rate as a function of anti-symmetric wing incidence with the constraints $\beta = 0$ and $V = 2.8$ m/s. Recall that asterisks ‘*’ and empty circles ‘o’ denote equilibria where all eigenvalues with positive real parts are real and complex conjugate, respectively.

3.3.3 Generalizations and Trade-Offs

The results in the aforementioned sections can be readily generalized to other similar aircraft. Although the numerical results were presented only for an aircraft based on the Vapor, it will be appreciated that they are based on a fundamental underlying concept whose validity does not depend on the aircraft to which it is applied. One could expect some quantitative changes with

aircraft geometry.

If the aircraft CG is located ahead of the wing AC, an asymmetric dihedral or an asymmetric force distribution on the wing would generate a yawing moment as explained in section 3.1.1. From figure 3.1, it follows that the yawing moment would be adverse in nature. At the same time, placing the CG ahead of the wing AC would increase the moment arm of the horizontal tail which would, in turn, improve the longitudinal performance and stability. Consider an aircraft rolling to the right. In this case, a positive proverse yawing moment can be obtained by deflecting the right wing upwards. Moreover, an upward deflection of the right wing leads to a proverse contribution from $C_{m_{ac}}$ as well. However, deflecting the right wing upwards would reduce the net side force. The reduction in side force would be beneficial while performing a pure roll, but it would be undesirable if the aircraft is rolling while turning to the right.

Now consider the configuration where the wing AC is ahead of the CG. This is the configuration which has been analysed in detail in this chapter. Recall (3.2)

$$\zeta = \frac{S_w l_w}{S_t l_t} \alpha_w + \frac{S_w c}{S_t l_t} \frac{C_{m_{ac}}}{C_{L_\alpha}} \quad (3.9)$$

It is evident that a negative wing $C_{m_{ac}}$, which results from a positive wing camber, has a detrimental effect on the dihedral effectiveness ratio ζ . One may be tempted to consider minimizing the camber to improve ζ , as suggested in section 3.1.1. However, note that α_w depends on the wing camber as well - it reduces with a reduction in camber. For a wing with no camber, $\alpha_w = \alpha$, the geometric angle of attack, and $C_{m_{ac}} = 0$. Therefore, the camber value could be chosen during design to maximize ζ .

The yawing moment that arises from an asymmetry in the wing configuration or aerodynamic force distribution can be traced to three sources. The primary source of yawing moment is the side force, illustrated in figure 3.1. The second source is $C_{m_{ac}}$, which was discussed in the last paragraph. The third source, which has not been discussed so far, is drag. A positive roll rate increases the angle of attack on the right wing, and a reduces that of the left wing. This leads to a higher drag on the right wing which contributes a proverse yawing moment. This stabilizing effect of drag is well known.

It is also evident from the discussion that the choice of the CG location involves a trade-off

between the longitudinal and lateral performance. Indeed, there are several merits in placing the CG behind the wing aerodynamic center, contrary to regular fixed wing aircraft with a vertical tail where the CG should be placed as far ahead as possible to improve the longitudinal as well as lateral performance.

3.4 Chapter Summary

In this chapter, we analysed the performance and stability of a rigid aircraft equipped with articulated wings. The key contributions of this chapter are: (a) identification of the problem of control effectiveness reversal, (b) literal approximations to the lateral stability derivatives, (c) trim and stability analysis of turning flight, and (d) the design pointers for wing camber and CG placement for ensuring the effectiveness of the dihedral-based yaw control mechanism.

In the next chapter, we will introduce the notion of effective dihedral for a flexible wing which will allow us to extend the literal approximations to a flexible-winged aircraft. We will also repeat the trim and stability analysis for a flexible winged aircraft. We will show that flexibility does not always bring about performance benefits compared to a rigid wing.

Chapter 4

Performance and Stability of a Flexible Aircraft

An experimentally derived steady aerodynamic model [102] is employed here. This is an admissible model because the wing is assumed to be statically deformed for the purpose of trim and stability analysis. The sectional aerodynamic coefficients for lift, drag, and pitching moment are given by

$$C_l = 0.28295 + 2.00417\alpha, \quad C_d = 0.0346 + 0.3438C_l^2, \quad C_{m,ac} = -0.1311 \quad (4.1)$$

The coefficient of lift, in particular, tallies very well with predictions from thin airfoil theory.

4.1 Analysis of the Wing and Effective Dihedral

The Young's modulus of the wing, E , may be considered as a design parameter. In order to exploit the idea of using the wing dihedral for yaw control, the wing dihedral effect itself may be looked upon as a design driver for E .

The role of differential (or asymmetric) dihedral for yaw control has been discussed in detail in Ref. [65]. The dihedral primarily produces a side force, which is actually a component of the total force produced by the wing normal to its local plane. Let Y_A and Z_A denote the local forces produced by the wing along the body y and z axes, respectively. Therefore, one may define a term called the effective dihedral, δ_{eff} , as follows:

$$\delta_{\text{eff}} = \tan^{-1} \left(\frac{\int_0^{b/2} Y_A(y) dy}{\int_0^{b/2} Z_A(y) dy} \right) \quad (4.2)$$

This notion of effective dihedral is different from, and arguably more general than, that of Rodden [79] who derived expressions for the increments, arising from the wing bending, in the rolling moment derivatives. The notion of effective dihedral is particularly useful for wing design from

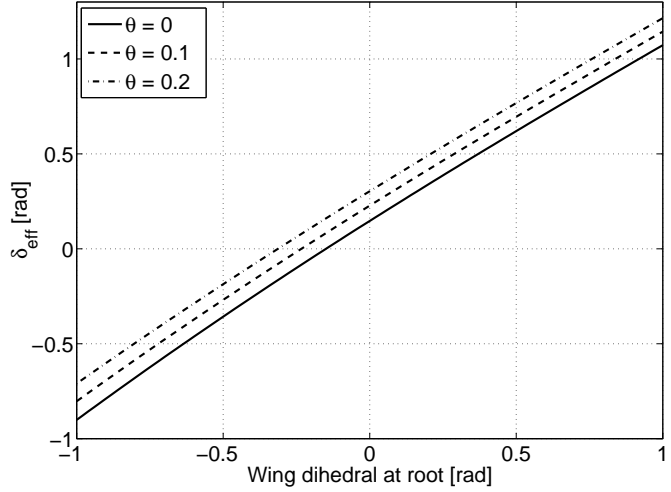
the point of view of elasticity. The Young's modulus, E , could be chosen to ensure that the wing produces a sufficient effective dihedral effect with reasonable actuator forces. The effective dihedral depends on the boundary conditions to which the wing is subjected whereas the boundary conditions themselves depend on the location and type of actuators. For a rigid wing, the effective dihedral and the actual dihedral are equal.

Figures 4.1(a) and 4.1(b) show the effective dihedral as a function of the wing dihedral angle at the root. The effective dihedral, as expected, is much higher for $E = 5 \text{ MPa}$ as compared to $E = 50 \text{ MPa}$. In the former case, the wing bending is large enough so that the flexibility provides a substantial increase in the wing dihedral effect. This suggests that for the particular wing geometry considered here, a material with a Young's modulus of $E \sim \mathcal{O}(1) \text{ MPa}$ should be chosen in order to obtain a significant dihedral effect. This conclusion depends on other chosen parameters and hence, such analysis should be performed on a case-by-case basis. Furthermore, it is important to note that the effective dihedral depends on the trim condition under consideration.

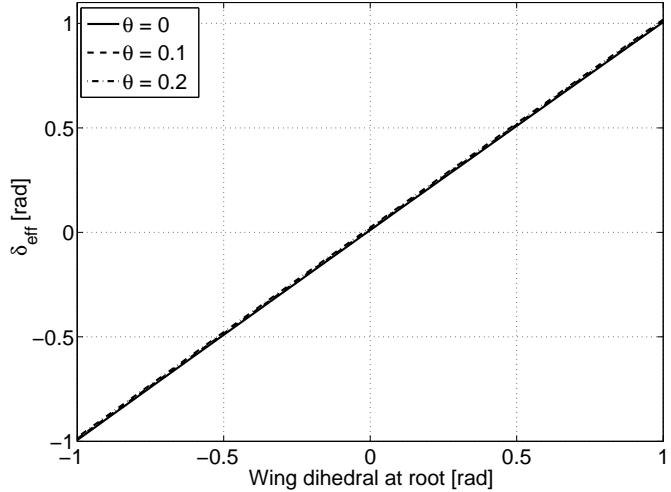
The effective dihedral is useful in another way. It forms the basis to extend the stability analysis for a rigid aircraft to the case of flexible wings. In Ref. [65], for example, analytical expressions for the traditional lateral stability derivatives were obtained for a rigid aircraft and the stability of lateral-directional modes was examined for various values of the wing dihedral. Those results would be applicable to a flexible-winged aircraft when the effective dihedral angle of the wing is matched to the dihedral angle of a rigid wing. This is valid regardless of the deformation profile of the wing. For the aircraft model considered here, it suggests that the motion stability would be similar to that of the rigid aircraft when $E \geq \mathcal{O}(10) \text{ MPa}$.

4.2 Feasibility of Using Wing Tension

At this point, it is helpful to note a design trade-off. A smaller E would provide a larger dihedral effect due to the aerodynamic loads on the wing. However, the same wing would be unable to generate as much anhedral because, usually, the wing would be expected to supply an upward lifting force. In principle, it seems that this limitation can be overcome by stiffening the wing internally. The effect of stiffening the wing on its effective dihedral effect is demonstrated in Fig. 4.2(a). The three curves in the figure correspond to tensions of zero, 5 g., and 10 g., respectively. The Young's



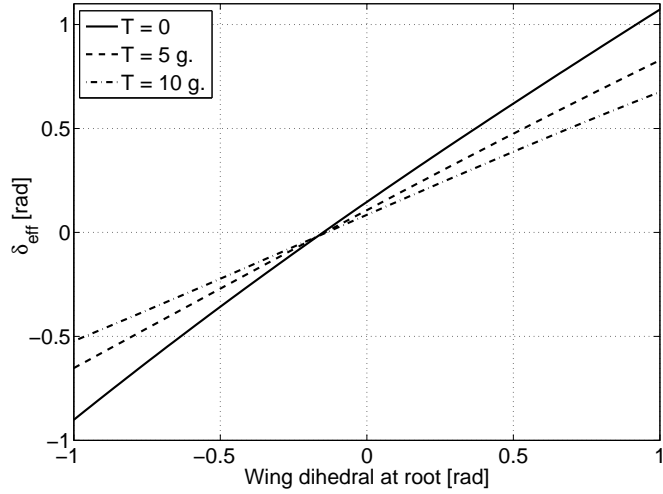
(a) Effective dihedral when $E = 5 \text{ MPa}$.



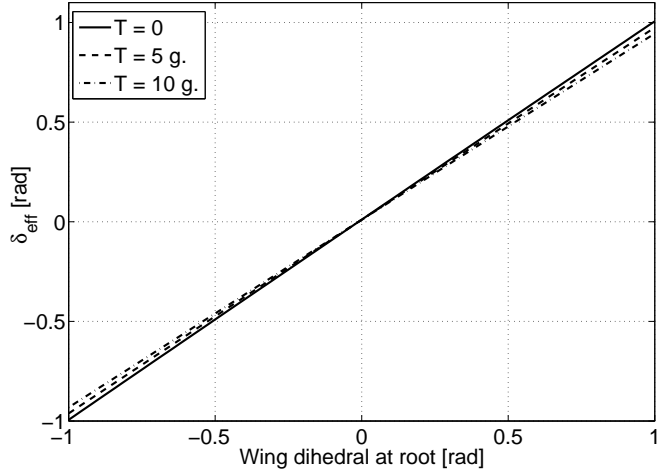
(b) Effective dihedral when $E = 50 \text{ MPa}$.

Figure 4.1: Effective dihedral as a function of the dihedral angle at the wing root for two different values of the Young's modulus. Each plot shows the effective dihedral for three values of wing tip twist (θ): 0, 0.1 rad and 0.2 rad. This plot was obtained for $V = 2.5 \text{ m/s}$ and $\alpha = 10 \text{ deg}$.

modulus was set to $E = 5 \text{ MPa}$. The tension values were chosen to be commensurate with the weight of the aircraft, with the understanding that servos similar to those which maneuver the wing should be able to provide these values of tension. Clearly, the effective dihedral decreases substantially with tension. The effect of tension becomes less significant as the Young's modulus



(a) Effective dihedral when $E = 5 \text{ MPa}$.



(b) Effective dihedral when $E = 50 \text{ MPa}$.

Figure 4.2: Effect of tension on the effective dihedral. The curves corresponding to a tension of zero, 5 g., and 10 g. are plotted. This flight speeds was set to $V = 2.5 \text{ m/s}$ and the angle of attack was $\alpha = 10 \text{ deg}$.

of the material is increased, as shown in Fig. 4.2(b). Whereas the conclusion is quite obvious, such analysis helps choose a suitable Young's modulus for the wing.

Interestingly, stiffening the wing not only reduces the effective dihedral of the wing, but it also flattens the curve of the effective dihedral as a function of the dihedral at the wing root.

Consequently, when a certain anhedral is required, the tensed wing will produce a lesser magnitude of anhedral as well.

4.3 Bending and Twist Natural Frequencies

Traditionally, natural frequencies of lifting surfaces are defined in terms of inertia and elastic stiffness. However, unsteady aerodynamic lift and moment relations contain terms which mathematically play the same role as stiffness, damping, and inertia in the governing relations. Consequently, another set of natural pseudo frequencies can be defined which include these aerodynamic contributions.

Consider the case where $\theta'(b/2) = \xi''(b/2) = \xi'''(b/2) = 0$. If ω_θ and ω_ξ denote the frequencies of the first (decoupled) twisting and bending modes, respectively, then it can be shown that [6]

$$\omega_\theta^2 = \frac{\pi^2}{4L^2} \frac{G\tilde{J}}{I_p} - \frac{M}{I_p}, \quad \omega_\xi^2 = \frac{12.36}{L^4} \frac{EI_b}{m} \quad (4.3)$$

where M denotes $\frac{\partial \mathbf{M}_{s,2}}{\partial \theta}$ (linearized twisting moment). In order to estimate the extent of time-scale separation, the ratio $\omega_\theta^2/\omega_\xi^2$ is of interest. Time-scale separation is a property wherein the dynamics consist of two sets of modes, one of which is significantly (at least an order of magnitude) faster than the other mode. The stability of each mode can be analysed independently, with other mode contributing a constant term whose value is a function of the mode being analysed. This property is used routinely for deriving literal approximations to aircraft dynamic modes [1]. The time-scale separation, if present, can also form the basis for the control design [105]. It must be noted that a sufficiently strong coupling between the two modes can alter the conclusions significantly. Therefore, caution must be exercised while drawing inferences from a time-scale-based analysis.

The ratio, $\omega_\theta^2/\omega_\xi^2$, will be estimated in section 6.6.1 in Chapter 6. We state a preview of the results. It turns out that for $\omega_\theta^2 > 0$ (i.e., to prevent torsional divergence), we need the material to be stiff enough. In fact, we derive the condition that $G > 7 \times 10^7$ when the wing thickness is assumed to be 1 mm. Second, the order of magnitude of the ratio ω_θ/ω_ξ is approximately 3. Therefore, twist dynamics are faster than bending. Finally, a glance at this derivation shows that the order of separation hinges essentially on two features: the low speed, the aspect ratio of the

wing and the geometry of the cross section. As the aircraft speed increases and the contribution from aerodynamics to ω_θ in Eq. (4.3) starts to dominate that from elasticity, the natural frequencies of bending and twist start converging towards each other increasing the possibility of the onset of flutter.

4.4 Bifurcation Analysis of Turning Flight

The performance and stability of an MAV equipped with flexible wings ($E = 5 \text{ MPa}$) in steady turning flight is analysed in a manner similar to that described for a rigid aircraft in Ref. [65]. A similar analysis could be repeated for other maneuvers of interest. Insofar as turning is concerned, wing flexibility may have one or more of several possible consequences.

1. The overall turn rate may improve because of the additional dihedral generated by the flexible wings.
2. Alternately, for a given turn rate, the dihedral angles required at the wing root would be reduced.
3. When the sideslip is not deliberately regulated, it would be reduced due to the enhanced dihedral effect.

It turns out that flexibility does result in a net improvement in the turn rate of the aircraft, but only when wing incidence angle at the root (or wing twist in general) is used actively. There is a significant reduction in the sideslip when the wings are locked in a symmetric dihedral configuration. However, when the dihedral angles alone are used for turns, the maximum achievable turn rate does not improve vis-a-vis a rigid aircraft. Furthermore, the magnitude of the commanded dihedral deflections required for a given turn rate is reduced in comparison to an aircraft with rigid wings.

4.4.1 Reduction in Sideslip (Variable $\theta_L; \theta_R = -\theta_L = -\theta_a; \delta_L = \delta_R$)

A turn is usually initiated by rolling the aircraft to the appropriate bank angle and followed by providing the appropriate yaw rate and pitch rate. When the flexible wings are twisted asymmetrically, the resultant roll rate causes a build-up in yaw rate due to the dihedral effect. However, if the wings

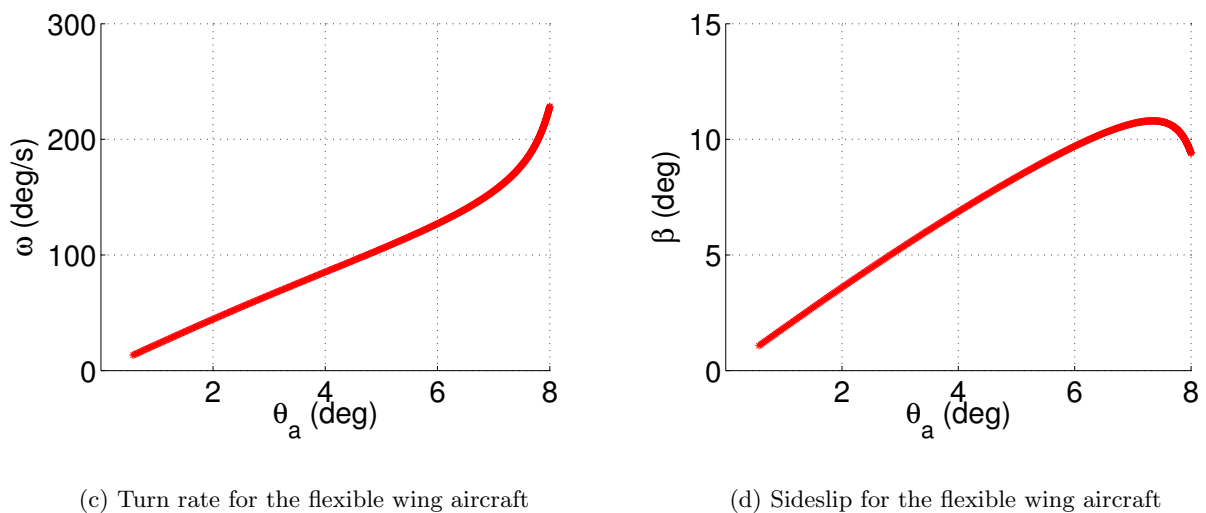
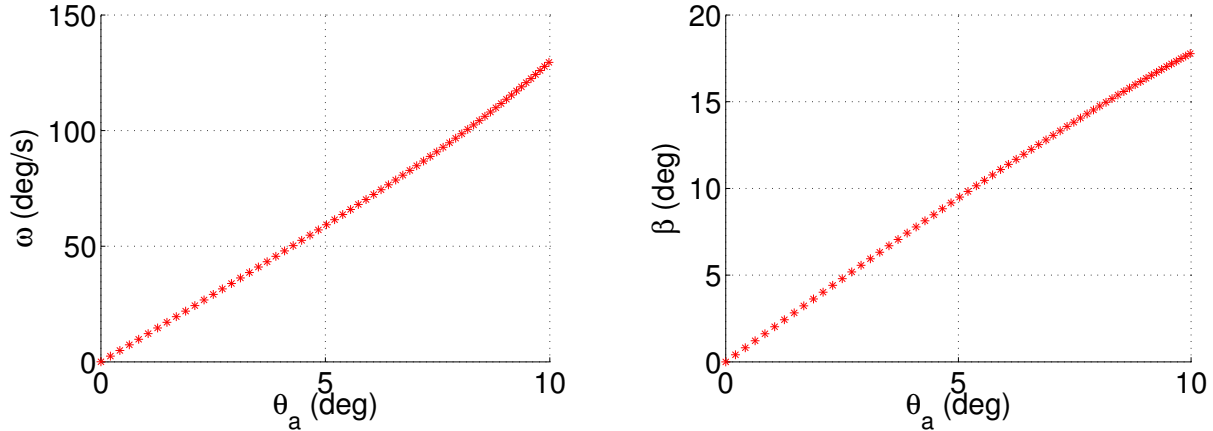


Figure 4.3: A comparison of the sideslip and turn rate as functions of anti-symmetric wing twist for otherwise identical airframes equipped with rigid and flexible wings. The wings have a Young's modulus of 5 MPa. The equilibria are marked with a red asterisk to denote that the Jacobian has a single positive real eigenvalue. In both cases, the dihedral angle at both wing roots was set to 25 deg. The flight speed was set to 2.8 m/s and the elevator was fixed at -11 deg and $\delta_L = \delta_R = 29$ deg (0.5 rad).

are locked in a symmetric dihedral configuration, the resultant turn is accompanied by a sideslip which increases with increasing turn (roll) rate. This phenomenon has been captured in Fig. 4.3 where the dihedral angle at the root was set to 29 deg (0.5 rad) for both wings. The equilibrium points are marked with a red asterisk ‘*’, indicating that they are unstable with a single positive real eigenvalue. For a rigid wing, the sideslip remains less than 5 deg until the turn rate builds up

to 35 deg/s (compared with nearly 70 deg/s for flexible wings). Thereafter, the aerodynamic data used here is insufficient to provide accurate trim results. In general, though, the sideslip increases with increasing turn rate for an aircraft with a rigid wing. On the other hand, when the wings are flexible, the turn rate increases sharply with increasing wing twist and furthermore, the sideslip peaks at just over 10 deg and drops thereafter due to the increasing effective dihedral angle. With aerodynamic data that is accurate for larger values of sideslip, the value of sideslip at the peak is liable to shift from that obtained with the present model. However, the peak itself occurs due to a favourable yawing moment which comes with an increasing wing dihedral. Therefore, a peak would be expected even with improved aerodynamic data, unless adverse yawing moment from the fuselage causes the sideslip to keep increasing with the turn rate.

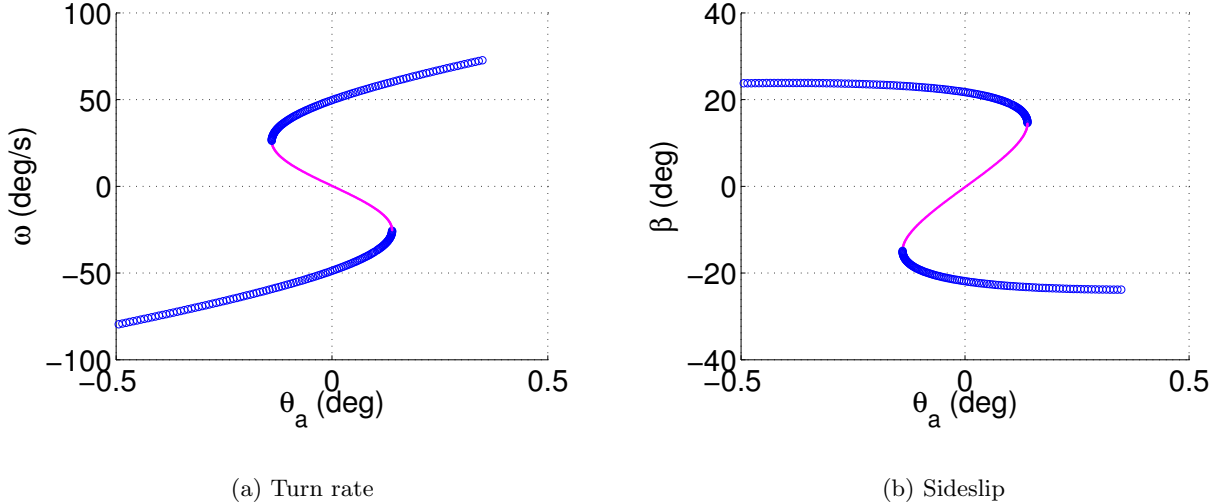


Figure 4.4: Turn rate and sideslip as functions of anti-symmetric wing twist when the $\delta_L = \delta_R = 0$. Blue circles denote equilibria where the Jacobian has a pair of complex conjugate eigenvalues with positive real parts, while pink dots denote equilibria where the Jacobian has three eigenvalues with positive real parts: one real and a complex conjugate pair. The Young's modulus was set to $E = 5$ MPa. The flight speed was set to 2.8 m/s. The elevator deflection was set to -11 deg.

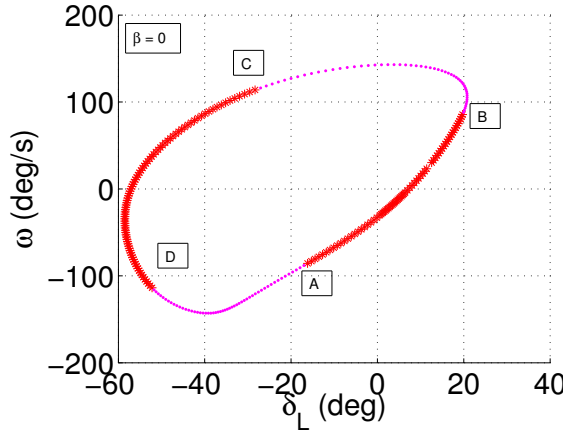
It is of interest to note that the topology of the equilibrium surface depends strongly on the wing dihedral. If the root dihedral angles are set to zero, a qualitatively different picture emerges as shown in Fig. 4.4. Blue circles ('o') denote equilibria where the Jacobian has a pair of complex conjugate eigenvalues with positive real parts, while pink dots ('.') denote equilibria where the Jacobian has three eigenvalues with positive real parts: one real and a complex conjugate pair.

The turn rate builds up rapidly and in a direction opposite to that observed in Fig. 4.3. Thereafter, the equilibrium curve turns around on itself at a saddle node bifurcation (the point of intersection of segments marked by dots and circles). The turn rate continues to increase while the sideslip value changes relatively slowly thereafter. Physically, this suggests that an uncontrolled aircraft will enter an oscillatory spin-like motion when the root dihedral is set to zero. Moreover, even if the equilibria are stabilized using a controller, the sign of the initial turn rate would be opposite to that observed for larger values of the root dihedral. This open-loop behavior needs to be understood thoroughly before a turning controller is designed.

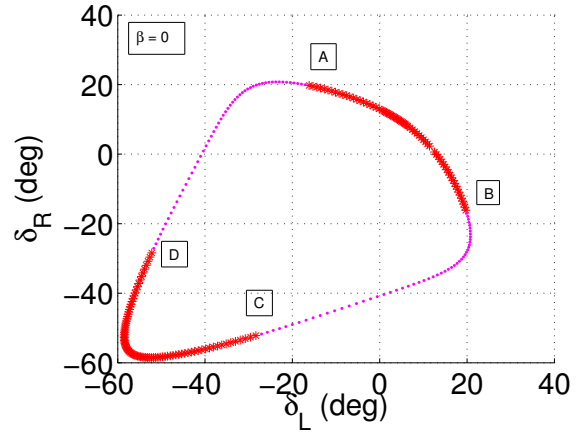
4.4.2 Coordinated Turn ($\theta_L = \theta_R = 0$; δ_L , δ_R variable)

Figure 4.5 compares the turning performance an aircraft equipped with rigid wings with that of one equipped with flexible wings with Young's modulus $E = 5$ MPa when the sideslip is required to be regulated to $\beta = 0$. The twist angle at each wing root is set to zero, i.e., $\theta_R = \theta_L = 0$. It is clear that there is no appreciable increase in the maximum achievable turn rate. However, a noticeably smaller dihedral deflection is required at the wing root for a given turn rate when the wings are flexible, as expected. The stability characteristics seen for the two sets of aircraft are identical. The points marked A, B, C and D are all Hopf bifurcations. Evidently, none of the computed equilibria possess inherent stability.

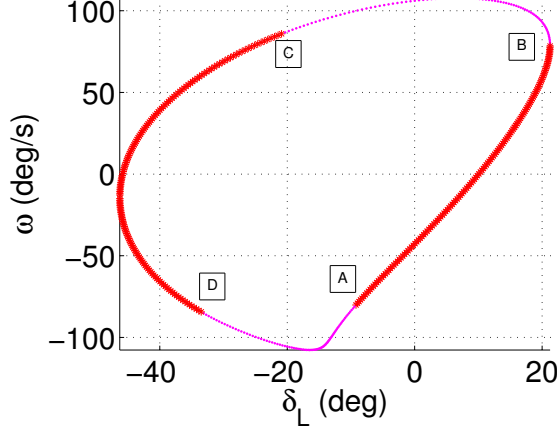
Remark: It was seen in Sec. 4.4.1 that the turn rate improved for a flexible wing MAV, accompanied by a reduced sideslip. On the other hand, in the present section, there is a deterioration in the coordinated turn performance, measured by the maximum turn rate, when the wings are flexible. This can be explained as follows. At the angle of attack considered here, the wing twists upward (i.e., the leading edge goes up) so that the net angle of attack on the wing is higher than in the rigid case. Therefore, for a given tail setting, the aircraft flies at a lower flight speed to maintain trim in pitch. The reduced speed leads to a reduction in the net lift, which, in turn, reduces the amount of centripetal force available to sustain rapid turns. Another point worth noting is that the maximum achievable turn rate depends on the maximum achievable yawing moment. The yawing moment for a given wing incidence setting reaches a maximum when the wing dihedral angle is 45 deg, or when the effective dihedral of a flexible wing equals 45 deg. This sets another



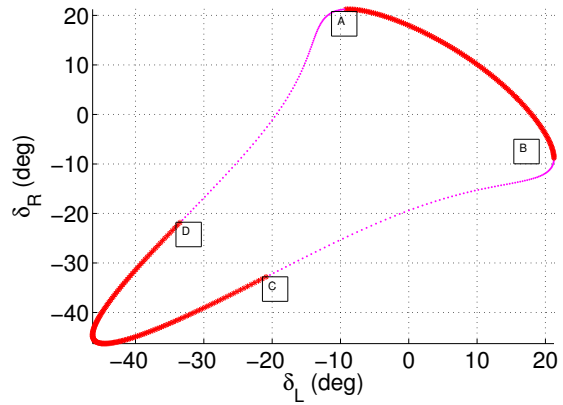
(a) Turn rate for the rigid wing aircraft



(b) Right wing dihedral angle for the rigid wing aircraft



(c) Turn rate for the flexible wing aircraft



(d) Right wing dihedral angle for the flexible wing aircraft

Figure 4.5: A comparison of the turn rate as a function of the left wing dihedral angle, and the right wing dihedral angle required to maintain zero sideslip, for otherwise identical airframes equipped with rigid and flexible wings. In both cases, the elevator deflection was fixed at -11 deg, and $\theta_R = \theta_L = 0$. The flexible wings have a Young's modulus of 5 MPa. The Jacobian of equilibria marked by pink dots have three eigenvalues with positive real parts: one real and a complex conjugate pair. The flight speed and angle of attack are within the range of validity of the aerodynamic data.

fundamental limitation on the maximum achievable turn rate, and one that arises out of the sole use the wing dihedral for turning.

4.4.3 Discussion

The results presented above yield some interesting design pointers. The wing flexibility can be reduced significantly (up to $\mathcal{O}(10)$ MPa for the wing geometry and flight speeds considered here) without achieving a substantial improvement in the coordinated turn rate or any measurable change in the effective dihedral angle, although a considerable saving in the wing mass can be achieved in the process. The motion stability (notwithstanding the structural stability of the wing) will not be markedly different from that of a rigid configuration. One interpretation which follows is that flexibility offers only a limited improvement in the performance, notwithstanding savings on the wing mass. Alternately, a complete aeroelastic analysis can be bypassed as long as the flutter and divergence speeds are “considerably larger” than the prescribed flight speeds (see Sec.4.3).

These conclusions are, by no means, universally valid but, when used judiciously, can achieve considerable savings in the computational effort invested in the design. In a recent paper, Baghdadi, Lowenberg, and Isikveren [3] observed that the open loop stability characteristics did not change markedly between the rigid and flexible configurations considered in their paper. This is in keeping with the observations in this thesis. Nevertheless, a control law designed using a rigid model yielded markedly different closed loop stability characteristics when the time constants of the rigid and flexible modes were close to each other. On similar lines, Merrett and Hilton [52] demonstrated that flutter (motion instabilities) can arise in high-speed aircraft due to transient maneuvers such as accelerations or rapid, instantaneous turns.

4.5 Chapter Summary

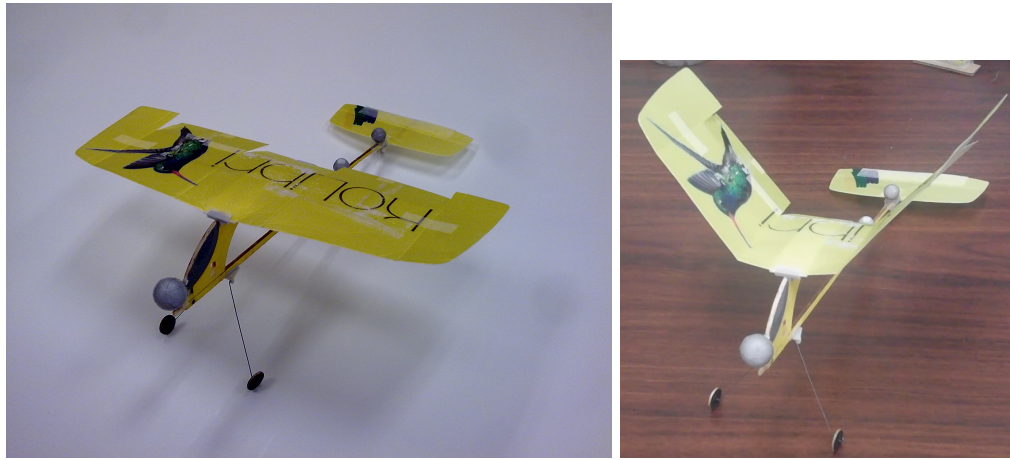
In this chapter, we generalized some of the ideas from chapter 3 to flexible winged aircraft. We introduced the concept of effective dihedral as a basis for extending the results obtained for a rigid aircraft to a flexible aircraft. We showed that flexibility does bring about an improvement in the turning performance of the MAV when wing twist is employed actively, but not when the wing dihedral angles alone are actuated. The next step would be to design a control law for managing the deformation of a flexible wing, which has been addressed in chapter 6.

Chapter 5

Experiments, Control Design and Perching

This chapter presents two sets of experiments. The first set of experiments were performed without a controller; i.e., in the open loop. In particular, the purpose of this set of experiments was to demonstrate the effectiveness of asymmetric dihedral for yaw control. The second set of experiments were performed on a remotely controlled larger aircraft. The purpose of this set was (a) to design control laws for an articulated wing aircraft, and (b) to implement them with a view of understanding their effectiveness as well as limitations. This chapter also discusses the perching maneuver, which is one of the most important maneuvers a flapping-wing aircraft would be expected to execute in the gliding phase.

5.1 Experimental Setup



(a) The aircraft with wing dihedral set to zero.

(b) The aircraft with its wings raised to a dihedral of 55 deg.

Figure 5.1: The Plantraco Kolibri Pocket Plane, used for open loop experiments described in this chapter.

Table 5.1: Physical Properties of the MAV

Property	Metric Measurement	Units
Mass	44.0	g
Wing span	41.8	cm
Wing chord (at root)	9.5	cm
Wing incidence angle	6.0	deg
Wing dihedral	controlled-variable	
MAV length	35.0	cm
Elevator area	39.12	cm ²
Propeller Thrust	39	g

The first round of experiments (open loop) was performed on Plantraco's Kolibri Pocket Plane (see figures 5.1(a) and 5.1(b)). The aircraft has a wing span of 220 mm, and weighs approximately 5 g. The wing camber is negligible, which means that $C_{m_{ac}} \approx 0$. Therefore, increasing the dihedral on the left wing relative to the right wing creates a positive yawing moment and vice-versa ($\zeta > 0$ in (3.2))

The aircraft wings were modified so that their dihedral could be changed *a priori*. Ailerons were added as substitutes for wing incidence, and the vertical tail was duly removed. The aircraft was seen to possess a significantly large L/D ratio. Ballast mass was added to the aircraft to rein in its tendency to accelerate and pull up. Spoilers were added on the inboard section of the wing to improve phugoid damping.

The closed loop experiments described here were performed on a test MAV, shown in Figure 5.2, which is a modified version of the commercially manufactured ParkZone Ember 2. The geometric properties of the MAV are listed in Table 5.1. Both wings were free to rotate from a maximum 45 deg dihedral to minimum -15 deg anhedral for a total arc range of 60 deg. The actuators for wing dihedral, it may be recalled, are controlled independently on both wings for yaw stability and control.

The VICON motion-capture system, consisting of 16 infrared cameras, was used to collect flight data, in particular the aircraft position and spatial orientation, at 100 Hz. The VICON system uses triangulation to locate the markers with an accuracy of 1 mm. The real-time datastream provided by the VICON motion-capture system includes the global reference position and the Euler angles of each object. The availability of tracking data is contingent upon the visibility of the objects. For time-steps with information loss, which were minimal and rarely comprised consecutive frames, a



(a) Symmetric dihedral 40 degrees

(b) Asymmetric configuration

Figure 5.2: Representative configurations showing the asymmetric dihedral capability of the wings. The foam table on which the aircraft is resting is not part of the airframe.

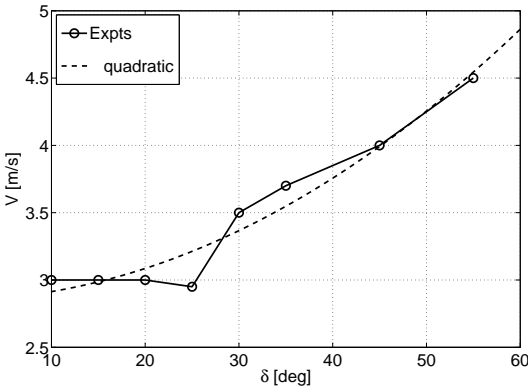
linear fit was used to estimate the missing data. Experiments were performed within the effective volume of capture, containing an area of 6 m. \times 4 m. and a height of 2 m. Since VICON provides only position and attitude information, a second order Lagrangian polynomial was used to compute velocities and angular rates, which were then filtered to eliminate noise.

One of the limitations in the MAV is the time lag in the actuator response. For example, the actual response of the wing dihedral angle and the elevator lags the commanded values by approximately 0.2 s. Furthermore, the digital filters implemented to compensate for the time delay amplify noise in the output and are designed with a low order Padé approximation. Finally, due to torque limitations of the servos and their limited ability to handle high wing-loading, the dihedral angles are typically 10 – 15 deg higher than the commanded values.

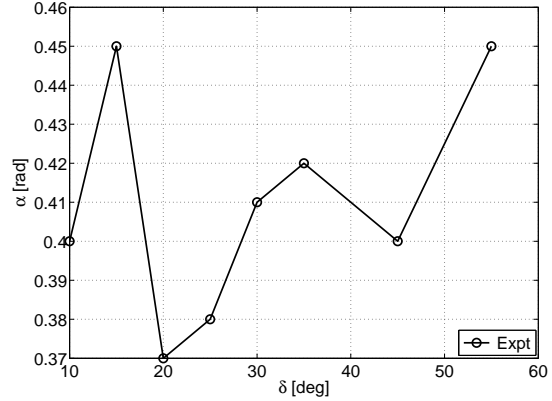
5.2 Open Loop Experimental Results

5.2.1 Symmetric Configuration

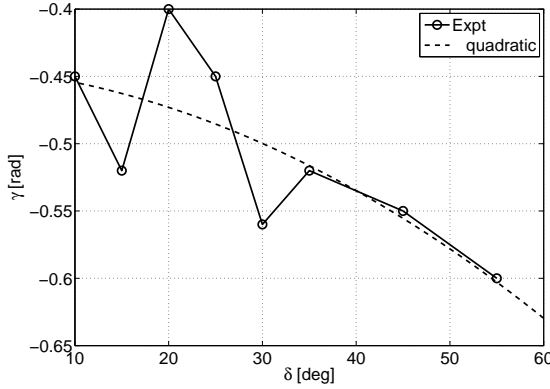
The purpose of the experiments with a symmetric configuration was to verify, qualitatively, the results in figure 3.4. Figures 5.3(a) - 5.3(c) show the flight speed, angle of attack and flight path angle as a function of the wing dihedral. Flight tests at small values of the dihedral were precarious, because of the tendency of the aircraft to depart into a spiral. Nevertheless, the velocity and the flight path angle trends (also shown by a quadratic fit) match those predicted by the theoretical analysis in the preceding section. The angle of attack increases almost linearly as the dihedral angle



(a) Flight speed as a function of the dihedral.



(b) Angle of attack as a function of the dihedral.



(c) Flight path angle as a function of the wing dihedral.

Figure 5.3: Steady state values of the longitudinal flight parameters as functions of the wing dihedral.

is increased from 20 deg to 55 deg. The angle of attack behaviour is seen to deviate substantially from the linear trend for $\alpha < 20$ deg due to the truant dynamics of the aircraft. Consequently, no attempt was made to fit a low order polynomial curve to the angle of attack data.

5.2.2 Lateral-Directional Motion

The turning performance of the aircraft was calculated for different values of the aileron deflection. The aircraft, however, was seen to be unstable, similar to that in the experiments with a symmetric

configuration. In fact, an oscillatory spin-like motion was observed during a few experiments. The results of the experiments have been tabulated in Table 5.2. The aileron deflection has been denoted by δ_a . The aircraft was seen to possess a very poorly damped transient performance. Consequently,

Table 5.2: A summary of the turning performance. The aileron deflection has been denoted by δ_a . The negative sign implies that the aircraft rolls to the left.

δ_a (deg)	δ_R (deg)	δ_L (deg)	V (m/s)	ω (deg/s)	β (deg)
−5	5	−5	3.6	104.6	4.6
	10	−5	3.74	133.5	8.02
	10	−10	3.8	154.7	13.2
−10	10	−10	3.5	160.4	−4.6
	15	−10	3.5	160.4	11.46

the values in Table 5.2 are approximate, in that they are obtained as the expected steady state solutions. Beyond $\delta_a = -15$ deg, the aircraft became unstable ruling out any meaningful turning experiments in the open loop. The data presented in Table 5.2 is, nevertheless, instructive in its own right.

For $\delta_a = -5$ deg, note that the aircraft sideslip increases as $\delta_R - \delta_L$ is increased. The desired coordinated turn would hence occur when δ_L is just less than 5 deg. The flight speed is almost constant, which matches the expectations from the earlier trim analysis. The aircraft turn rate increases as $\delta_R - \delta_L$ increases due of the consequent increase in the side force.

For $\delta_a = -10$ rad, the sideslip is zero when $\delta_L = -10$ deg, and δ_R is between 10 and 15 deg. Note that the turn rate and flight speed are almost constant. Therefore, a part of the increased sideforce is lost in compensating for the sideslip. It is interesting that even such sparse and crude, albeit carefully chosen, data can be useful for predicting the optimal dihedral combination for coordinated turns.

5.3 Control Law Design

Control law design for the MAV is described in this section. The control law has a two-tier hierarchical structure based on time-scale separation [105] which occurs naturally between the fast rotational dynamics and the slow translational dynamics:

- The innermost loop commands the elevator and the asymmetric components of the wing

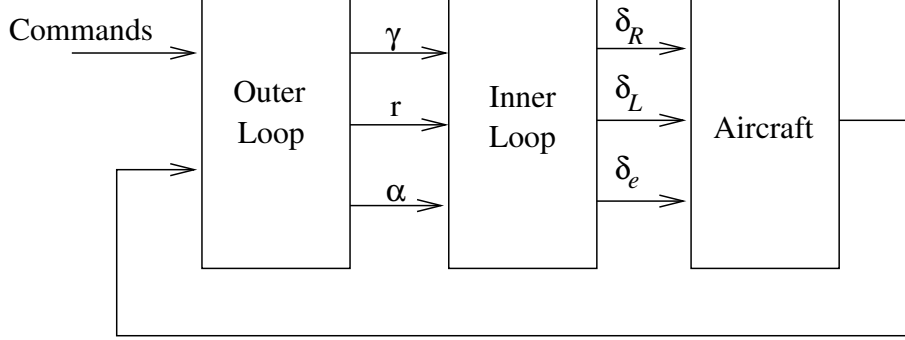


Figure 5.4: Schematic of the controller, where χ denotes the aircraft heading.

dihedral.

- The outer loop commands the angle of attack and turn rate to be tracked by the inner loop based on flight speed and turn rate. The turn rate and the flight path angle are computed based on position measurements.

A schematic of the controller is shown in Fig. 5.4.

5.3.1 Case for PI(D) Control

The control design used for experiments can be justified using the dynamic inversion (DI) approach presented by Hovakimyan, Lavretsky and Sasane [32]. We recall (a specialized version of) Theorem 2 from Ref. [32], applied to first order systems. We show that the DI-based controller can be simplified to a PI controller. By analogy, we suggest that a DI control law derived from a second order system would simplify to a PID controller. This analogy forms the basis for using PI and PID controllers for the nonlinear aircraft dynamics, and helps tune the gains on the controllers.

Consider a system described by

$$\begin{aligned}\dot{x}(t) &= f(x(t), z(t), u(t)) \\ \dot{z}(t) &= \zeta(x(t), z(t), u(t))\end{aligned}\tag{5.1}$$

where $x(0) = x_0$ and $z(0) = z_0$ for $(x, z, u) \in D_x \times D_z \times D_u$ and where $D_x, D_z, D_u \subset \mathbb{R}$ are domains containing the origin. The functions $f, \zeta : D_x \times D_z \times D_u \rightarrow \mathbb{R}$ are continuously differentiable with respect to their arguments, and furthermore, assume that $\partial f / \partial u$ is bounded away from zero in the

compact set $\Omega_{x,z,u} \subset D_x \times D_z \times D_u$ of possible initial conditions; i.e., there exists $b_0 > 0$ such that $|\partial f / \partial u| > b_0$.

Let $e(t) = x(t) - r(t)$ be the tracking error signal. Then, the open loop error dynamics are given by

$$\begin{aligned}\dot{e}(t) &= f(e(t) + r(t), z(t), u(t)) - \dot{r}(t), \quad e(0) = e_0 \\ \dot{z}(t) &= \zeta(e(t) + r(t), z(t), u(t)), \quad z(0) = z_0\end{aligned}\tag{5.2}$$

We construct an approximate dynamic inversion controller:

$$\epsilon \dot{u}(t) = -\text{sign}\left(\frac{\partial f}{\partial u}\right) \mathbf{f}(t, x, z, u),\tag{5.3}$$

where

$$\mathbf{f}(t, x, z, u) = f(e(t) + r(t), z(t), u(t)) - \dot{r}(t) - a_m e(t)\tag{5.4}$$

where $a_m > 0$ gives the desired rate of convergence.

Let $u(t) = h(t, e, z)$ be an isolated root of $\mathbf{f}(t, e, z, u) = 0$. The reduced system for the dynamics in (5.2) is given by

$$\begin{aligned}\dot{e}(t) &= -a_m e(t), \quad e(0) = e_0 \\ \dot{z}(t) &= \zeta(e(t) + r(t), z(t), h(t, e(t), z(t))), \quad z(0) = z_0\end{aligned}$$

The boundary layer system is

$$\frac{dv}{d\tau} = -\text{sign}\left(\frac{\partial f}{\partial u}\right) \mathbf{f}(t, e, z, v + h(t, e, z))\tag{5.5}$$

where the state $v(t) = u(t) - h(t, e, z)$, and the time τ is obtained by scaling t : $\tau = t/\epsilon$.

We assume that three conditions hold for all $[t, e, z, u - h(t, e, z), \epsilon] \in [0, \infty) \times D_{e,z} \times D_v \times [0, \epsilon_0]$ for some domains $D_{e,z}, D_v \subset \mathbb{R}$ which contain the origin:

1. The functions f, ζ are such that their partial derivatives with respect to (e, z, u) , and the partial derivative of f with respect to t are continuous and bounded on any compact subset

of $D_{e,z} \times D_v$. Further, $h(t, e, z)$ and $\frac{\partial f}{\partial u}(t, e, z)$ have bounded first derivatives with respect to their arguments, and $\frac{\partial f}{\partial e}$ and $\frac{\partial f}{\partial z}$ are Lipschitz in e and z uniformly in t .

2. The origin is an exponentially stable equilibrium of $\dot{z}(t) = \zeta(x, z, h(t, 0, z))$

3. The term $\left| \frac{\partial f}{\partial u} \right|$, is bounded away from zero

Theorem (Theorem 2, Hovakimyan, Lavretsky and Sasane [32]): Subject to the three assumptions above, the origin in an exponentially stable equilibrium of the boundary layer system (5.5). Moreover, let Ω_v be a compact subset of R_v , where $R_v \subset D_v$ denotes the region of attraction of the autonomous system

$$\frac{dv}{d\tau} = -\text{sign}\left(\frac{\partial f}{\partial u}\right) \mathbf{f}(0, e_0, z_0, v + h(0, e_0, z_0))$$

Then for each compact subset $\Omega_{z,e} \subset D_{z,e}$ there exist a positive constant ϵ_* and $T > 0$ such that for all $t \geq 0$, $(e_0, z_0) \in \Omega_{e,z}$, $u_0 - h(0, e_0, z_0) \in \Omega_v$, and $0 < \epsilon < \epsilon_*$, the system (5.1), (5.3) has a unique solution $x_\epsilon(t)$ on $[0, \infty)$ and $x_\epsilon(t) = r(t) + \mathcal{O}(\epsilon)$ holds uniformly for $t \in [T, \infty)$. \square

The control law in Eq. (5.3) can be reduced to a PI controller. Note that $\dot{x} = f(t, x, z, u)$. Therefore, the controller can be written as

$$\begin{aligned} \epsilon \dot{u}(t) &= -\text{sign}\left(\frac{\partial f}{\partial u}\right) \mathbf{f}(t, x, z, u) \\ &= -\text{sign}\left(\frac{\partial f}{\partial u}\right) (f(e(t) + r(t), z(t), u(t)) - \dot{r}(t) - a_m e(t)) \\ &= -\text{sign}\left(\frac{\partial f}{\partial u}\right) (\dot{e}(t) - a_m e(t)) \end{aligned} \quad (5.6)$$

Integrating both sides yields a PI controller of the form

$$u(t) = u(0) - \text{sign}\left(\frac{\partial f}{\partial u}\right) \frac{1}{\epsilon} \left(e(t) - e(0) - a_m \int_0^t e(t) dt \right) \quad (5.7)$$

Remark: If k_p and k_i denote the proportional and integral gains of the PI controller, then they should be chosen to satisfy $k_i = a_m k_p$ and $k_p = 1/\epsilon$.

Remark: We could have started with a second order system, $\ddot{x}(t) = f(t, x, \dot{x}, z, u)$. If $u(t)$ is to be

designed to ensure that $\ddot{x} = -c\dot{e}(t) - ke(t) + \ddot{r}(t)$, where c and k are chosen to guarantee desired convergence properties, then the DI approach gives rise to a PID controller with gains k_p , k_i and k_d chosen to satisfy $k_i = kk_d$, $k_p = ck_d$ and $k_d = 1/\epsilon$.

Remark: The point to be noted here is that PI and PID controllers can be used for nonlinear systems. The theorem stated above guarantees that it will perform the tracking objective with an error bound of $1/\epsilon$. To address robustness concerns, a filter can be added in line with the small gain theorem. This is done in adaptive control methodologies where, instead of substituting for $f(t, x, u)$ with \dot{x} , $f(t, x, u)$ is predicted online using adaptive algorithms [59].

5.3.2 Simulations

PID controllers designed using DI-inspired tuning were simulated. The time histories obtained in two different environments have been plotted in Figs 5.5 (no external disturbances) and 5.6 (persistent periodic disturbances). In both cases, the controllers performed satisfactorily. The angle of attack was kept above 11 deg to ensure the yaw control effectiveness of the dihedral was uniformly positive.

Remark: The purpose of the simulations was to demonstrate a general control design technique. However, in the course of experiments, we were able to make reasonable estimates of the open loop dynamics. This allowed us to tune controllers without resorting to a DI-inspired scheme.

5.3.3 Angle of Attack Control

The stability of the longitudinal dynamics depends on the CG location. Two longitudinal controllers were designed: one for the configuration with the vertical tail where the CG was placed around the quarter-chord point of the wing, and another for the configuration without a vertical tail where the CG was placed between 0.25 c and 0.3 c behind the wing AC. Here, c denotes the wing root chord length.

The longitudinal dynamics of the configuration with a vertical tail were seen during experiments to be stable across the angle of attack envelope, as a consequence of a favorable CG location, while the lateral dynamics showed a divergent unstable yaw mode. The angle of attack is controlled using

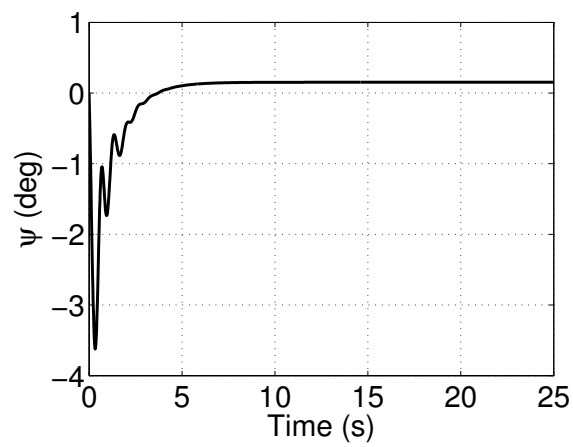
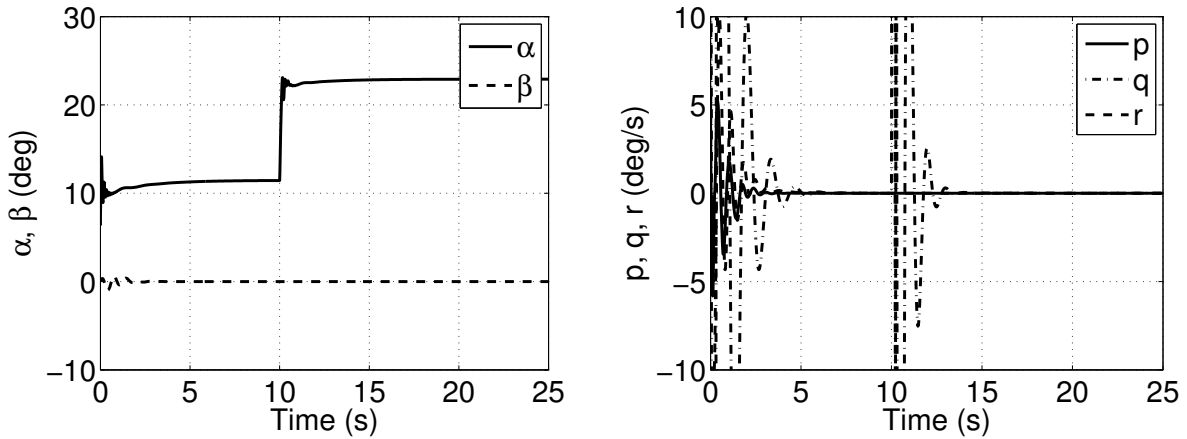


Figure 5.5: Simulated time histories of the aircraft in a disturbance-free flight. A 12 deg (0.2 rad) jump in the angle of attack, α , is commanded. The resulting disturbances are rejected by the control law.)

a simple PID scheme which ensures satisfactory tracking and retains an ease of implementation on the hardware.

Let $e_\alpha(t) = \alpha_c(t) - \alpha(t)$, where $\alpha_c(t)$ is the commanded angle of attack. A gain-scheduled PI

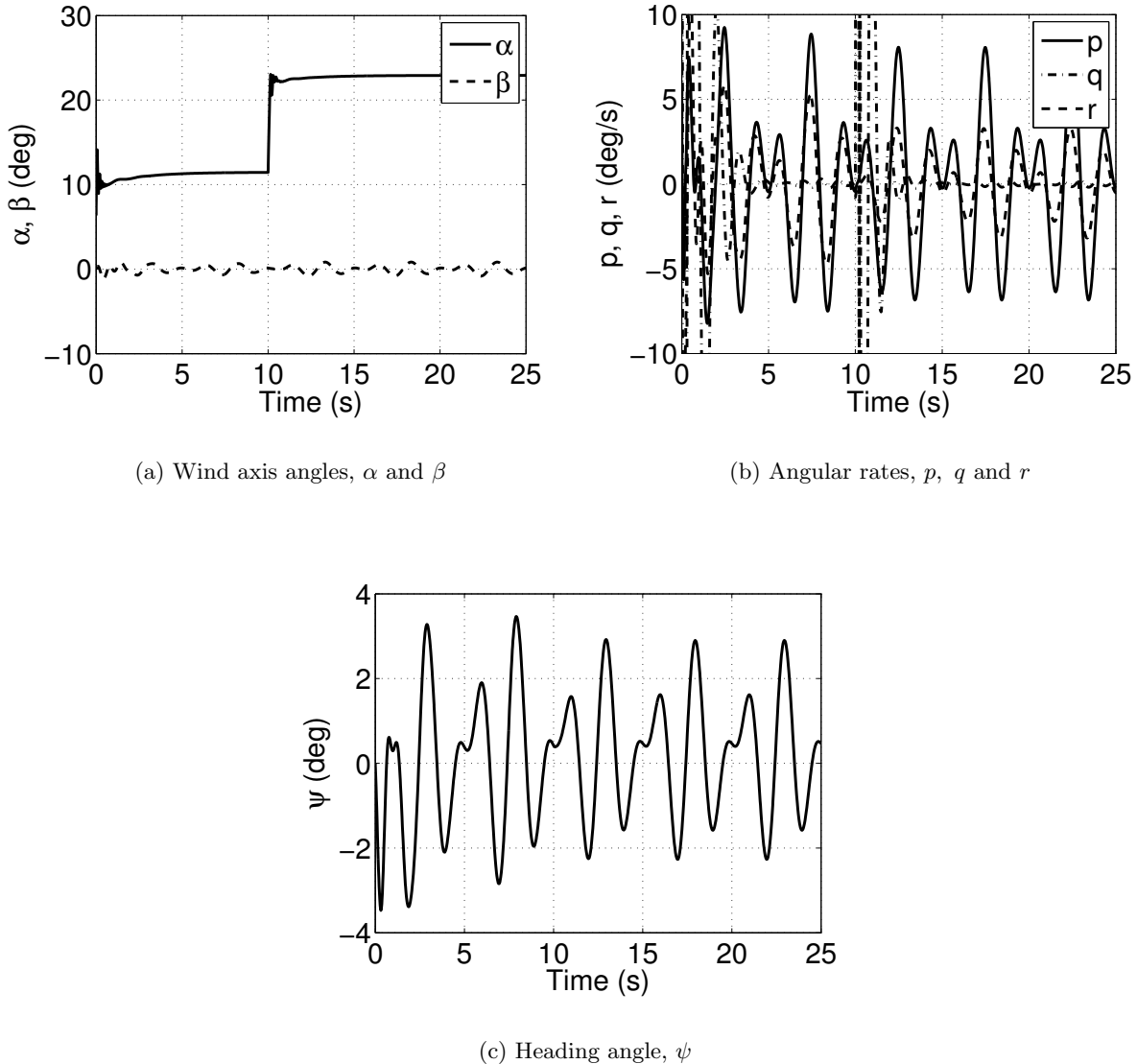


Figure 5.6: Simulated time histories of the aircraft in a persistent periodic lateral-directional disturbance field. A 12 deg (0.2 rad jump in the angle of attack, α , is commanded.)

controller commands the elevator deflection in the configuration with a vertical tail:

$$\delta_e(t) = k_p e_\alpha + k_i \int_0^t e_\alpha dt, \text{ where } k_p = k_i = -0.45 + 20(\alpha - 0.18)^2 \quad (5.8)$$

The longitudinal dynamics of the tailless Configuration are stable, but poorly damped for $\alpha > 8$ deg. Around $\alpha = 15$ deg, the elevator effectiveness saturates and higher angles of attack are unattainable under routine flight conditions. The open loop response was measured to have a time period of 1 s. The observed reduction in the amplitude of oscillations was used to approximate the damping coefficient to 0.046. The open loop dynamics can be written in the form

$$\ddot{\alpha} + 0.62\dot{\alpha} + 40\alpha = -40\delta_e + 5.6 \quad (5.9)$$

Therefore, an essentially derivative-integral controller was designed for the tailless configuration:

$$\delta_e(t) = 0.14 - \alpha_c + k_d \dot{\epsilon} + k_i \int_0^t e_\alpha dt, \quad (5.10)$$

where the offset of 0.14 rad was added based on the measured $\delta_e - \alpha$ trims. The gain k_i was similar to that for the configuration with a vertical tail, while $k_d = 0.217$ is chosen so that the damping coefficient is approximately equal to 0.7.

5.3.4 Yaw Control by Asymmetric Wing Dihedral

Yaw control has been often neglected in the literature on perching, primarily because the aircraft possessed the traditional roll and yaw control surfaces. On the other hand, lateral-directional control is an important concern for aircraft which lack a roll control surface and use a highly unconventional yaw control mechanism. Two different yaw controllers are needed for the configurations with and without a vertical tail because the wing dihedral plays a separate role in each configuration. Moreover, although both configurations are laterally unstable, the nature of the instability is different. In the configuration with a vertical tail, the role of the wing dihedral is to primarily provide the side force required to sustain a turn. The yaw moment required for trimming comes from the wing dihedral as well as the vertical tail. Furthermore, since the vertical tail is

not actuated, the dihedral angles need to be controlled for different maneuvers such as entering or recovering from a turn.

The asymmetric component of the wing dihedral angles, δ_{asym} , is commanded by a PI controller. Let $e_r(t) = r_c(t) - r(t)$, where $r_c(t)$ is the commanded yaw rate. The anti-symmetric dihedral deflection commanded by the controller is given by

$$\delta_{\text{asym}}(t) = 1 e_r(t) + 0.5 \int_0^t e_r(t) dt \quad (5.11)$$

Unlike the configuration with a vertical tail, the tailless aircraft is seen to be highly unstable in the open loop. The lateral-directional dynamics are primarily underdamped, which mandates the use of a derivative controller (unlike the PI which sufficed for the configuration with a vertical tail).

Based on experimental observations, it was estimated that the open loop yaw-rate dynamics are of the form

$$\ddot{r} + 2\zeta\omega\dot{r} + \omega^2 r = N_{\delta_{\text{asym}}} \delta_{\text{asym}}, \quad \zeta \approx -0.1, \quad \omega \approx 2\pi \quad (5.12)$$

for $\alpha < 8$ deg. Thereafter, the yaw dynamics are unstable and oscillatory in nature. Recall the approximation for $N_{\delta_{\text{asym}}}$:

$$N_{\delta_{\text{asym}}} \approx \frac{1}{2I_z} \rho V_\infty^2 S_{out} c \left(\frac{C_{L\alpha}\alpha}{3} + C_{m,ac} \right)$$

where S_{out} is the combined area of the outboard sections of the two wings and I_z is the aircraft moment of inertia about the z axis. Substituting the estimates for the geometric and aerodynamic terms, it follows that

$$-2 < N_{\delta_{\text{asym}}} < -1.2, \quad \alpha < 6 \text{ deg} \quad (5.13)$$

Finally, in order to account for the actuator time delay of 0.2 s, a lead compensator $L(s)$ is designed given by $L(s) = \frac{8(s+4.5)}{4.5(s+8)}$. Furthermore, a derivative filter of the form $D(s) = \frac{12(s+4)}{s+8}$ is designed. The role of dihedral control is regulation, and it suffices use a derivative controller for

damping addition, so that the commanded dihedral deflection is given by

$$\delta_{\text{asym}} = k_d D(s) L(s) e_r(s) \quad (5.14)$$

5.3.5 Perching Guidance Loop

The outer control loop is designed to ensure rapid changes in the flight path over a short duration. For the sake of completeness, it must be noted here that, in general, the guidance loop commands the flight path angle as well as the turn rate. The flight path angle (γ), the heading angle (χ), and the turn rate (ω) are given by [65]

$$\sin \gamma = \cos \alpha \cos \beta \sin \theta - \sin \beta \sin \phi \cos \theta - \sin \alpha \cos \beta \cos \phi \cos \theta \quad (5.15)$$

$$\begin{aligned} \sin \chi \cos \gamma &= \cos \alpha \cos \beta \cos \theta \sin \psi + \sin \beta (\sin \phi \sin \theta \sin \psi + \cos \phi \cos \psi) \\ &+ \sin \alpha \cos \beta (\cos \phi \sin \theta \sin \psi \sin \phi \cos \psi) \end{aligned} \quad (5.16)$$

$$\omega = \dot{\chi} = \text{sign}(\dot{\chi}) \sqrt{p^2 + q^2 + r^2} \quad (5.17)$$

The flight path angle is controlled in discrete time so that a symmetric dihedral angle is commanded every 0.2 s (which is equal to the dihedral actuator time delay). The commanded dihedral angles are given by

$$\delta_R = \delta_L = \sqrt{2 + \frac{2}{f(\alpha) \tan \gamma_c}}, \quad f(\alpha) \approx \frac{C_L(\alpha)}{C_D(\alpha)} \quad (5.18)$$

where γ_c is the commanded flight path angle which is, in turn, given by

$$\gamma_c = \tan^{-1}(h) \approx \frac{h}{1 + 0.28125h^2}, \quad h = \frac{z - z_l}{\sqrt{(x - x_l)^2 + (y - y_l)^2}} \quad (5.19)$$

Here, x_l , y_l and z_l are the coordinates of the desired landing point on the ground, or a point in the air where a perching command is to be sent to the aircraft. It has to be noted that the dihedral and flight path angles are computed and commanded every 0.2 s. This is not an optimal gliding strategy because it does not take into account the instantaneous flight path angle and aircraft speed. It was seen to be effective over the short duration of the experiments, although it needs to be improved for experiments which may last over a longer duration. It is interesting to note

that changing the wing dihedral brings about a significant effect in the pitching moment and using a continuous-time flight path controller leads to undesirable oscillatory behavior due to coupling with the pitch dynamics. This problem is bypassed by updating the dihedral angle every 0.2 s, an interval which was arrived at after trial and error in the course of experiments.

5.4 Closed Loop Experiments

5.4.1 Angle of Attack Control for Perching

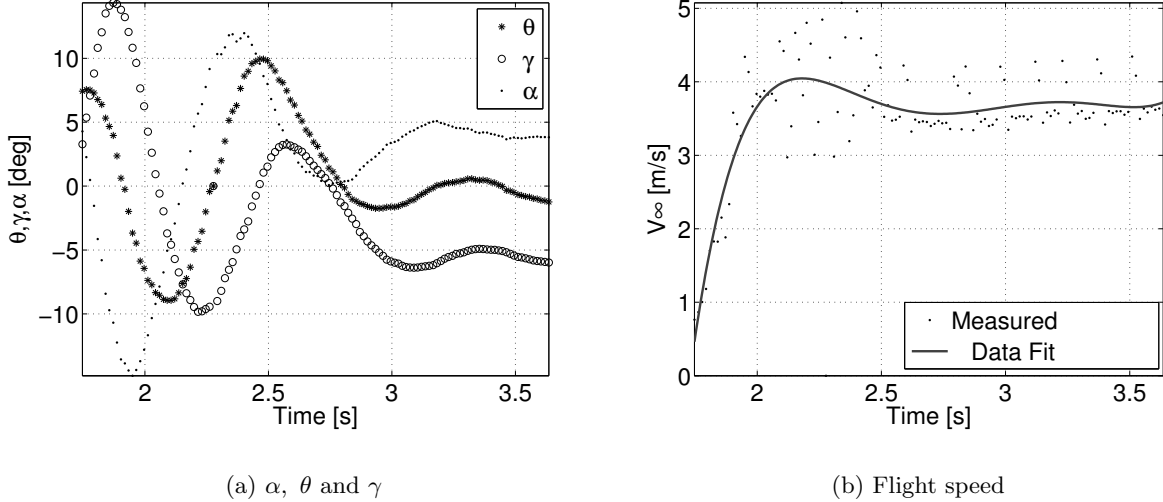


Figure 5.7: Experimental results showing the longitudinal flight parameters. In particular, α settles down at the desired value within 2 s.

Figure 5.7 shows the experimentally-measured longitudinal flight parameters. For these experiments, the wing dihedral was not controlled actively which caused the aircraft heading to deviate steadily from a straight line. An angle of attack of 5 deg was commanded while the flight speed and flight path angle were not controlled. The controller for the tailless aircraft yielded similar characteristics as the one with a vertical tail.

5.4.2 Lateral-Directional Control for Perching

In the aircraft with a vertical tail, local lateral stability was achieved using a simple PID controller. However, in several flight tests, the roll rate was seen to build up due to the dihedral effect and,

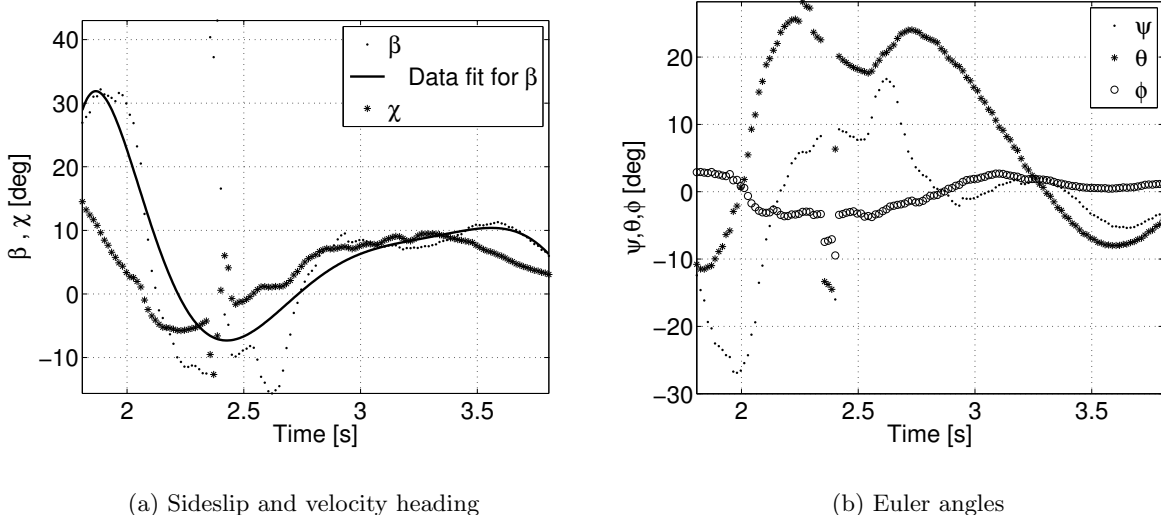


Figure 5.8: Experimental results showing the sideslip, velocity heading and the Euler angles measured during a yaw control test of the aircraft with a vertical tail. Parameters appear to be regulating during the short experiment

without wing twist or ailerons, could not be compensated. This led to a divergent lateral-directional behavior despite local stability. Figure 5.8 shows the time histories for the case where the lateral dynamics were seen to be stable. A zero heading angle was commanded. The heading angle as well as sideslip converge to small values. However, the transient response does not vanish within the limited flight duration. Nevertheless, the yaw rate slows significantly by the end of the flight indicating good closed loop stability characteristics. Lateral control of a tailless configuration is under experimental investigation.

5.4.3 Flight Path Control for Perching

An effective flight path controller is necessary for a successful perching maneuver. The aircraft must be able to track the desired flight path in order to arrive at a spatial target with an acceptable flight speed and height. The PID controller gains on the angle of attack controller were tuned to ensure sound tracking characteristics across a range of flight path angles. The flight path angle itself, as explained in section 5.3.5, is controlled using the wing dihedral angles.

5.5 Perching

5.5.1 C_L for Perching

Figure 5.9 shows some snapshots of an owl executing a perching maneuver. These were extracted from a reputed BBC documentary called the Life of Birds, and the clip was processed in Matlab. The longitudinal flight parameters, the flight path angle γ , the body axis pitch angle θ , and the angle of attack α , were extracted by making two assumptions: (a) the depth calibration was assumed to be unchanged, and (b) the local ground level was assumed to be approximately horizontal. These flight parameters have been plotted in Fig. 5.10. The perching maneuver is seen to consist of two phases: a gliding phase to bring the aircraft to a suitable position with respect to the landing spot, followed by a rapid pitch up (usually to a post-stall angle of attack) which leads to an instantaneous climb and a rapid deceleration.

Interestingly enough, when Cory and Tedrake [16] optimized the perching maneuver using the error in the final position as the cost, the resulting maneuver had a similar two-step profile; in particular, the elevator switched between two values, one corresponding to a low- α flight and the other being the saturation value of the elevator deflection which produced the desired post-stall angle of attack.

A perching maneuver requires three key ingredients: (a) a guidance law which brings the aircraft to a desired point, (b) a yaw controller which regulates the heading, and (c) identification of a suitable point to commence the pitch-up. Task (a) is a formidable problem in its own right and has not been addressed here because our objective has been to understand the capabilities of the aircraft and the flight mechanics underlying the maneuvers. Task (b) was addressed in the previous section. Task (b) has been largely ignored in the literature because perching has been studied using a stable aircraft. However, tailless aircraft are unstable and the instability is rapid enough to be of relevance even in a rapid maneuver like perching. We have addressed the problem of yaw control in section 5.3.4.

In this section, we identify a suitable point with reference to the landing point at which the pull up maneuver is executed. Our identification is purely at the level of flight mechanics. The reader is referred to Refs. [16, 107, 108] for optimal guidance laws. We assume that C_L is essentially



Figure 5.9: Snapshots showing an owl in various stages of a perching maneuver, from BBC's Life of Birds. The video was processed using Matlab.

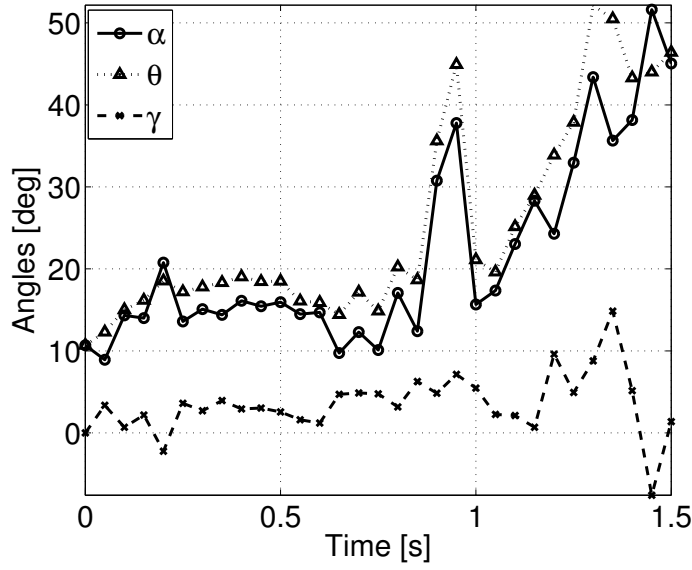


Figure 5.10: Angle of attack, flight path angle and pitch angle measurements from the BBC video of a perching owl. The maneuver was completed at $t = 1.5$ s.

constant during the second (constant δ_e) phase of perching. This leaves us with three variables to contend with: the initial flight speed, the initial flight path angle, and the distance from the landing point at which the maneuver is commenced. We seek to calculate the final speed and the C_L required for the maneuver. Note that the value of C_L required for the maneuver depends on the initial distance from the landing point.

We start with the longitudinal equations of motion of the aircraft. Let $s_c = \rho S/(2m)$ and let $\cos \gamma \approx 1$. Then, the equations of motion are given by

$$\begin{aligned}\dot{V} &= -g \sin \gamma - s_c V^2 C_D \\ \dot{\gamma} &= s_c V C_L - \frac{g}{V} \\ \dot{z} &= -V \sin \gamma\end{aligned}\tag{5.20}$$

We wish to use the x coordinate as the independent variable instead of t . Let $V' = dV/dx$, and

note that $\dot{x} = V \cos \gamma$. We make a small angle approximation, i.e., $\sin \gamma \approx \gamma$. Therefore, we get

$$\begin{aligned} V' &= -\frac{g}{V}\gamma - s_c V C_D \\ \gamma' &= s_c C_L - \frac{g}{V^2}, \quad z' = -\gamma \end{aligned} \quad (5.21)$$

The equation for V' can be solved analytically. Multiplying both sides by V gives

$$\begin{aligned} VV' &= -g\gamma - s_c V^2 C_D \\ \implies \frac{V^2}{2} &= e^{-2s_c C_D x} \frac{V_0^2}{2} - g \int_0^x e^{-2s_c C_D (x-\tilde{x})} \gamma d\tilde{x} \\ \implies \frac{V^2}{2} &\approx e^{-2s_c C_D x} \frac{V_0^2}{2} - g(z - z_0) \end{aligned}$$

The final velocity, V_f , at $z = z_0$ and $x = x_f$ is given by

$$V_f = e^{-s_c C_D x_f} V_0 \quad (5.22)$$

It now remains to find an expression for C_L , which would yield C_D to compute V_f .

Consider the last two equations in Eq. (5.21). It follows that

$$z'' = \frac{g}{V^2} - s_c C_L \quad (5.23)$$

We wish to command a constant value for C_L . To get an estimate, we could assume that V is a constant. This is not very accurate, especially because perching usually involves a considerable deceleration. However, since the purpose is to obtain a simple yet reliable estimate, we could use $V_c = 0.5(V_f + V_0)$. In any case, the right hand side of (5.23) is a constant, and it follows that

$$z_f = 0 = \left(\frac{g}{V_c^2} - s_c C_L \right) \frac{x_f^2}{2} - \gamma_0 x_f \quad (5.24)$$

Thus, it follows that C_L has to be chosen to satisfy

$$C_L = \frac{g}{s_c V_c^2} - \frac{2\gamma_0}{s_c x_f} \quad (5.25)$$

The right hand side depends on V_c , which is obtained from Eq. (5.22) which depends, in turn, on C_L . Therefore, an iterative procedure is required to compute C_L . Equation (5.22) also sets a bound on the smallest attainable V_f without stalling: $V_{f,\min} = e^{-s_c C_{D,s} x_f} V_0$, where $C_{D,s} = C_{D_0} + k C_{L,\max}^2$.

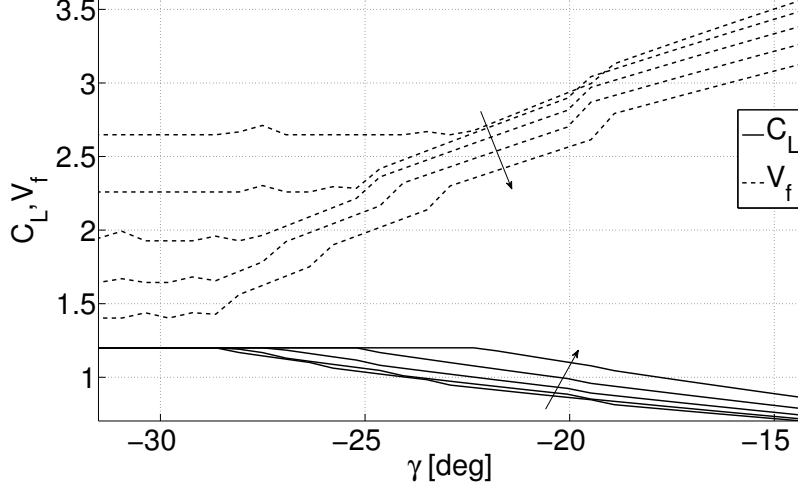
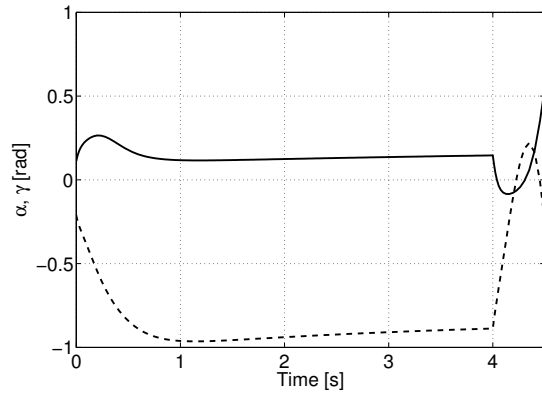


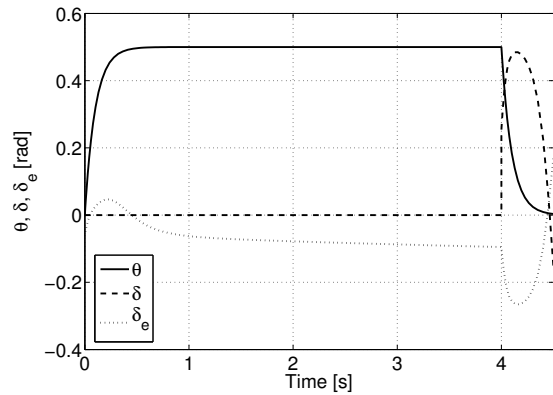
Figure 5.11: The C_L required for perching, starting with $V_0 = 5$ m/s for different values of γ_0 and x_f . The value of C_L has been calculated using Eq. (5.25). The arrow indicates the direction of increasing x_f .

Figure 5.11 shows the C_L required as a function of γ_0 for different x_f . The value of C_L is seen to saturate for steeper flight path angles. At the same time, the final flight speed decreases with steeper initial flight path angle and a larger x_f . This observation can be explained by the fact that, in both cases, a larger distance is available for deceleration. Note, however, that once the saturation point is reached, a steeper glide renders the desired landing point unattainable. Wing twist can be used to execute a perching maneuver when the option of dropping below the perching point is not available [11].

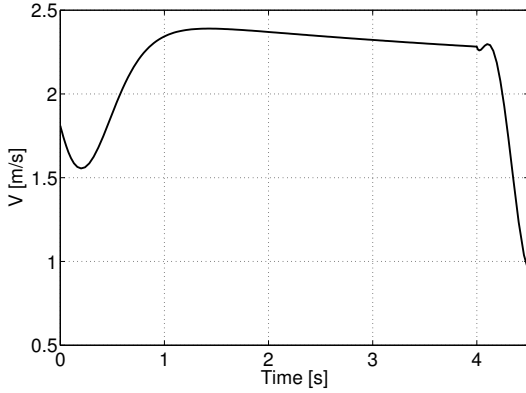
This figure illustrates the importance of perching in the post-stall flight regime, which is marked by high values of both C_L as well as C_D which, in turn, help ensure a reduced V_f . The problem of flying in the post-stall regime, though, is the possibility of loss of elevator effectiveness. This can be mitigated by using wing twist which allows the wing angle of attack to be increased to post-stall values without compromising the effectiveness of the horizontal tail. Figure 5.12 shows a perching maneuver executed on a high-drag aircraft configuration [62]. The wing twist was scheduled to hold the angle of attack of the wing constant, and the elevator was used to maintain the angle of attack



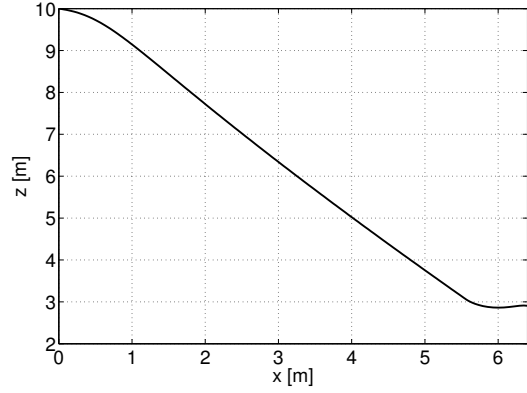
(a) Angle of attack (solid line) and flight path angle (dashed line)



(b) Elevator deflection, wing twist and dihedral angles



(c) Speed



(d) Trajectory

Figure 5.12: Perching trajectory, and time histories of state and control variables for a high drag configuration [62].

of the aircraft. The availability of wing twist, together with high drag, allow for a considerably large deceleration in a very short period of time following a steep, rapid glide.

Figure 5.11 also illustrates the importance of wing articulation. Recall our observation in Chapter 3 that the ability to change the wing dihedral symmetrically can be used to fly steep glides without a steep increase in the flight speed. This ability would translate to a reduction in the terminal speed at the end of a perching maneuver. Note, however, that the amount of space available below the perching point constrains γ_0 , the flight path angle at the end of the descent phase. A perching maneuver which starts with a steep drop is used by birds to perch on cliffside

nests, and can be used by robotic aircraft for perching on power lines or ledges.

5.5.2 Experimental Demonstration of a Perching Maneuver

In conjunction with the guidance controller, a perching maneuver is executed as follows. An appropriate altitude is chosen such that a perching command is sent when the aircraft crosses it. This value was chosen to accommodate the actuation time delays for the wing dihedral as well as the elevator. Until this point, the angle of attack and flight path angle controllers described in Sec. 5.3 were used actively. Once the aircraft reaches the prescribed altitude, zero dihedral and maximum pitch-up elevator angles are commanded. These signals are held until touch-down. Figure 5.13 shows the perching signal sent at the 0.6 s mark. The angle of attack builds up to 30 deg, causing the speed to reduce, and the aircraft climbs momentarily. Flight speed is halved within 1 s to 3 m/s. After a brief ascent, the MAV lands at a low angle of attack. It is interesting to note that the final speed has reduced substantially even without using wing twist. Addition of wing twist would not only enable a further reduction in the final speed, but also provide for better roll and yaw control during the approach.

Experiments are currently under way on an aircraft which uses ailerons for roll control as well as for ensuring that $N_{\delta_{\text{asym}}}$ does not change sign in the flight envelope. This will allow us to use the yaw controller during the course of the entire perching maneuver, particularly during the pull-up phase. The ailerons on either wing are controlled independently of each other, which means that they can be used as conventional flaps as well to reduce the terminal speed further. Eventually, a claw or a suction pad may be added to the aircraft to ensure that the aircraft performs a perched landing at the desired spot.

5.6 Use of Trailing Edge Flaps for Mitigating Control Effectiveness Problems

Recall, from the discussion in Chapter 3, Section 3.2.3, that the yaw control effectiveness of the anti-symmetric dihedral depends primarily on the angle of attack, and also on the angular rates. The sign of the effectiveness depends on the sign $(x_a C_L/c + C_{m,ac})$, where x_a/c is the non-dimensional

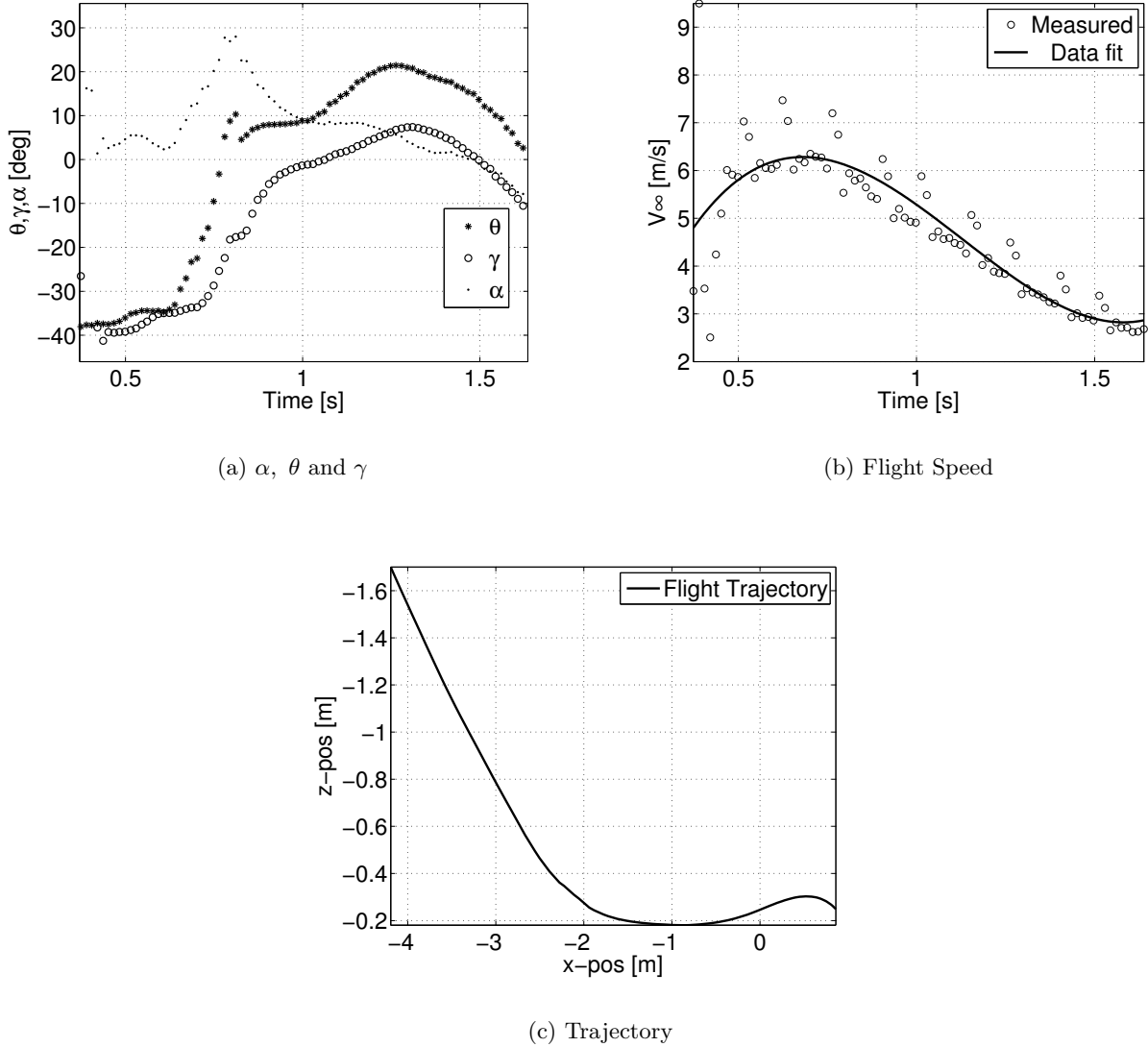


Figure 5.13: Flight parameters during a perching attempt that was triggered at 1.5m above the ground

distance between the center of gravity and the quarter-chord line. Furthermore, $C_{m,ac} < 0$, and therefore, at small angles of attack, the control effectiveness is negative and it is positive at higher angles of attack. For an intermediate range of angles of attack, the sign depends on the angular rates as well. This can cause immense problems for yaw control, particularly when the angle of attack changes between the three regions in the course of a maneuver.

One way to get around this problem is to use trailing edge (TE) flaps. TE flap deflection leads to a greater increase in C_L as compared to the reduction in $C_{m,ac}$. From thin airfoil theory [48], it

can be shown that the change in C_L and $C_{m,ac}$ due to a flap deflection δ_f is given by

$$\begin{aligned}\Delta C_L &= (2(\pi - \theta_f) + 2 \sin \theta_f) \delta_f \\ \Delta C_{m,ac} &= -\frac{\delta}{2} \sin \theta_f \cos(\theta_f - 1),\end{aligned}\quad (5.26)$$

where θ_f depends on the non-dimensionalized location of the flap (x_f):

$$x_f = 0.5(1 - \cos \theta_f) \quad (5.27)$$

For our aircraft, $x_f \approx 0.8$ and $x_a/c = 0.25$. Thus, $\theta_f = 2.2143$. Thus, $\Delta C_L = 3.45\delta_f$ and $\Delta C_{m,ac} = -0.14\delta_f$.

It is of interest to find the flap deflection, as a function of α , which will guarantee a certain positive control effectiveness. For example, suppose we need the effectiveness to be at least 0.025 (corresponds to an α of 10 deg in Fig. 5.14(a)). Then, substituting the expressions for ΔC_L and $\Delta C_{m,ac}$, it follows that

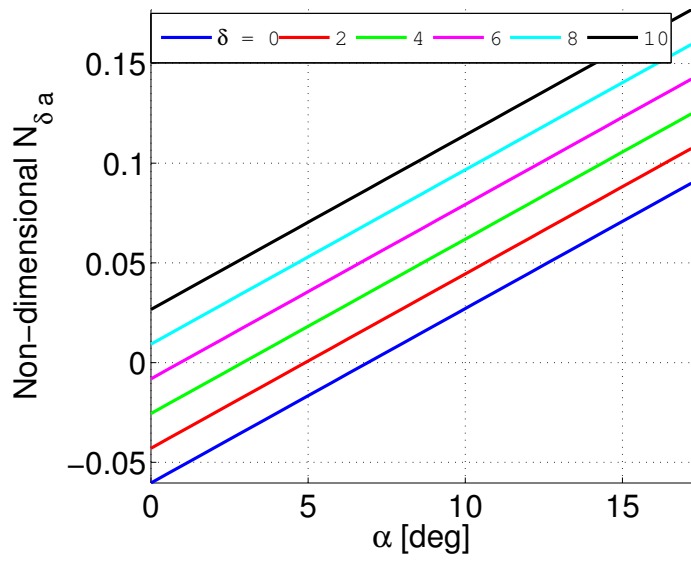
$$\begin{aligned}\frac{C_L}{4} + C_{m,ac} + 0.72\delta_f &= 0.025 \\ \therefore 0.07 + 0.5\alpha - 0.1311 + 0.72\delta_f &= 0.025 \implies \delta_f = 0.12 - 0.69\alpha\end{aligned}\quad (5.28)$$

Figure 5.14(b) plots the value of δ_f in Eq. (5.28) as a function of α .

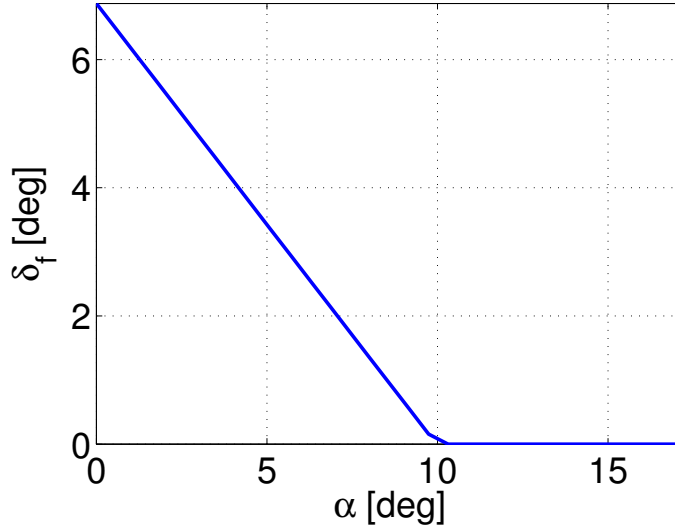
The benefit of a uniformly positive control effectiveness, however, comes at a terrible cost: the aircraft is forced to fly in a high-lift (it can be checked that $C_L > 0.64$), high drag configuration across the flight envelope. This necessarily means that the aircraft will fly slower than normal. However, note that the flight path angle can still be controlled effectively using symmetric dihedral deflection.

5.7 Chapter Summary

In this chapter, we described the results of open loop and closed loop experiments. The open loop experiments demonstrated the claims made in Chapter 3 on the basis of a conceptual and numerical study. The closed loop experiments were an ideal ground for testing potential control laws, but they



(a) Control effectiveness as a function of α and δ_f



(b) Flap schedule, from Eq. (5.28)

Figure 5.14: Effect of using a TE flap, $0 \leq \delta_f \leq 10$ deg. The nondimensional control effectiveness, Non-dimensional $N_{\delta_{asym}} = C_L x_a/c + C_{m,ac}$

also proved as a valuable source for understanding practical difficulties in implementing control laws in articulated wing aircraft. Issues such as tight bounds on the angle of attack and roll rate, which can be produced in computer simulations, are difficult to reproduce in experimental circumstances.

Therefore, we conclude that (a) it is necessary to use wing twist or ailerons, and (b) that the problem of state-dependent sign of control effectiveness needs to be addressed at a theoretical level. A solution to (b) will be beneficial for control reversal problems witnessed at high angles of attack and due to wing flexibility.

Chapter 6

PDE Boundary Control of Flexible Wings

6.1 Motivation

The motivation for considering the problem of boundary control of beams comes from the problem of controlling flexible wings for agile aircraft maneuvers. Suppose that the wing has length L , a mass per unit span of \tilde{m} , and let y denote the spanwise coordinate. Furthermore, let $\xi \triangleq \xi(t, y)$ and $\theta \triangleq \theta(t, y)$ denote the bending and twist displacements, respectively, as shown in Figure 6.1. Let EI_b and $G\tilde{J}$ denote the bending and torsion stiffness, respectively, where I_b is the second moment of area of the cross section about the local bending axis, and \tilde{J} is the torsional constant. Let I_p denote the mass moment of inertia of the wing cross section.

The resultant wind velocity at a given point on the wing, \mathbf{u} , is a sum of the aircraft flight speed \mathbf{u}_B (measured in the body axis) and the wing vibration rate $\mathbf{u}_f = [0 \ 0 \ \dot{\xi}]^T$, so that $\mathbf{u} = \mathbf{T}_{WB}\mathbf{u}_B + \mathbf{u}_f(y)$, where \mathbf{T}_{WB} is the rotation matrix from the body frame to the local wing frame. Let c denote the wing chord length. Let x_{ec} denote the distance between the center of mass and the shear center of the wing, and x_{ac} the distance between the aerodynamic center and shear center. The wing is loaded transversely with a load F_b , which depends on the wind velocity, inertial effects arising from aircraft acceleration and added mass effect, and gravity. An aerodynamic model for calculating F_b , based on an ODE approximation for the time-varying flow dynamics on the wing, can be found in Ref. [27].

Then, the equations for wing vibration dynamics are given by

$$\begin{bmatrix} \tilde{m} & -\tilde{m}x_{ec} \\ -\tilde{m}x_{ec} & I_p \end{bmatrix} \begin{bmatrix} \xi_{tt} \\ \theta_{tt} \end{bmatrix} + \begin{bmatrix} \eta EI_b \xi_{tyyy} + EI_b \xi_{yyyy} \\ -\eta G\tilde{J} \theta_{tyy} - G\tilde{J} \theta_{yy} \end{bmatrix} = \begin{bmatrix} F_b(\xi_y, \theta, \mathbf{u}, \dot{\mathbf{u}}_B) \\ -x_{ac} F_b(\xi_y, \theta, \mathbf{u}, \dot{\mathbf{u}}_B) \end{bmatrix}, \quad (6.1)$$

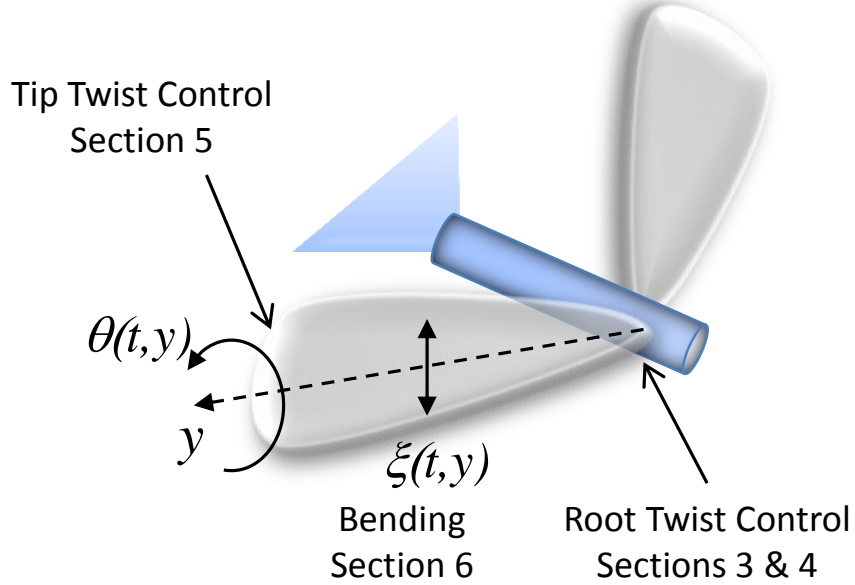


Figure 6.1: Figure showing the problems addressed in this chapter.

where the subscripts t and y denote partial derivatives, i.e., $\xi_{tt} = \frac{\partial \xi}{\partial t^2}$, $\xi_{tyyy} = \frac{\partial \xi}{\partial t \partial y^4}$, and so on. This equation is valid for the right wing, and a similar equation can be derived for the left wing as well. The boundary conditions for tip based actuation are given by

$$\begin{aligned}\xi(0) &= 0, \quad \xi_y(0) = 0, \quad \xi_{yy}(L) = 0, \quad \xi_{yyy}(L) = \frac{F_{\text{tip}}}{EI_b}, \\ \theta(0) &= 0, \quad \theta_y(L) = \frac{M_{\text{tip}}}{GJ}\end{aligned}\tag{6.2}$$

while those for root-based actuation are

$$\begin{aligned}\xi(0) &= 0, \quad \xi_y(0) = \delta_R, \quad \xi_{yy}(L) = 0 = \xi_{yyy}(L) = 0, \\ \theta(0) &= \theta_R, \quad \theta_y(L) = 0\end{aligned}\tag{6.3}$$

Note that both root as well as tip control configurations have one Neumann and one Dirichlet boundary condition. In equations (6.2) and (6.3), F_{tip} and M_{tip} are the applied tip force and twisting moment, respectively. The root actuation variables, δ_R and θ_R , are the *rigid* dihedral (up and down motion) and wing incidence angles. The term η denotes the Kelvin-Voigt damping coefficient. It need not be the same for bending and twisting in general. It is worth noting that

the RHS of equation (6.1) depends on $\dot{\mathbf{u}}_B$ which couples the structural dynamics of the wing to the flight dynamics of the complete aircraft and makes control design a challenging assignment. Physically, F_{tip} and M_{tip} can be realized by using wing tip flaps, not unlike the outboard feathers on a bird's wings. Indeed, trailing edge effectors have been demonstrated to be effective at wing flutter suppression as well [5]. On the other hand, δ_R and θ_R are easier to control and the capability for root actuation is present naturally in flapping wing aircraft.

For the sake of completeness, it is worth noting that the structural dynamics of the wing are coupled to the rigid flight dynamics primarily via aerodynamics and kinematics, and, to a lesser extent, by the variation in mass distribution. The coupled equations of motion have essentially the following structure:

$$\begin{aligned} m(\dot{\mathbf{u}}_B + S(\boldsymbol{\omega}_B)\mathbf{u}_B) + \tilde{m} \int_w (\dot{\mathbf{u}}_f + S(\boldsymbol{\omega}_B)\mathbf{u}_f) dy &= \mathbf{F}_{\text{net}} \\ \mathbf{J}\dot{\boldsymbol{\omega}}_B + S(\boldsymbol{\omega}_B)J\boldsymbol{\omega}_B + \int_w (I_p(y)\dot{\boldsymbol{\omega}}_f + S(\boldsymbol{\omega}_B)I_p(y)\boldsymbol{\omega}_f) dy &= \mathbf{M}_{\text{net}} \end{aligned} \quad (6.4)$$

where: m is the total mass of the aircraft, \mathbf{J} is the moment of inertia tensor for the aircraft, \int_w denotes integration over the wing, $S(\cdot)$ denotes the cross product, and \mathbf{F}_{net} and \mathbf{M}_{net} represent the net external (aerodynamic + gravitational) force and moment on the aircraft. Furthermore, $\boldsymbol{\omega}_B$ and $\boldsymbol{\omega}_f = [0 \ \dot{\theta} \ 0]^T$ are vector representations of the aircraft angular velocity and the twist rate of the wing, with components in the aircraft body axes. The reader is referred to Chapter 2 for a detailed and more general derivation of the equations of motion.

6.2 Problem Formulation

The control objective is to ensure that

$$\lim_{t \rightarrow \infty} \left(\int_0^L \theta(t, y) dy - H(t) \right) = 0 \quad (\text{net lift, or}) \quad (6.5)$$

$$\lim_{t \rightarrow \infty} \left(\int_0^L y\theta(t, y) dy - H_l(t) \right) = 0 \quad (\text{net rolling moment, and}) \quad (6.6)$$

$$\lim_{t \rightarrow \infty} \left(\int_0^L \xi_y(t, y) dy - R(t) \right) = \lim_{t \rightarrow \infty} (\xi(t, L) - R(t)) = 0 \quad (\text{bending displacement of the tip}), \quad (6.7)$$

where $H(t)$, $H_l(t)$ and $R(t)$ are sufficiently smooth time-varying signals. Although we state asymptotic convergence as the objective, we will prove exponential convergence to a uniform ultimate bound. The net lift produced by the wing is $\int_0^L 0.5\rho V^2 c C_L(y, \alpha, \theta) dy$, where ρ is the air density and C_L is the coefficient of lift which depends on the aircraft angle of attack, α , and the local wing twist angle θ . Depending on the aerodynamic theory, the C_L may be a nonlinear function of α and θ , and it is almost always a function of y for a finite-span wing [48]. The term $\int_0^L \xi_y(t, y) dy = \xi(L)$ is a measure of the effective wing dihedral which is a key yaw control parameter [63]. It is approximately the ratio of two components of F_b : the first points along the y direction in Fig. 6.1, the second points upward. Hence, it is a measure of the amount of side (y -) force produced by the wing which, in turn, produces a yawing moment on the aircraft.

Remark: An important question that concerns systems described by PDEs is that of well-posedness. In this thesis, we work primarily with two families of linear PDEs: the wave equation and the Euler-Bernoulli beam equation. The well-posedness depends on the dynamics as well as the choice of boundary conditions. Well-posedness of the closed loop systems considered here can be shown by proving that the input-output map of the system is bounded [84, 12]. For the twisting dynamics actuated by root control, this is achieved by designing the control to map the system onto well-posed and exponentially stable dynamics. For twisting dynamics actuated at the wing tip, the input-output map is actually a finite order ODE, and its well-posedness follows from the standard existence and uniqueness theorems for ODEs. Finally, the well-posedness of the closed loop bending dynamics can be shown using a transfer function approach [12].

6.3 Boundary Control of Twisting Motion: Root Control

Consider the case where the flexible wing needs to be controlled from the wing root; i.e., the PDE for wing twist is

$$\begin{aligned} \theta_{tt} - b\theta_{t\bar{y}y} - a\theta_{yy} &= M\theta, \\ \theta_y(t, L) &= 0, \quad \theta(t, 0) = U(t) \quad (\text{wing tip free, root displacement controlled}), \end{aligned} \tag{6.8}$$

where $a = G\tilde{J}/I_p$, $b = \eta a$, and $M\theta = -x_a c F_b/I_p$ in equation (6.1), where the net force, F_b , has been assumed to be linear in θ . It is easy to check that the system has an infinite relative degree with respect to the output in equation (6.5). Thus, one needs to approach this problem in two steps. In the first step, the desired tracking response is determined. In the second step, the error dynamics between the system behavior and the desired tracking response are stabilized using backstepping [40]. Therefore, the control $U(t)$ may be decomposed into two parts

$$U(t) = U_d(t) + u(t), \quad (6.9)$$

where U_d is the desired boundary condition at the wing root for which the integral objective, equation (6.5), is satisfied, while $u(t)$ is the stabilizing controller obtained from backstepping.

6.3.1 Boundary Condition when $H(t) \equiv H$

If the desired behavior is an equilibrium (i.e., $H(t) \equiv H$, a constant), then the steady state PDE is obtained from equation (6.8) by neglecting the time-dependence of θ :

$$\theta_{d,yy} + \mu^2 \theta_d = 0, \quad \theta_{d,y}(L) = 0, \quad \theta_d(0) = U_d \quad (6.10)$$

where $\mu^2 = M/a$ and the subscript, d , denotes the desired (also, in this case, steady) state. The following control law, U_d , ensures that the condition equation (6.5) is satisfied.

$$U_d = \frac{\mu H}{\tan(\mu L)} \quad (6.11)$$

Alternatively, the desired behavior may be time varying in which case the boundary condition prescribed at the root needs to be determined separately. The boundary condition at the wing tip, on the other hand, is relatively easy to choose because, as shown in Section 6.5, the system has a relative degree of 2 for the outputs in equations (6.5) and (6.6), and the wing tip moment as the control input.

6.3.2 Backstepping for Regulation to a Steady State

Backstepping is carried out in two steps: (a) the target dynamics are identified, and (b) a backstepping (Volterra) transformation converts the system dynamics (in this case, the error dynamics) into the target dynamics and the control signal $u(t)$ is obtained in the process. The method described by Krstic and Smyshlyaev [40] is used here. Let $\tilde{\theta}$ denote the error between the system state and the desired steady state value in equation (6.10), i.e., $\tilde{\theta} = \theta - \theta_d$.

Next, consider the target dynamics described by the PDE

$$\begin{aligned} v_{tt} - bv_{tyy} - av_{yy} &= (M - ap)v - bpv_t, \\ v(t, 0) &= v_y(t, L) = 0 \end{aligned} \quad (6.12)$$

Using the method of separation of variables, it is easy to check that the eigenvalues of this system are the solutions of

$$\begin{aligned} \lambda^2 + b(\nu^2 + p)\lambda + (a(\nu^2 + p) - M) &= 0 \\ \text{where } \nu = \frac{2n+1}{2}\frac{\pi}{L}, \quad n = 0, 1, 2, \dots & \end{aligned} \quad (6.13)$$

The target dynamics are stable if and only if the control design parameter, p , satisfies

$$p > \max\left(\frac{M}{a} - \frac{\pi^2}{4L^2}, -\frac{\pi^2}{4L^2}\right) \quad (6.14)$$

A dummy spatial variable x is introduced and the Volterra transformation between $\tilde{\theta}$ (the error between the actual dynamics and the desired steady state in equation (6.12)) and v (the target dynamics for the error state) is given by

$$v(t, y) = \tilde{\theta}(t, y) - \int_L^y k(y, x)\tilde{\theta}(t, x)dx \quad (6.15)$$

It is helpful to recall that the $\tilde{\theta}$ dynamics are

$$\tilde{\theta}_{tt} - b\tilde{\theta}_{tyy} - a\tilde{\theta}_{yy} = M\tilde{\theta}, \quad \tilde{\theta}(t, 0) = u(t), \quad \tilde{\theta}_y(t, L) = 0 \quad (6.16)$$

In order to solve for $k(x, y)$, substitute equations (6.15) and (6.16) into equation (6.12). Next, isolating the coefficients of v and v_t , the following Klein - Gordon PDE for $k(y, x)$ is derived [40]

$$\begin{aligned} k_{xx}(y, x) - k_{yy}(y, x) &= -pk(y, x) \\ k(y, y) &= \frac{p}{2}(L - y), \quad k_x(y, L) = 0 \end{aligned} \quad (6.17)$$

The control input is found from equation (6.15)

$$u(t) = \tilde{\theta}(t, 0) = - \int_0^L k(0, x) \tilde{\theta}(t, x) dx \quad (6.18)$$

It remains to explain the derivation of $k(x, y)$. First, we derive expressions for v_{tt} and v_{yy} .

$$\begin{aligned} v_{tt} &= \tilde{\theta}_{tt} - \int_L^y k(y, x) \tilde{\theta}_{tt}(x) dx \\ &= b\tilde{\theta}_{tyy} + a\tilde{\theta}_{yy} + M\tilde{\theta} - \int_L^y k(y, x) \left(b\tilde{\theta}_{txx}(x) + a\tilde{\theta}_{xx}(x) + M\tilde{\theta}(x) \right) dx \\ &= b\tilde{\theta}_{tyy} + a\tilde{\theta}_{yy} + M\tilde{\theta} - \int_L^y k(y, x) M\tilde{\theta}(x) dx - \int_L^y k_{xx}(y, x) \left(b\tilde{\theta}_t(x) + a\tilde{\theta}(x) \right) dx \\ &\quad - k(y, y)(b\tilde{\theta}_{ty}(y) + a\tilde{\theta}_y(y)) + k_x(y, y)(b\tilde{\theta}_t(y) + a\tilde{\theta}(y)) - k_x(y, L)(b\tilde{\theta}_t(L) + a\tilde{\theta}(L)) \end{aligned} \quad (6.19)$$

The expression for v_{yy} can be derived as follows:

$$\begin{aligned} v_y(y) &= \tilde{\theta}_y(y) - k(y, y)\tilde{\theta}(y) - \int_L^y k_y(y, x) \tilde{\theta}(x) dx \\ v_{yy}(y) &= \tilde{\theta}_{yy}(y) - 2k_y(y, y)\tilde{\theta}(y) - k_x(y, y)\tilde{\theta}(y) - k(y, y)\tilde{\theta}_y(y) - \int_L^y k_{yy}(y, x) \tilde{\theta}(x) dx \end{aligned} \quad (6.20)$$

The expression for v_{tyy} is similar to that for v_{yy} . We substitute equations (6.19) and (6.20) into equation (6.12) and isolate the coefficients of $\tilde{\theta}$ and $\tilde{\theta}_y$ in the integrand as well as outside the integral. This yields the PDE $k_{xx} - k_{yy} = -pk$ and one of the two boundary conditions, viz., $k_x(y, L) = 0$. It also yields the condition $k(y, y) = -\frac{p}{2}y + \text{constant}$. From the first equation of (6.20), it follows that $k(L, L) = 0$ since $\tilde{\theta}_y(L) = v_y(L) = 0$. Therefore, $k(y, y) = \frac{p}{2}(L - y)$, which is the second boundary condition.

One can solve for $k(y, x)$ using successive approximations, as described in Ref. [40]. The solution

is given in terms of the modified Bessel function I_1 ^{*}:

$$k(y, x) = p(L - y) \frac{I_1(\sqrt{p((L - y)^2 - (L - x)^2)})}{\sqrt{p((L - y)^2 - (L - x)^2))}} \quad (6.21)$$

In summary, the control signal, $U(t)$, is given by equations (6.9), (6.18) and (6.21).

6.3.3 Discussion

A few observations are worth noting here.

1. If the wing is reasonably stiff $\left(\frac{MI_p}{G\tilde{J}} = \frac{M}{a} < \frac{\pi^2}{4L^2} \right)$; i.e., $G\tilde{J} > 4L^2 MI_p / \pi^2$, the system can be stabilized with $p = 0$, i.e., with no additional control input.
2. For stability, it is essential that $b > 0$, i.e., the Kelvin-Voigt damping coefficient is always positive. A negative damping could be introduced due to aerodynamics, but it can be compensated by the term $b p v_t$ and wing flutter can be prevented. The compensation in damping imposes an additional constraint on p .
3. The controller in equation (6.18) requires that the twist angle at all points on the wing be known. This difficulty can be circumvented by designing a PDE-based observer [40] or, practically, using a series of distributed sensors and fitting their output with an *a priori* designed spline.
4. Damping and stiffness cannot be added independently. They are added in the ratio b/a .
5. Finally, the control law does not require that a , b or M be known for the purpose of regulation. We only need to know bounds on a and M to choose an appropriate value of the gain p .

6.3.4 Local Linear Analysis

A nonlinear problem which is of interest to the present discussion would be to regulate a PDE of the form

$$\theta_{tt} - b\theta_{t\bar{y}\bar{y}} - a\theta_{yy} = -x_a c F_b(\theta, \theta_t), \quad \theta_y(t, L) = 0, \quad \theta(t, 0) = U(t) \quad (6.22)$$

* A modified Bessel function, $I_n(y)$, satisfies $y^2 I_n''(y) + y I_n'(y) - (y^2 + n^2) I_n(y) = 0$.

where x_a is the normalized (with respect to the chord length c) distance between the shear center and the aerodynamic center of the wing. Recall that $a = G\tilde{J}/I_p$, $b = \eta a$, and the control input is, physically, θ_R from equation (6.3). The nonlinearity on the RHS arises from the inclusion of θ_t in the local flow velocity, and is widely used, for e.g., in flutter prediction [31]. Consider the error dynamics between the actual system and the steady state.

Desired: $\zeta_{tt} - b\zeta_{tyy} - a\zeta_{yy} = -x_a c F_b(\zeta, \zeta_t)$, $\zeta_y(t, L) = 0$, $\zeta(t, 0) = U_d(t)$

Error Dynamics: $e_{tt} - be_{tyy} - ae_{yy} = -x_a c F_b(\zeta, \zeta_t) + x_a c F_b(\zeta_{ss}, 0)$, $e_y(t, L) = 0$, $e(t, 0) \neq 0$

where the subscript ‘ss’ has been used to denote the steady state. Notice that, on this occasion, we have no simple expression for U_d . Instead, it must be calculated on a case-by-case basis for different nonlinearities on the right hand side. The nonlinear term can be approximated to the first order to get

$$e_{tt} - be_{tyy} - ae_{yy} = M_2 e_t + M_1 e, \quad e_y(t, L) = 0, \quad e(t, 0) = u(t) \quad (6.24)$$

where the coefficients $M_1 = -x_a c \frac{\partial F_b(\theta, \theta_t)}{\partial \theta}$ and $M_2 = -x_a c \frac{\partial F_b(\theta, \theta_t)}{\partial \theta_t}$ depend on the steady state θ .

Consider the following target dynamics for backstepping:

$$\begin{aligned} v_{tt} - bv_{tyy} - av_{yy} &= M_2 v_t + M_1 v - apv - bpv_t, \\ v(0) &= v_y(L) = 0, \end{aligned} \quad (6.25)$$

whose characteristic equation is

$$\lambda^2 + (bv^2 + bp - M_2)\lambda + (a(\nu^2 + p) - M_1) = 0 \quad (6.26)$$

where $\nu^2 = \frac{\pi^2}{4L^2}$. The target dynamics are stable if and only if

$$p > \max \left\{ \left(\frac{M_1}{a} - \nu^2 \right), \left(\frac{M_2}{b} - \nu^2 \right) \right\} \quad (6.27)$$

The rest of the backstepping transformation is identical to that described in Section 6.3.2.

6.3.5 Lyapunov-based Analysis for Spatially-Varying $M(y)$

In this section, we show that backstepping, described in Section 6.3.2, can be used to control nonlinear systems of the form

$$\theta_{tt}(t, y) - b\tilde{\theta}_{tyy} - a\tilde{\theta}_{yy} = M(y)\tilde{\theta}, \quad \tilde{\theta}_y(L) = 0, \quad \tilde{\theta}(0) = u(t) \quad (6.28)$$

Recall that $a = G\tilde{J}/I_p$, $b = \eta a$ and $M(y)\theta = -x_a c F_b/I_p$. The term $M(y) > 0$ represents the moment distribution on the wing and is a (usually nonlinear) function of the wing geometry. Physically, it captures the effect of downwash on a finite wing [48]. We have set $U_d(t) = 0$, which implies that $U(t) = u(t)$; i.e., a regulation controller is to be designed. Stability analysis is completed in three steps:

1. First, the backstepping transformation in equations (6.15) and (6.17) is invoked to transform the system dynamics into “target” dynamics (see equation (6.30)).
2. The target dynamics are decomposed into “nominal” dynamics and a vanishing perturbation.
3. The nominal dynamics are shown to be exponentially stable, which implies that there exists a class of functions $M(y)$ for which the target system is exponentially stable.

The first step is to identify the target dynamics. Using the Volterra transformation (6.15), (6.17) and (6.21), i.e.,

$$\begin{aligned} v(t, y) &= \tilde{\theta}(t, y) - \int_L^y k(y, x)\tilde{\theta}(t, x)dx, \\ k(y, x) &= p(L-y) \frac{I_1(\sqrt{p((L-y)^2-(L-x)^2)})}{\sqrt{p((L-y)^2-(L-x)^2)}}, \end{aligned} \quad (6.29)$$

we obtain the target dynamics

$$\begin{aligned} v_{tt}(y) - bv_{tyy} - av_{yy} - (M(y) - ap)v + bpv_t &= M(y) \int_L^y k(y, x)\tilde{\theta}(x)dx - \int_L^y k(y, x)M(x)\tilde{\theta}(x)dx, \\ &= \int_L^y M'(x) \int_L^x k(y, z)\tilde{\theta}(z)dz dx \triangleq \Pi(y) \\ v(0) = v'(L) = 0, \quad p > \max_y \frac{M(y)}{a} \end{aligned} \quad (6.30)$$

where $M'(x) = dM/dx$.

The RHS of equation (6.30) may be viewed as a perturbation. The bound on the RHS is calculated as follows:

$$\begin{aligned}\Pi(y) &\leq \left(\max_y \int_0^L |k(y, z)\tilde{\theta}(z)| dz \right) \left(\int_0^L |M'(x)| dx \right) \\ &\leq \left(\int_0^L |M'(x)| dx \right) \left(\max_y \sqrt{\int_0^L k(y, z)^2 dz} \right) \left(\sqrt{\int_0^L \tilde{\theta}(z)^2 dz} \right) = K_1 \|\tilde{\theta}\| \quad (6.31)\end{aligned}$$

where the constant K_1 is a (known) bound on $\left(\int_0^L |M'(x)| dx \right) \left(\max_y \sqrt{\int_0^L k(y, z)^2 dz} \right)$ and $\|\tilde{\theta}\| = \sqrt{\int_0^L \tilde{\theta}(z)^2 dz}$ (the norm of θ). Furthermore, as shown in Ref. [40], there exists a bounded function $l(y, x)$ such that

$$\begin{aligned}\tilde{\theta}(t, y) &= v(t, y) - \int_L^y l(y, x)v(t, x)dx, \\ \implies \|\tilde{\theta}\| &\leq K_2 \|v\|, \quad (6.32)\end{aligned}$$

where K_2 is another known constant. Hence, from equations (6.31) and (6.32), it follows that

$$\Pi(y) \leq K_1 K_2 \|v\| \quad (6.33)$$

Hence, the perturbation on the RHS of equation (6.30) is vanishing in v .

Next, we prove the exponential stability of the nominal dynamics given by

$$v_{tt}(y) - bv_{tyy} - av_{yy} = (M(y) - ap)v - bpv_t, \quad v(0) = v'(L) = 0, \quad p > \max_y \frac{M(y)}{a} \quad (6.34)$$

In order to show \mathcal{L}_2 stability, consider the Lyapunov function

$$V(t) = \int_0^L \left(\frac{v_t^2}{2} + \frac{av_y^2}{2} + (ap - M(y)) \frac{v^2}{2} + \delta vv_t \right) dy \quad (6.35)$$

The above Lyapunov function is positive definite for a large enough $p > \max_y \frac{M(y)}{a}$ and small enough $\delta > 0$. A bound for δ will be derived presently. Differentiating $V(t)$ with respect to t yields

$$\dot{V}(t) = \int_0^L (v_t v_{tt} + av_y v_{ty} + (ap - M(y))vv_t + \delta v_t^2 + \delta vv_{tt}) \quad (6.36)$$

The first term in the integrand can be expanded, followed by integration by parts, so that

$$\begin{aligned} \int_0^L v_t v_{tt} dy &= \int_0^L (bv_{tyy} v_t + av_{yy} v_t - (ap - M(y))vv_t - bp v_t^2) dy \\ &= \int_0^L (-bv_{ty}^2 - av_y v_{ty} - (ap - M(y))vv_t - bp v_t^2) dy \end{aligned} \quad (6.37)$$

A similar expression can be calculated for $\int_0^L \delta vv_{tt} dy$. Substituting equation (6.37) into (6.36), it follows that

$$\dot{V}(t) = \int_0^L ((-bp + \delta)v_t^2 - bv_{ty}^2 - a\delta v_y^2 - (ap - M(y))\delta v^2) dy + \int_0^L (\delta bv v_{tyy} - \delta bp v v_t) dy$$

Since $v(0) = v_y(L) = 0$, it follows that

$$\dot{V}(t) = \int_0^L ((-bp + \delta)v_t^2 - bv_{ty}^2 - a\delta v_y^2 - (ap - M(y))\delta v^2) dy + \int_0^L (-\delta bv_y v_{ty} - \delta bp v v_t) dy \quad (6.38)$$

Using Young's and Cauchy-Schwarz inequalities, it follows that

$$\int_0^L (-\delta bv_y v_{ty} - \delta bp v v_t) dy \leq \frac{\delta b}{2} \int_0^L \left(\delta v_y^2 + \frac{v_{ty}^2}{\delta} \right) dy + \frac{\delta bp}{2} \int_0^L \left(\delta v^2 + \frac{v_t^2}{\delta} \right) dy \quad (6.39)$$

Therefore,

$$\dot{V}(t) \leq \int_0^L \left(\left(-bp + \delta + \frac{pb}{2} \right) v_t^2 - \frac{b}{2} v_{ty}^2 - (a - 0.5\delta b)\delta v_y^2 - \left(ap - M(y) - \frac{\delta pb}{2} \right) \delta v^2 \right) dy$$

If δ is chosen such that

$$\delta < \min \left\{ 1, \frac{(b - 2\kappa)p}{2}, \frac{2(ap - M(y) - \kappa p)}{bp} \right\} \quad \forall y \leq L \quad (6.40)$$

where κ is another small number such that $\kappa < \min(a - M(y)/p, b) \quad \forall y \leq L$, then it follows that

$$\dot{V} \leq -\frac{\kappa\delta}{2}V \quad (6.41)$$

This proves exponential stability and $\lim_{t \rightarrow \infty} v = 0$. Note that the condition $p > \max_y \frac{M(y)}{a} + \kappa$ is stronger than the condition obtained for linear systems. Increasing p allows us to choose a larger κ , subject to the constraint arising from b , to improve the guaranteed rate of convergence. Furthermore, since δ does not appear in the control law, it does not have any bearing on the performance and stability of the actual system.

The nominal system has been shown to be exponentially stable. Furthermore, the perturbation on the RHS of equation (6.30) is vanishing in v , as shown in equation (6.33). Hence, it follows that the nominal system is robust to sufficiently small perturbations. In particular, it is exponentially stable for sufficiently small $\int_0^L |M'(y)|dy$ (e.g., see Lemma 9.1 in Khalil [37] for an ODE analogue), i.e., for a sufficiently small K_1 in equation (6.31).

A theoretical bound on K_1 can be calculated by noting that, had we retained the perturbation term

$$\Pi(y) \triangleq \int_L^y M'(x) \int_L^x k(y, z) \tilde{\theta}(z) dz dx,$$

it would have entered $\dot{V}(t)$ via terms involving v_{tt} in equation (6.38). Using the Cauchy-Schwarz inequality, it can be shown that the change in $\dot{V}(t)$ arising from the inclusion of $\Pi(y)$, denoted by $\Delta\dot{V}$, is given by

$$\Delta\dot{V}(t) \leq 2K_1 K_2 \underbrace{\left(1 + \frac{\delta}{\sqrt{ap - M_{\max}}}\right)}_{K_3} V = K_1 K_2 K_3 V \quad (6.42)$$

Thus, if $K_1 < \frac{\kappa\delta - 2\epsilon}{2K_2 K_3}$, where $2\epsilon < \kappa\delta$, then the system continues to remain exponentially stable with a guaranteed convergence rate of ϵ for V .

Remark: Stability could have been proven even with $\delta = 0$. In that case, $\dot{V}(t) = \int_0^L (-bpv_t^2 - bv_{ty}^2) dy$ which is negative semi-definite. Clearly, the dynamics would converge to a steady state which is the solution of $av_{yy} = (M(y) - ap)v$ and $v(0) = v_y(L) = 0$. This boundary value problem has the trivial solution $v \equiv 0$ as the only solution for almost all $M(y)$. The constant p has to be chosen to

prevent the existence of multiple solutions.

6.4 Tracking Controller for Twist

In this section, we consider a linear twist PDE with constant coefficients. The backstepping method described in the previous section is used for designing a tracking controller. We consider the system realized via the coordinate transformation

$$w(t, y) = \int_L^y \theta(t, x) dx \quad (6.43)$$

Physically, $w(t, y)$ measures the lift generated by the outboard section of the wing starting at y and terminating at the wing tip. The lift produced at the wing tip is zero, which is physically correct. Note that $\theta_y(t, L) = 0$ at the free end $y = L$. Hence, it follows that

$$\begin{aligned} w_{tt}(t, y) &= \int_L^y \theta_{tt}(t, x) dx = \int_L^y (b\theta_{txx}(t, x) + a\theta_{xx}(t, x) + M\theta(t, x)) dx \\ &= b\theta_{ty}(t, y) + a\theta_y(t, y) + Mw(t, y) = bw_{tyy}(t, y) + aw_{yy}(t, y) + Mw(t, y) \end{aligned} \quad (6.44)$$

Thus, the dynamics of w are described by the PDE

$$w_{tt} - bw_{tyy} - aw_{yy} = Mw, \quad w(t, L) = 0, \quad w_y(t, 0) = u(t), \quad (6.45)$$

where $u(t)$ is the control signal (θ_R in equation (6.3)), and recall that $a = G\tilde{J}/I_p$ and $b = \eta a$. Furthermore, we defined M so that $M\theta = -x_a c F_b / I_p$, where F_b is a linear function of θ . Note that $w_y(t, y) = \theta(t, y)$. Recall that the control objective is to ensure that $\lim_{t \rightarrow \infty} (\int_0^L \theta dy - H(t)) = 0$ (see equation (6.5)). The control objective is now recast to ensuring that $\lim_{t \rightarrow \infty} (w(t, 0) + H(t)) = 0$, i.e., $\lim_{t \rightarrow \infty} w(t, 0) = -H(t)$.

The method presented in this section rests on the following steps:

1. Obtain a backstepping transformation $w \mapsto v$, where v dynamics are similar to those in Section 6.3.2, although the boundary conditions are changed to match the tracking requirement,
2. Identify the boundary conditions and

3. Derive a motion planning-based design for the boundary conditions of the v dynamics.

Step 1: Volterra Transform: Define the Volterra transformation

$$v(t, y) = w(t, y) - \int_L^y k(y, x)w(t, x)dx \quad (6.46)$$

and the v -dynamics

$$v_{tt} - bv_{tyy} - av_{yy} = Mv - bpv_t - apv, \quad v(t, L) = 0, \quad p > 0 \quad (6.47)$$

Note that we have prescribed only one boundary condition for v . The second boundary condition, $v_y(t, 0)$, has to be calculated to ensure that the $w(t, 0) \approx -H(t)$ (this is what we can guarantee in practice, in place of asymptotic convergence). The target dynamics in equation (6.47) are very similar to those designed for the regulation problem, in equation (6.12). The critical difference is in the choice of the boundary conditions, which are chosen to match the problem. For the regulation problem recall that we had prescribed $v(t, 0) = v_y(t, L) = 0$. On the other hand, we now prescribe $v(t, L) = 0$ and choose $v_y(t, 0)$ using motion planning.

The steps from Section 6.3.2 are repeated to solve for $k(y, x)$. It follows that $k(y, x)$ satisfies the PDE

$$k_{xx}(y, x) - k_{yy}(y, x) = -pk(y, x), \quad k(y, L) = 0, \quad k(y, y) = \frac{p}{2}(L - y) \quad (6.48)$$

The solution to this PDE is given in terms of the modified Bessel function, $I_1(\cdot)$, as

$$k(x, y) = p(L - x) \frac{I_1\left(\sqrt{p((L - y)^2 - (L - x)^2)}\right)}{\sqrt{p((L - y)^2 - (L - x)^2)}} \quad (6.49)$$

Step 2: Boundary Condition, $v(0)$, for tracking: We have already ascertained that $v(L) = 0$. From equation (6.46), it follows that

$$v(t, 0) = w(t, 0) + \int_0^L k(0, x)w(t, x)dx \quad (6.50)$$

The above equation does not yield an exact relationship to connect $H(t)$ and $v(t, 0)$. Instead, we

need to determine an appropriate reference value for $v(t, 0)$, call it $H_0(t)$, which ensures that $w_0(t, 0)$ approximately tracks $-H(t)$. For example, we could approximate $w(t, x) \approx f_1(x)w(t, 0)$, $f_1(0) = 1$, where $f_1(x)$ denotes the shape of the first twisting mode. Thus, we set

$$H_0(t) = -H(t) \left(1 + \int_0^L k(0, x) f_1(x) dx \right) \quad (6.51)$$

It is important to appreciate that ignoring the higher modes has no repurcussions for stability since it is guaranteed separately. At the same time, it may be necessary to include more than one mode if there are tight bounds on the tracking error. An similar approach based on backstepping, but for constant reference signals, has been derived in Ref. [85].

Step 3: Motion Planning for Wing Twist: TWe design a motion planning-based algorithm (see Ch. 12 in Ref. [40]). We define a new state v^r , where the subscript ‘r’ denotes the reference value. The dynamics of v^r are given by a PDE that is identical to (6.47):

$$v_{tt}^r - bv_{tyy}^r - av_{yy}^r = Mv^r - bpv_t^r - apv^r, \quad v^r(t, L) = 0, \quad (6.52)$$

where $v_y^r(t, 0)$ is the control input to be designed using motion planning to ensure that $v^r(t, 0)$ tracks $H_0(t)$.

Since $v^r(t, L) = 0$, we expand $v^r(t, y)$ as a polynomial

$$v^r(t, y) = \sum_{j=1}^N \eta_j(t) \frac{(L-y)^j}{j!} \quad (6.53)$$

Substituting for v in (6.47), we get

$$\ddot{\eta}_j(t) + bp\dot{\eta}_j(t) + (ap - M)\eta_j(t) = b\eta_{j+2}(t) + a\eta_{j+2}(t) \quad (6.54)$$

The requirement that $v^r(t, 0) = H_0(t)$ gives

$$\sum_{j=1}^N \eta_j(t) \frac{L^j}{j!} = H_0(t) \quad (6.55)$$

The value of N can be chosen on a case-by-case basis. As an illustration, if we truncate the series at $N = 3$, we get

$$\ddot{\eta}_1(t) + bp\dot{\eta}_1(t) + (ap - M)\eta_1(t) = b\eta_3(t) + a\eta_3(t) \quad (6.56)$$

A similar equation can be obtained for $\eta_2(t)$, with the right hand side equal to zero. Therefore, η_2 converges to zero exponentially fast and can be ignored. The requirement that $v^r(t, 0) = H_0(t)$ gives

$$\eta_1(t)L + \eta_3(t)\frac{L^3}{6} = H_0(t) \quad (6.57)$$

Thus,

$$\eta_1(t) = \frac{H_0(t)}{L} - \eta_3(t)\frac{L^2}{6} \quad (6.58)$$

Substituting into (6.56) gives

$$\frac{L^2}{6}\ddot{\eta}_3(t) + \left(\frac{bpL^2}{6} + b\right)\eta_3(t) + \left(\frac{(ap - M)L^2}{6} + a\right)\eta_3(t) = \frac{\ddot{H}_0(t) + bp\dot{H}_0(t) + (ap - M)H_0(t)}{L} \quad (6.59)$$

Then, $v_y^r(t, 0)$ can be calculated by differentiating both sides of (6.53)

$$v_y^r(t, 0) = -\eta_1(t) - \eta_3(t)\frac{L^2}{2} \quad (6.60)$$

where $v_y^r(t, y) = \partial v^r(t, y)/\partial y$.

We set the boundary condition $v_y(t, 0) = v_y^r(t, 0)$. Let $\tilde{v}(t, y) = v(t, y) - v^r(t, y)$. It is straightforward to check that the dynamics of \tilde{v} are given by the exponentially stable PDE

$$\tilde{v}_{tt} - b\tilde{v}_{tgy} - a\tilde{v}_{yy} = M\tilde{v} - bp\tilde{v}_t - ap\tilde{v}, \quad \tilde{v}(t, L) = \tilde{v}_y(t, 0) = 0 \quad (6.61)$$

Thus, in particular, it follows that $v(t, 0) \rightarrow v^r(t, 0)$ exponentially fast and $v(t, 0)$ tracks $H_0(t)$.

An expression for $v_y(t, y)$ can be found by differentiating both sides of the Volterra transform in (6.46):

$$v_y(t, y) = w_y(t, y) - k(y, y)w(t, y) - \int_L^y k_y(y, x)w(t, x)dx \quad (6.62)$$

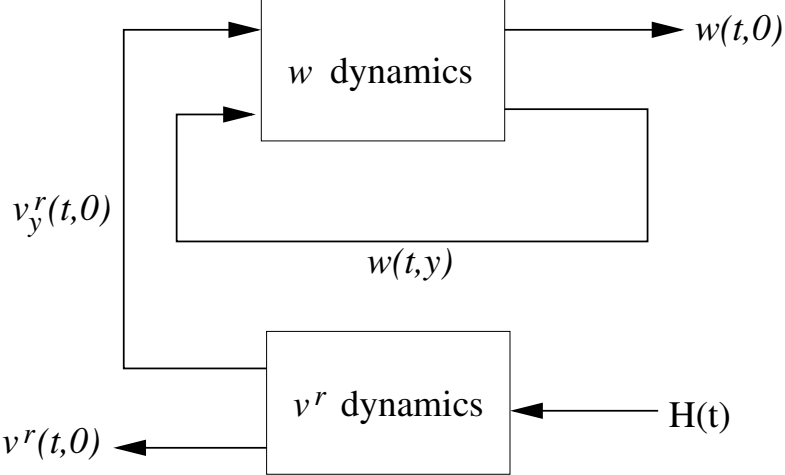


Figure 6.2: Block diagram showing the tracking controller for twist (θ) dynamics. This structure is identical to the classic strict feedback structure for systems described by ODEs [39].

Finally, the control input to the system (w) dynamics is calculated:

$$U(t) = \theta(t, 0) = w_y(t, 0) = v_y^r(t, 0) + k(0, 0)w(t, 0) - \underbrace{\int_0^L k_y(0, x)w(t, x)dx}_{\text{feedback}} \quad (6.63)$$

It is interesting to note that setting $v_y^r = 0$ in (6.63) reduces $u(t)$ to a regulator controller. Therefore, the term $v_y(t, 0)$ plays the role of the (open loop) ‘‘reference half’’ of the control signal, while the remaining two terms act as ‘‘stabilizers.’’ It is interesting that $w(t, 0)$ makes an explicit appearance in the stabilizing half of the controller, rather than the reference half (whose task is to ensure that $w(t, 0)$ tracks the reference signal $-H(t)$.)

The control design procedure has been illustrated via a block diagram in Fig. 6.2.

Remark: The v dynamics can be shown to be stable using the Lyapunov argument in Section 6.3.5. Since equation (6.46) is a diffeomorphism, we can find another function $l(y, x)$ (which is expressed in terms of the Bessel function J_1 [40]) such that $w(t, y) = v(t, y) - \int_L^y l(y, x)v(t, x)dx$, and $l(y, x)$ is bounded for all $0 \leq y \leq x \leq L$. Since the v -dynamics are stable, it follows that the w -dynamics are stable as well.

6.5 Boundary Control of Twisting Motion: Wing Tip Control

Although backstepping can be employed when the twisting moment at the wing tip is used as the control input, it turns out that there is a simpler alternative, as described in this section. It relies on the fact that the system has a finite relative degree for the input-output combination of $\int_0^L \theta(t, y) dy$ and the tip moment.

6.5.1 Tip Boundary Control when All Parameters are Known

As in the previous section, one can design a backstepping controller for the case where a control moment is applied to the free end ($y = L$) of the wing while the other end ($y = 0$) is clamped. In fact, the procedure in both cases is identical, although the final expressions for the control law differ slightly. Alternately, in case of MAVs, one may do without a stabilizing controller. The “tracking half” of the controller ($U_d(t)$ in equation (6.9)) may be designed using the output measurements. This method is useful for adaptive designs as well. We consider the wing model

$$\theta_{tt} - b\theta_{t\bar{y}} - a\theta_{\bar{y}\bar{y}} = M\theta, \quad \theta(t, 0) = 0, \quad \theta_y(t, L) = u(t) \quad (6.64)$$

where the control input is a moment applied at the wing tip, ($u(t) = \theta_y(L, t) = M_{\text{tip}}$ in equation (6.2)), and $b = \eta a = \eta G \tilde{J} / I_p$. Furthermore, we defined M so that $M\theta = -x_a c F_b / I_p$, where F_b is a linear function of θ . The control objective is to ensure that

$$\lim_{t \rightarrow \infty} \left(\int_0^L \theta(t, y) dy - H(t) \right) = 0 \quad (6.65)$$

The problem will be solved using a linear control approach. Let $e(t) = \int_0^L \theta(t, y) dy - H(t)$ denote the error which needs to be regulated. Then,

$$\begin{aligned} \ddot{e} &= \int_0^L \theta_{tt}(t, y) dy - \ddot{H}(t) \\ &= \int_0^L (a\theta_{yy} + b\theta_{t\bar{y}} + M\theta) dy - \ddot{H}(t) \\ &= a\theta_y(L) - a\theta_y(0) + b\theta_{ty}(L) - b\theta_{ty}(0) + M e(t) - \ddot{H}(t) + M H(t) \\ &= b\dot{u}(t) + au(t) - a\theta_y(0) - b\theta_{ty}(0) + M e(t) - \ddot{H}(t) + M H(t) \end{aligned} \quad (6.66)$$

A dynamic controller of the form

$$b\dot{u}(t) + au(t) = \ddot{H}(t) - MH(t) - (M+k)e(t) - k_c\dot{e}(t) + a\theta_y(0) + b\theta_{ty}(0) \quad (6.67)$$

renders the system into the spring-mass form

$$\ddot{e}(t) + k_c\dot{e}(t) + ke(t) = 0. \quad (6.68)$$

The control law in equation (6.67) suggests that θ need not be monitored or measured at all locations on the wing. Instead, only $\theta_y(0)$ needs to be measured or estimated. The reference signal $H(t)$ is known. It may be difficult to inject damping because $\dot{e}(t)$ is the rate of change of the lift and in practice, would require differentiating noisy acceleration signals.

Another interesting observation is that although the PDE system had an infinite relative degree when the root twist was chosen as the control input, the relative degree is 2 when twisting moment at the wing tip is considered as the input. This facilitates the control law design in this section considerably. The control law design described in this section lends itself readily to adaptation should a and/or M be unknown.

6.5.2 Tracking and Stability

The problems of tracking and stabilization are distinct because the PDE system is infinite dimensional. Nevertheless, a tracking controller improves stability as described presently. The best way to understand the influence of a tracking controller is to set $H = 0$. Make a coordinate transformation $w(t, y) = \int_L^y \theta(t, y) dy$, similar to equation (6.43), so that achieving $H = 0$ is equivalent to achieving $w(0) \triangleq w(t, 0) = 0$. It follows that the transformed dynamics, with $H = 0$ ensured by the tracking algorithm, are given by

$$w_{tt}(t, y) - bw_{tyy}(t, y) - aw_{yy}(t, y) = Mw(t, y) - bw_{tyy}(t, 0) - aw_{yy}(t, 0), \quad w(L) = w(0) = 0, \quad w'(0) = 0 \quad (6.69)$$

The third boundary condition is not entirely independent. Let $w(t, y) = \eta(t)\phi(y)$. Then, we get

$$\frac{\ddot{\eta}(t) - M\eta(t)}{b\dot{\eta}(t) + a\eta(t)} = \frac{\phi''(y) - \phi''(0)}{\phi(y)} = -\lambda^2, \quad (6.70)$$

where λ is a constant. It follows that the condition for stability is $M/a < \lambda^2$. The differential equation for $\phi(y)$ can be solved to get

$$\phi(y) = A \sin(\lambda y) + B \cos(\lambda y) + \phi''(0)/\lambda^2 \quad (6.71)$$

The boundary conditions $\phi(0) = \phi'(0) = 0$ lead to $\phi(y) = B(\cos(\lambda y) - 1)$. Finally,

$$\phi(L) = 0 \implies \lambda = 2n\pi/L, \quad \because \phi(L) = 0, \quad n = 1, 2, \dots \quad (6.72)$$

Had we not imposed the condition $H(0) = 0$, we would have obtained $M/a < \pi^2/(4L^2)$ as the condition for stability. Since the condition for open loop stability is given by $M/a < \lambda^2 = 4\pi^2/L^2$, it follows that the stability margin improves by a factor of sixteen *using only the tracking controller*, although, it does not stabilize the wing for all values of M and a as backstepping does. In principle, the tracking controller converts the wing from a cantilever beam to a clamped-clamped beam. In practice, this translates to the ability to increase the wing flexibility by an order of magnitude, or increase the wing divergence speed four-fold.

6.5.3 Adaptive Control for Wing Tip Actuator

Adaptive control is a useful method when system dynamics and/or parameters are unknown. The elastic properties of a linearly elastic structure can be characterized experimentally. The aerodynamic force and moment distribution would be usually hard to characterize or if characterized at all, would show a considerably nonlinear spatial distribution. For example, a simple rectangular wing has an elliptic lift distribution under nominal flight conditions [48]. Nonlinearities would be considered in a later section of this chapter. Consider the case where M is constant, but unknown. This is not a very realistic model, but provides a sound foundation to design an adaptive controller.

Consider the dynamics in equation (6.64) with the objective in equation (6.65). The control

law in (6.67) is modified so that

$$b\dot{u}(t) + au(t) = \ddot{H}(t) - \hat{M}(t)(H(t) + e(t)) - ke(t) - k_c\dot{e}(t) + a\theta_y(0) + b\theta_{ty}(0) \quad (6.73)$$

where $\hat{M}(t)$ is the estimated value of M . The error dynamics are described by the ODE

$$\ddot{e}(t) + k_c\dot{e}(t) + ke(t) = -\tilde{M}(t)(H(t) + e(t)), \quad (6.74)$$

where $\tilde{M}(t) = \hat{M}(t) - M(t)$. An adaptive law must be designed for $\hat{M}(t)$ to ensure that the error, $e(t)$, remains bounded with as small a bound as possible.

For notational convenience, define $x = [e(t), \dot{e}(t)]^T$ and $A = \begin{bmatrix} 0 & 1 \\ -k & -k_c \end{bmatrix}$. Since A is Hurwitz, it follows that there exists a positive definite symmetric matrix $P = P^T > 0$ satisfying the Lyapunov equation

$$PA + A^T P = -\mathbb{I}, \quad (6.75)$$

where \mathbb{I} is the 2×2 identity matrix. We assume that $|M(t)|$ is bounded above by B_1 and $|\dot{M}(t)|$ by B_2 , where B_1 and B_2 are constants.

Consider the Lyapunov function

$$V(t) = x^T(t)Px(t) + \frac{1}{\gamma}\tilde{M}(t)^2, \quad (6.76)$$

where $\gamma > 0$ is the adaptive gain. Differentiating both sides with respect to t , we get

$$\dot{V}(t) = -x^T(t)x(t) + \frac{2}{\gamma}\tilde{M}(t)\left(\dot{\hat{M}}(t) - \gamma x^T P \begin{bmatrix} 0 \\ 1 \end{bmatrix} (e(t) + H) - \dot{M}(t)\right) \quad (6.77)$$

With the adaptive law

$$\dot{\hat{M}}(t) = \gamma \text{Proj} \left(\hat{M}(t), x^T P \begin{bmatrix} 0 \\ 1 \end{bmatrix} (e(t) + H) \right) \quad (6.78)$$

it follows that

$$\dot{V}(t) \leq -x^T(t)x(t) - \frac{2}{\gamma}\tilde{M}(t)\dot{M}(t) \leq \frac{-1}{\lambda_{\max}(P)} \left(x^T P x + \frac{1}{\gamma} \tilde{M}(t)^2 \right) + \frac{4B_1^2}{\gamma \lambda_{\max}(P)} + \frac{4B_1 B_2}{\gamma} \quad (6.79)$$

The projection law can be chosen so that $|\hat{M}(t)| < B_1$ (the same bound as that on $M(t)$). Therefore, it follows that

$$\dot{V}(t) \leq \frac{-1}{\lambda_{\max}(P)}(1 - \delta_b)V(t) \quad \forall \quad V(t) > \frac{4\lambda_{\max}(P)B_1B_2 + 4B_1^2}{\delta_b\gamma}, \quad \delta_b \in (0, 1) \quad (6.80)$$

and hence, the solution is uniformly ultimately bounded with some $T \geq 0$ and with the ultimate bound given by

$$\|x(t)\|_\infty \leq \|x(t)\|_2 \leq \sqrt{\frac{4\lambda_{\max}(P)B_1B_2 + 4B_1^2}{\lambda_{\min}(P)\delta_b\gamma}} \quad \forall t \geq T \quad (6.81)$$

where $\delta_b \in (0, 1)$. Note that the bound on $\|x(t)\|_\infty$ can be made arbitrarily small by choosing a large γ . The steady state beam shape of the wing depends on the steady state value of the error $\tilde{M}(t)$. Finally, it is worth noting that although a and b were assumed to be known, the aforementioned analysis can be repeated to accommodate an unknown a and b as well.

6.5.4 Control of Rolling Moment

An abstract measure of the rolling moment is $\int_0^L y\theta(t, y)dy$, defined in equation (6.6). Let $e_l(t, y) = \int_0^L y\theta(t, y)dy - H_l(t)$, where $H_l(t)$ denotes the reference value of the rolling moment to be tracked, and $e_l(t)$ is the tracking error. Differentiate $e_l(t)$ twice with respect to time:

$$\begin{aligned} \ddot{e}_l(t) &= \int_0^L y\theta_{tt}(t, y)dy - \ddot{H}_l(t) \\ &= \int_0^L y(b\theta_{tyy}(t, y) + a\theta_{yy}(t, y))dy + M \int_0^L y\theta(t, y)dy - \ddot{H}_l(t) \\ &= L(b\theta_{ty}(t, L) + a\theta_y(t, L)) - b(\theta_t(t, L) - \theta_t(t, 0)) - a(\theta(t, L) - \theta(t, 0)) + M e_l(t) + M H_l(t) - \ddot{H}_l(t) \end{aligned} \quad (6.82)$$

An interesting observation is that $e_l(t)$ has a relative degree of 2 with respect to $\theta_y(L)$ (tip control) as well as $\theta(0)$ (root control). In particular, it means that a considerably simpler controller than the backstepping controller, on the lines of the adaptive controller in the previous section, can be

implemented for a root-based actuator. Indeed, in aircraft, the lift is controlled using the horizontal tail, while wing-based flaps (ailerons and spoilers) are used primarily for roll control.

Finally, if $\theta(0)$ as well as $\theta_y(L)$ can be controlled, it may be possible to ensure that the wing deformation produces the desired net lift as well as moment. This control scheme is physically realizable in MAVs. For example, flapping wing MAVs such as the robotic bat described in Ref. [15] has a twist angle actuator at the root. A small flap at the wing tip, not unlike the outboard feathers in a bird wing, can provide twisting moment at the tip.

6.6 Root Boundary Control of Wing Bending

In this section, we will demonstrate conditions under which there is a significant time-scale separation between the bending and twisting dynamics, and which facilitate the design of independent control laws for bending and twisting dynamics. Time-scale separation is used quite routinely to design flight control laws [93, 105, 75, 32]. Thereafter, we will design a root controller for bending (δ_R in equation (6.3)) using a perturbation observer and motion planning. The design of a tip controller (F_{tip} in equation (6.2)) is straight-forward using the approach established in this section.

The bending PDE in equation (6.1) can be written as

$$\begin{aligned} \tilde{m}\xi_{tt} + \eta EI_b\xi_{tyyyyy} + EI_b\xi_{yyyyy} &= F_n(t, y, \xi_t, \theta, \theta_{tt}), \\ \xi(t, 0) = \xi_{yy}(t, L) = \xi_{yyy}(t, L) &= 0, \quad \xi_y(t, 0) = u(t), \end{aligned} \quad (6.83)$$

where the control input $u(t) = \delta_R(t)$ in Eq. (6.3) is designed to ensure that $\xi(t, L) = R(t)$ in (6.7). The acceleration term corresponding, $\tilde{m}x_e c \ddot{\theta}$ in equation (6.1) has been moved to the right hand side and merged into F_b , so that $F_n = F_b + \tilde{m}x_e c \ddot{\theta}$. The interesting point about equation (6.83) is that the right hand side is independent of ξ , and θ is an average value obtained from the faster twist dynamics. Therefore, unlike the twisting dynamics, the onset of instability in the bending dynamics will correspond to the damping becoming negative.

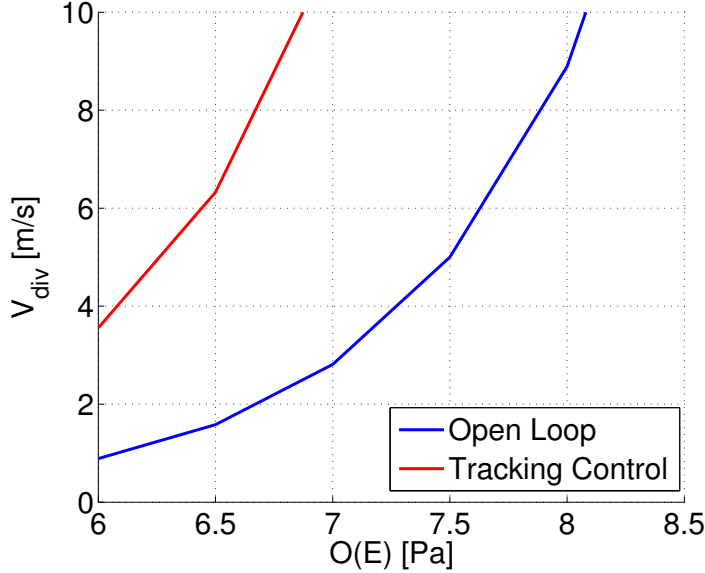


Figure 6.3: Torsional divergence speed as a function of the Young’s modulus of the wing. The blue curve is the open loop divergence speed, while the red curve is the divergence speed after adding the tip controller from section 6.5.

6.6.1 Time Scales of Wing Twist and Bending

The objective of this section is two-fold: (a) estimate the torsional divergence speed for an MAV wing as a function of its Young’s modulus, and (b) estimate the time scales of bending and twisting dynamics. In particular, we show that the time scale separation can be estimated using the geometry of the cross section, the Poisson’s ratio of the wing material, the aspect ratio of the wing and the flight speed.

As an illustration, consider the wing of an MAV whose dynamics are described by equations (6.83) and (6.8). The torsional divergence speed is found by solving for zero stiffness, i.e., by setting $M/a = \pi^2/(4L^2)$, where $a = G\tilde{J}/I_p$ and $M\theta = -x_a c F_b/I_p$, with F_b linear in θ and I_p is the mass moment of inertia of the wing cross section. Furthermore, $M \approx V^2 c^2/I_p$ (with x_a assumed to be 0.5). Thus, we get that the divergence speed can be approximated as

$$V_{\text{div}}^2 \sim \mathcal{O} \left(\frac{\pi^2}{4\Gamma} \frac{G}{\mathcal{A}_{0.5}} \frac{t_c^3}{c^3} \right) \approx \mathcal{O} (10^{-6} G), \quad (6.84)$$

where $\mathcal{A}_{0.5}$ is the aspect ratio of the semi-wing and $\Gamma \sim \mathcal{O}(10)$ is a function of the shape of the wing cross section. The divergence speed for a wing with an almost elliptical cross section has been

shown in figure 6.3. The blue line shows the open loop divergence speed, i.e., the divergence speed without a stabilizing or tracking controller, while the red curve shows the divergence speed when the tracking controller from section 6.5 is added. Therefore, MAVs wings should be designed with $E \approx 10^8$ (when $t_c/c = 0.01$) to avoid torsional divergence altogether. Since the divergence speed is proportional to $(t_c/c)^{1.5}$, doubling the wing thickness would increase the divergence speed by a factor of nearly 3.

We now estimate the time scale separation between twisting and bending dynamics. Consider a cantilever wing where $\theta(0) = \xi(0) = \xi_y(0) = 0$ and $\theta_y(L) = \xi_{yy}(L) = \xi_{yyy}(L) = 0$. If ω_θ and ω_ξ denote the frequencies of the first twisting and bending modes, respectively, then it can be shown that

$$\omega_\theta^2 = \frac{\pi^2}{4L^2} \frac{G\tilde{J}}{I_p} - \frac{M}{I_p}, \quad \omega_\xi^2 = \frac{12.36}{L^4} \frac{EI_b}{\tilde{m}} \quad (6.85)$$

In order to estimate the ratio $\omega_\theta^2/\omega_\xi^2$, the following estimates are required.

1. $I_p \sim \mathcal{O}(\tilde{m}A_c c^2)$, where A_c is the area of cross section of the wing and \tilde{m} is the density of the wing material per unit span.
2. $\tilde{J}/I_p \sim \mathcal{O}((t_c/c)^2)/\tilde{m}$. Thus, $G\tilde{J}/I_p \sim G(t_c/c)^2/\rho_w$.
3. $I_b \sim \mathcal{O}(A_c t_c^2)$, where t_c is wing thickness. Furthermore, $\tilde{m} = \rho_w A_c$. Thus, $EI_b/\tilde{m} \sim Et_c^2/\rho_w$.

From Eq. (6.85), it is clear that the time scale separation depends on the flight speed. It is of interest to determine the time scale separation in the absence of the M/I_p term, which is an upper bound on the time scale separation. It will closely approximate the actual time scale separation for larger values of stiffness, and would need to be scaled when the wing flexibility is increased. Ignoring the contribution from M/I_p , it follows that

$$\omega_\theta^2 \approx \frac{\pi^2}{4L^2} \frac{G\tilde{J}}{I_p} = \frac{\pi^2}{4L^2} \frac{G}{\rho_w} \frac{t^2}{c^2} \quad (6.86)$$

and

$$\omega_\xi^2 = \frac{12.36}{L^4} \frac{EI_b}{\tilde{m}} \approx \frac{12.36}{L^4} \frac{E}{\rho_w} \frac{t^2}{16} \quad (6.87)$$

where the scaling factor of 16 is obtained assuming a nearly elliptical cross section. Therefore, the ratio $\omega_\theta^2/\omega_\xi^2$ is given by

$$\frac{\omega_\theta^2}{\omega_\xi^2} \approx 3 \frac{G}{E} \frac{L^2}{c^2} \approx \frac{3}{2(1 + \nu_p)} \frac{L^2}{c^2} \quad (6.88)$$

where ν_p is Poisson's ratio. The ratio $1.5/(1 + \nu_p) \approx 1$. Thus, $\frac{\omega_\theta}{\omega_\xi} \approx \mathcal{O}(L/c)$ (the aspect ratio of the wing). Therefore, the twist dynamics are faster than the bending dynamics. The time scale separation reduces with decreasing E and increasing V , as the influence of the aerodynamic terms increasingly dominates the contribution from elasticity. The time scale separation increases with increasing aspect ratio. Although this time scale separation cannot be used to draw any inference about the susceptibility of the wing to flutter, it can be used as the basis for designing independent controllers for controlling wing bending and torsion. Time scale separation is used quite commonly in flight control design in a similar fashion [93, 105, 75, 32]. Incidentally, equation (6.88) suggests that significant time scale separation is to be expected in slow aircraft with large aspect ratio wings, such as gliders and high altitude, long endurance aircraft like the NASA HALE [73, 74].

6.6.2 Open Loop Stability of Bending

Assume that the boundary conditions are homogeneous, i.e., $\xi(0) = \xi_y(0) = \xi_{yy}(L) = \xi_{yyy}(L) = 0$. Let $a_b = EI_b/\tilde{m}$ and $b_b = \eta a_b$. Let $F(t, y) = F_n(t, y)/\tilde{m}$, where $F_n(t, y)$ succinctly denotes the RHS of equation (6.83). Assume that the flight speed, V_∞ , is constant. Consider the Lyapunov function (in this case, the total energy of the beam),

$$V(t) \triangleq V(t, y) = \frac{1}{2} \int_0^L (\xi_t^2 + a_b \xi_{yy}^2) dy \quad (6.89)$$

It is quite straight forward to derive the following expressions for $\dot{V}(t)$:

$$\dot{V}(t) = -b_b \int_0^L \xi_{tyy}^2 dy + \int_0^L \xi_t F(t, y) \quad (6.90)$$

By applying Poincaré's inequality[†] successively, it follows that

$$\dot{V}(t) \leq -\frac{b_b \pi^4}{16L^4} \int_0^L \xi_t^2 dy + \int_0^L \xi_t F(t, y) \quad (6.91)$$

Clearly, if

$$F(t, y) < \frac{b_b \pi^4}{16L^4} \xi_t, \quad (6.92)$$

then the bending dynamics are stable. This equation actually offers a lot of insight. First, note that expression for $F(t, y)$ in the simplest case is of the form $F(t, y) = -(\kappa_1 \xi_t + \kappa_2 \xi_t^2) C_L(\theta)$, where $\kappa_1, \kappa_2 > 0$ are essentially constant. If $C_L > 0$ (a reasonable assumption), it follows that $\kappa_1 C_L \xi_t$ injects damping into the system and counters the potentially destabilizing contribution from $\kappa_2 \xi_t^2 \theta$ for sufficiently small values of ξ_t . However, if $C_L(\theta)$ is not uniformly positive, and if it is out-of-phase with ξ_t , $F(t, y)$ could potentially cause the damping to become negative, leading to an oscillatory instability in the bending dynamics and trigger wing flutter. This simple analysis explains a possible mechanism for the onset of flutter, and (6.92) is a sufficient condition to prevent an instability.

Second, note that $\kappa_1 \propto V_\infty$, where $V_\infty = \|\mathbf{u}_B\|$ is the flight speed, and $b_b \propto E$, the Young's modulus. Therefore, (6.92) can be used to derive a stable envelope for the flight speed and Young's modulus. However, unlike the analysis for wing twist in Section 6.6.1, the analysis is considerably more complicated because of the potentially strong nonlinear contribution from ξ_t^2 at low flight speeds.

6.6.3 Perturbation Observer for Root Control of Bending

If the beam dynamics are unstable, in a manner described above, PDE backstepping can be used to inject damping into the system. A procedure for backstepping, based on a transformation of the bending dynamics into the Schrödinger equation, has been detailed in Krstic and Smyshlyaev (See Ch. 8 of Ref. [40]). As we showed in Section 6.4, a tracking controller can be added on top of the backstepping controller for tracking. We focus on a motion planning-based design for a tracking controller. However, note that $F(t, y)$ is usually not measurable in practice, although one may

[†]Poincaré's inequality: $\int_0^L w^2 dx \leq L w^2(0) + \frac{4L^2}{\pi^2} \int_0^L w_x^2 dx$

estimate its spatial profile from the wing geometry [48].

In this section, we design an observer-based controller to facilitate a motion-planning-based tracking controller for bending. The perturbation observer does not predict the system states. It uses projection-based adaptation to estimate $F(t, y)$ which would be unknown in practical situations. The perturbation observer is split into a “particular” and a “homogeneous” component (the notions will be made more precise in this section). In particular, the homogeneous component is stable and not driven directly by external feedback. Thus, it is simpler to design a control law for it. The same control signal is sent to the actual system, whose states then converge exponentially to a bounded envelope around the observer states.

Let $F(t, y) = W(t)^T \phi_b(y) + \sigma(t)$ where $W(t)$ and $\sigma(t)$ are unknown and bounded with known bounds. The set of functions, $\phi_b(y)$, can be chosen to get a satisfactory bound on σ , and using a knowledge of the wing geometry [48] (e.g., the force distribution on an elliptical wing is rectangular, and vice-versa). A candidate for ϕ_b is $1 - (y/L)^2$, which approximates a sinusoidal force distribution with zero force at the wing tip. Consider the perturbation observer for the bending dynamics in (6.83)

$$\begin{aligned} \hat{\xi}_{tt}(t, y) + b_b \hat{\xi}_{tyyy}(t, y) + a_b \hat{\xi}_{yyy}(t, y) &= \hat{W}(t)^T \phi_b(y) + \hat{\sigma}(t) - b_b p \tilde{\xi}_t(t, y) - a_b p \tilde{\xi}(t, y) \\ \hat{\xi}_{yy}(t, L) = \hat{\xi}_{yyy}(t, L) &= \hat{\xi}(t, 0) = 0, \quad \hat{\xi}_y(t, 0) = u(t), \end{aligned} \quad (6.93)$$

where $\tilde{\xi} = \hat{\xi} - \xi$ and $p > 0$ is chosen to ensure desirable convergence properties. Figure 6.4 is a block diagram of the perturbation observer. Notice that the reference input, $R(t)$ from (6.7), enters only the homogeneous component of the perturbation observer, while the feedback from the actual system only enters the particular component.

Consider the Lyapunov function

$$V(t) = \frac{1}{2} \int_0^L \left(\tilde{\xi}_t^2 + a_b(1 + \delta p) \tilde{\xi}_{yy}^2 + (a_b p + \delta b_b p) \tilde{\xi}^2 \right) dy + \frac{1}{\gamma_a} \left(\tilde{W}^T \tilde{W} + \tilde{\sigma}^2 \right) + \delta \int_0^L \tilde{\xi} \tilde{\xi}_t dy \quad (6.94)$$

The constant δ is chosen to be small enough so that the Lyapunov function is positive definite, while $\gamma_a > 0$ is the adaptation rate.

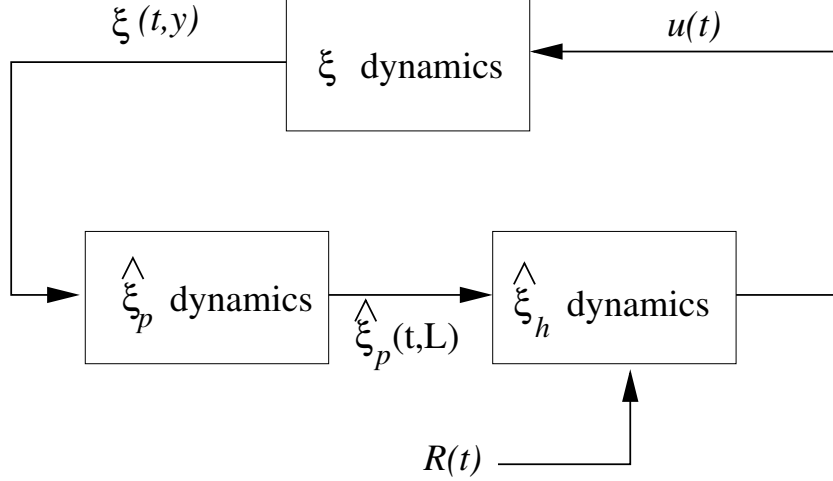


Figure 6.4: Block diagram for the perturbation observer coupled to the system dynamics. The control signal, $u(t)$, is generated from motion planning, while $R(t)$ is the desired reference signal from (6.7).

Choose a projection-based adaptive law for $\hat{W}(t)$ and $\hat{\sigma}(t)$:

$$\begin{aligned}\dot{\hat{W}}(t) &= \gamma_a \text{Proj} \left(\hat{W}(t), - \int_0^L (\tilde{\xi}_t + \delta\tilde{\xi}) \phi_b(y) dy \right) \\ \dot{\hat{\sigma}}(t) &= \gamma_a \text{Proj} \left(\hat{\sigma}(t), - \int_0^L (\tilde{\xi}_t + \delta\tilde{\xi}) dy \right)\end{aligned}\quad (6.95)$$

Differentiating both sides with respect to time and performing integration by parts a few times, it can be verified that

$$\begin{aligned}\dot{V}(t) \leq & -b_b(p - \delta) \int_0^L \tilde{\xi}_t^2 dy - \delta a_b p \int_0^L \tilde{\xi}^2 dy - \delta a_b \int_0^L \tilde{\xi}_{yy}^2 dy - b_b \int_0^L \tilde{\xi}_{tyy}^2 dy - \int_0^L (\tilde{\xi}_t + \delta\tilde{\xi})(F(t, y)) dy \\ & - \frac{1}{\gamma_a} \left(\tilde{W}(t)^T \dot{W}(t) + \tilde{\sigma}(t) \dot{\sigma}(t) \right)\end{aligned}\quad (6.96)$$

It follows that the error dynamics between the perturbation observer and the actual system are stable, and in fact, globally uniformly bounded. The bound can be calculated using the method employed in Section 6.3.5 In particular, the error bound depends on the bounds on $\dot{W}(t)$, $\dot{\sigma}(t)$ and $F(t, y)$.

The perturbation observer can be designed as a sum of two states, $\hat{\xi} = \hat{\xi}_h + \hat{\xi}_p$, where the

dynamics of the two states $\hat{\xi}_h$ and $\hat{\xi}_p$ are described by the following PDEs:

$$\begin{aligned}\hat{\xi}_{p,tt}(t, y) + b_b \hat{\xi}_{p,tyyy}(t, y) + a_b \hat{\xi}_{p,yyyy}(t, y) &= -b_b p \tilde{\xi}_{p,t}(t, y) - a_b p \tilde{\xi}_p(t, y) + \hat{W}(t)^T \phi_b(y) + \hat{\sigma}(t), \\ \hat{\xi}_{p,yy}(L) = \hat{\xi}_{p,yyy}(L) = \hat{\xi}_p(0) = \hat{\xi}_{p,y}(0) &= 0\end{aligned}\quad (6.97)$$

for the particular component, where $\tilde{\xi}_p = \hat{\xi}_p - \xi$, and

$$\begin{aligned}\hat{\xi}_{h,tt} + b_b \hat{\xi}_{h,tyyy} + a_b \hat{\xi}_{h,yyyy} &= -b_b p \hat{\xi}_{h,t} - a_b p \hat{\xi}_h, \\ \hat{\xi}_{h,yy}(L) = \hat{\xi}_{h,yyy}(L) = \hat{\xi}_h(0) = 0, \quad \hat{\xi}_{h,y}(0) &= u(t)\end{aligned}\quad (6.98)$$

for the homogeneous component. This observer can be used in the motion planning algorithm to ensure that the wing tip tracks the desired displacement profile. Note that the homogeneous half is a stable system and its dynamics are not influenced in any way by ξ or $\hat{\xi}_p$.

Recall that the output of interest is $\int_0^L \xi_y(t, y) dy = \xi(t, L)$, from (6.7), which represents the integrated value of the wing dihedral which, in turn, is a measure of the side force produced by the wing. In order to ensure that this output tracks the desired reference signal, $R(t)$, the control signal, $u(t)$ (also $= \hat{\xi}_{h,y}(t, 0)$) is designed using motion planning to ensure that $\hat{\xi}_h(t, L)$ tracks $R(t) - \hat{\xi}_p(t, L)$.

Remark: The observer-based approach presented here can be used for a wide class of functions $F(t, y)$ which, as we argued earlier, are usually nonlinear in ξ_y . Therefore, it is difficult to construct a polynomial expansion for $F(t, y)$. Although the motion planning involves a polynomial expansion, the use of a two stage perturbation observer allows us to do away with the need to obtain a polynomial expansion for $F(t, y)$.

The error between the perturbation observer and the system is uniformly bounded, and the bound can be made arbitrarily small by increasing γ_a . The gain γ_a does not enter the control signal itself, which is constructed using an essentially open loop process, and therefore, there is no risk of introducing stability and noise issues related to the use of high gain.

Remark: The limitations of using a perturbation observer need to be stated although these can be occasionally circumvented effectively. First, it requires a knowledge of $\xi(t)$. However, $\xi(t)$ can

be obtained using an array of sensors and spline-fitting. Second, the approach does not actually stabilize the bending dynamics beyond the improvement that comes from imposing a clamp-like boundary condition at both ends. Note, however, that effectively adding a clamp at the free end results in a substantial improvement in the stability margin (in practice, measured by the extent to which the material stiffness can be reduced or by the increase in the critical flight speed) of the closed-loop system. Finally, the use of an observer in the current form requires that we know a_b and b_b . However, they can be obtained reliably from experiments.

6.6.4 Motion Planning for the Homogeneous Component of the Observer ($\hat{\xi}_h$)

For a reference signal $R(t)$ from (6.7), let us define $R_h(t) = R(t) - \hat{\xi}_p(t, L)$ denote the reference signal that has to be tracked by $\hat{\xi}_h(t, L)$. We use a motion-planning approach, as we did for wing twist.

The term $\hat{\xi}_h(t, y)$ can be approximated by a polynomial of the form

$$\hat{\xi}_h(t, y) = \sum_{j=1}^N \frac{\eta_j(t)y^j}{j!} \quad (6.99)$$

where N needs to be chosen to ensure desirable tracking properties. Note that the coefficient of y^0 is zero because $\hat{\xi}(t, 0) = 0$.

Substituting (6.99) into the $\hat{\xi}_h$ dynamics in (6.98) yields the set of ODEs

$$\ddot{\eta}_j + b_b p \dot{\eta}_j + a_b p \eta_j = -b_b \dot{\eta}_{j+4} - a_b \eta_{j+4} \quad (6.100)$$

The boundary conditions, together with $\xi_h(L) = R_h(t)$, yield the following algebraic equations:

$$\sum_{j=0}^{N-2} \frac{\eta_{j+2}(t)}{j!} = 0, \quad \sum_{j=0}^{N-3} \frac{\eta_{j+3}(t)}{j!} = 0, \quad \sum_{j=1}^N \frac{\eta_j(t)L^j}{j!} = R_h(t) \quad (6.101)$$

The value of N can be chosen to ensure good tracking. Note that the $\hat{\xi}_h$ dynamics are fourth order in y . Therefore, we need to choose $N > 5$, and the gain p must be chosen to ensure stability of the resulting set of ODEs. An interesting point must be noted. For any choice of N , we have $N - 4$ differential equations (for η_1 to η_{N-4}) and 3 constraints, a total of $N - 1$ equations. This

problem may be resolved by setting one variable among η_{N-3} , η_{N-2} and η_{N-1} to zero, or imposing an additional constraint on the system.

Let us choose $N = 5$, i.e., $\eta_6 = \eta_7 = \dots = 0$. We will set $\eta_4(t) = 0$ [‡] This yields the differential equation

$$\ddot{\eta}_1(t) + b_b p \dot{\eta}_1(t) + a_b p \eta_1(t) + b_b \dot{\eta}_5(t) + a_b \eta_5(t) = 0. \quad (6.102)$$

The constraint (6.101) can be solved to obtain $\eta_1(t)$ in terms of $\eta_5(t)$ and $R_h(t)$. From Eq. (6.99), it follows that the control input is given by

$$u(t) = \hat{\xi}_{h,y}(t, 0) = \eta_1(t) = -\frac{\eta_5(t)L^4}{12} + \frac{R_h(t)}{L} \quad (6.103)$$

where, from (6.102), it follows that $\eta_5(t)$ satisfies the following differential equation:

$$\ddot{\eta}_5(t) + b_b \left(p - \frac{12}{L^4} \right) \dot{\eta}_5(t) + a_b \left(p - \frac{12}{L^4} \right) \eta_5(t) = \left(\frac{12}{L^5} \right) (\ddot{R}_h(t) + b_b p \dot{R}_h(t) + a_b p R_h(t)) \quad (6.104)$$

Note that the gain p has to be chosen so that $p > 12/L^4$ for $\eta_5(t)$ to be stable. This completes the design of a motion planning-based tracking controller for bending.

6.7 Simulations

Simulations are carried out in Matlab using a Galerkin-based approach to convert the PDE system into ODEs. The Galerkin truncation is not used as a basis for control law design, so no danger of a “spillover instability” arises. The twist $\theta(t, y)$ is expressed as a weighted sum of basis functions $\phi_i(y)$, $i = 1, 2, \dots, n$ and $\psi(y)$:

$$\theta(t, y) = s(t)\psi(y) + \sum_{i=1}^n \eta_i(t)\phi_i(y), \quad \phi_i(0) = \phi'_i(L) = 0, \quad (6.105)$$

where $s(t)$ is the boundary control input. If boundary control is applied at the wing root, then $\psi(y)$ has to be chosen to satisfy $\psi'(L) = 0$ and $\psi(0) = 1$. On the other hand, if the boundary control is applied at the wing tip, we choose ψ to satisfy $\psi(0) = 0$ and $\psi'(L) = 1$.

[‡]Motivation: if R_h is a constant, then $\eta_4 = 0$ in the steady state solution. Therefore, this approximation will work at least for a class of slowly varying time signals.

The PDE in equation (6.64) can be rewritten as

$$\begin{aligned} \psi(y)\ddot{s}(t) + \sum_{i=1}^n \ddot{\eta}_i(t)\phi_i(y) - \sum_{i=1}^n \phi_i''(y)(b\dot{\eta}_i(t) + a\eta_i(t)) - \psi''(y)(b\dot{s} + as) \\ = M \left(\psi(y)s + \sum_{i=1}^n \eta_i(t)\phi_i(y) \right) \end{aligned} \quad (6.106)$$

Using Galerkin's method, equation (6.106) is converted to a set of ODEs:

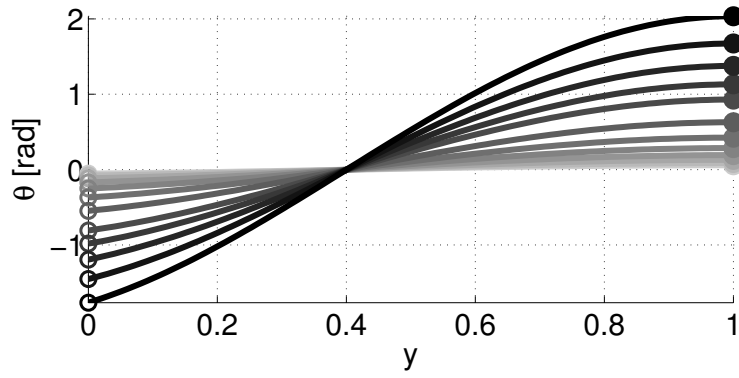
$$\mathbf{c}(\ddot{s}(t) - Ms(t)) + \mathbf{d}(b\dot{s} + as(t)) + [A](\ddot{\eta}(t) - M\eta(t)) + [B](b\dot{\eta}(t) + a\eta(t)) = 0 \quad (6.107)$$

where

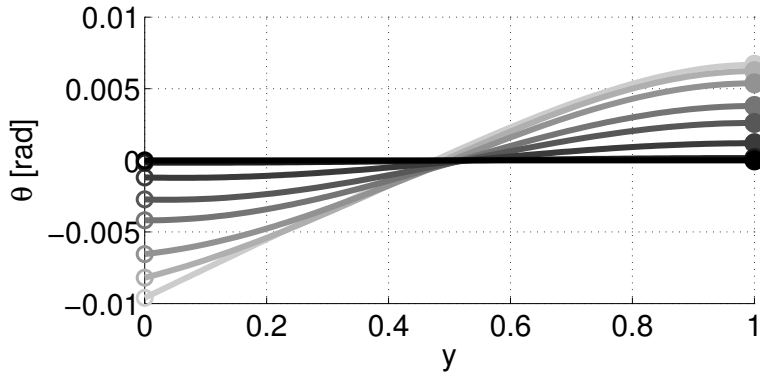
$$\begin{aligned} \mathbf{c} &= \int_0^L \psi(y)\phi(y), \quad \mathbf{d} = - \int_0^L \psi''(y)\phi(y), \\ [A] &= \int_0^L \phi\phi^T dy, \quad [B] = - \int_0^L \phi(\phi'')^T dy \end{aligned} \quad (6.108)$$

The reader will recall that ψ is a scalar, and $\phi = [\phi_1 \ \phi_2 \ \dots \ \phi_n]^T$ is a vector. The control $s(t)$ is expressed similarly in terms of ϕ , ψ and η to obtain a set of ODEs which are simulated to approximate the response of a twisting beam with boundary control. Figure 6.5 demonstrates the regulation of twist dynamics using the backstepping controller derived in equation (6.18), with the transformation in equations (6.15) and (6.17). The value of M/a was set to 8, where $a = G\tilde{J}/I_p$. A value of $p = 4$ yielded an unstable response, while the response was stable for $p = 8$. Recall the following condition for stability with $L = 1$: $p > M/a - \pi^2/4 \approx 2.53$. The backstepping controller works even when $M(y) = M(1 - y^2)$ is used (to mimic an elliptical lift distribution over the wing) instead of a constant $M(y) \equiv M$. The backstepping controller can be added on top of a tracking controller.

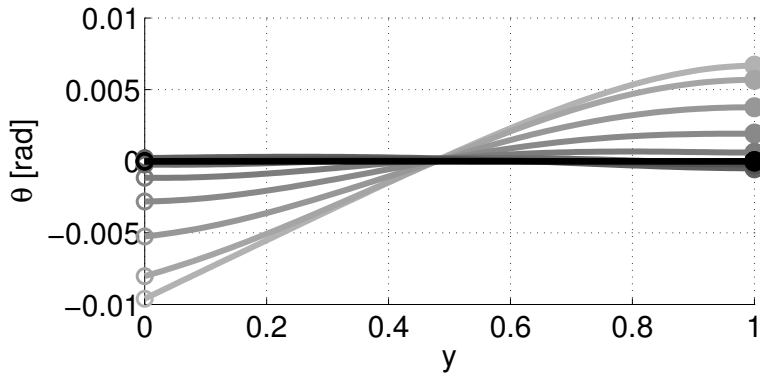
Figure 6.6 shows the simulation of a wing actuated by tip control. The value of M/a was chosen so that stability is assured without the need for a dedicated stabilizing controller. The first plot was obtained for a for a system where the aerodynamics were assumed to be linear but unknown. The second plot assumed linear unknown aerodynamics, such that the system was unstable in the open loop, but within the enhanced stability margin described in Section 6.5.2.. The third plot



(a) Unstable response with $p = 4$



(b) Stable response with $p = 8$



(c) Stable response with $p = 8$ for spatially-varying $M(y)$

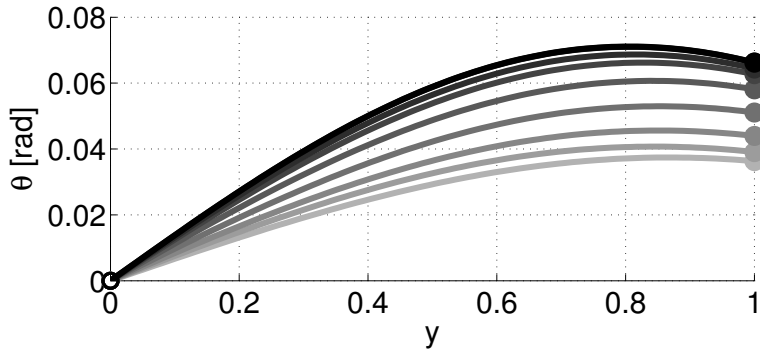
Figure 6.5: Regulation of the twist dynamics using the backstepping controller in equation (6.18), with the transformation in equations (6.15) and (6.17). The plots were obtained for $M/a = 8$, while p was increased to ensure stability. Each plot is a collection of snapshots, where the lines get darker with time.

was obtained for the case where the aerodynamics were additionally spatially varying. The time histories of the tracking error $e(t)$, and the control signal $u(t)$, for the third case are plotted in Fig. 6.7. In all three cases, the twist amplitude converges to the steady state value with satisfactory transients. The error metric equation (6.5) is also seen to be very small. Note that the control signal, obtained from Eq. (6.73), is almost noise-free. This is because the dynamic controller acts like a low pass filter and ensures that noisy terms arising from the high gain terms on the right hand side of Eq. (6.73) are filtered out.

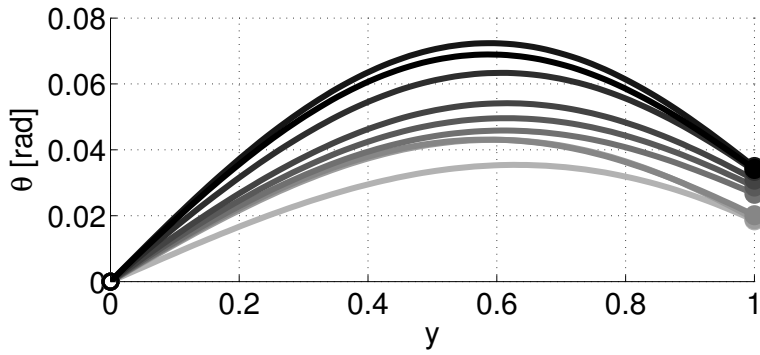
Finally, figure fig:BendSims shows the time histories tip displacement for a wing whose bending motion is actuated by a root-based actuator. The dashed lines show the reference signal for wing tip displacement, while blue lines show the actual displacement of the wing tip. The first two simulations were obtained for the case where $F(t, y)$ was set to zero, while the third plot was obtained for a time varying $F(t, y)$. The motion planning algorithm used a seventh order polynomial in the spatial variable y (see equation (6.99)). In all three cases, the tracking is seen to be satisfactory and noise free.

6.8 Chapter Summary

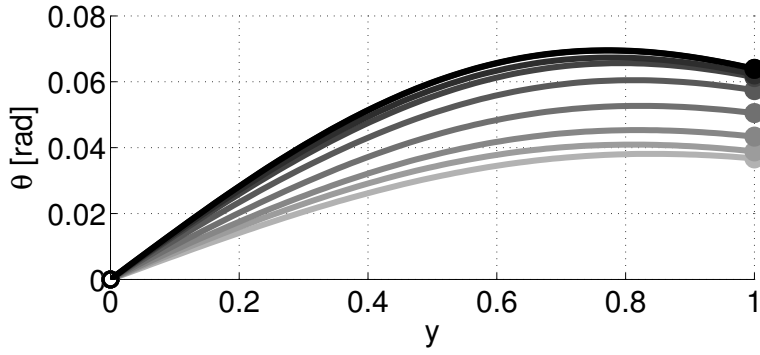
Tools from PDE boundary control show considerable promise for the efficient control of flexible structures in general, and of flexible wings in particular. The key contributions of this chapter were: (a) the design of a PDE backstepping based tracking controller for wing twist, (b) the finite degree problem formulation for wing twist control using a tip-based actuator, (c) the study of the enhancement in stability due to a tracking controller, and (d) the design of a perturbation observer based controller for wing bending. It is safe to claim that every contribution listed above leads to a related open problem in PDE control. The most important open problem is the design of a coupled twist-bending controller.



(a) M unknown, constant, open loop stable

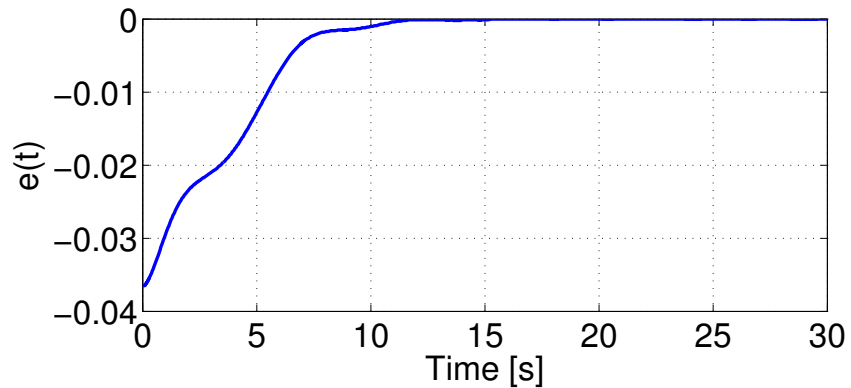


(b) Unknown M , constant, open loop unstable

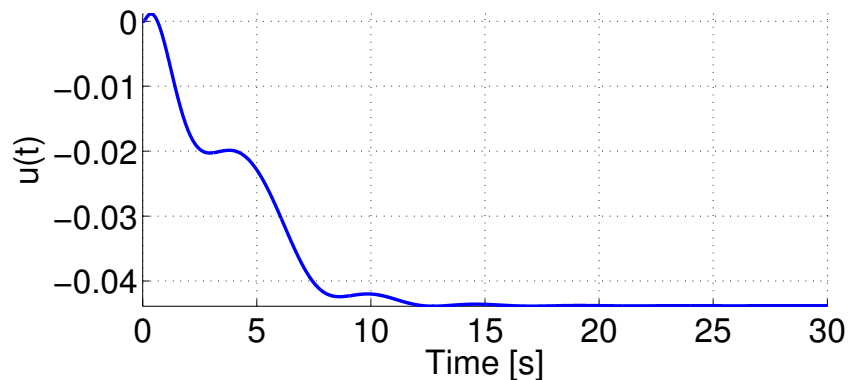


(c) Spatially varying, unknown $M(y)$, unstable dynamics

Figure 6.6: Twist profile of the wing as a function of time when the adaptive controller in equation (6.73) is applied at the wing tip. Three cases have been examined here, with $\int_0^L \theta(t, y) dy = 0.05$ as the desired output. Each plot shows appropriately chosen snapshots, with lines getting darker with time.



(a) Time history of $e(t)$



(b) Time history of $u(t)$

Figure 6.7: Time histories of the error $e(t)$ and the control signal $u(t)$ for the case of spatially varying, unknown $M(y)$ with unstable open loop dynamics.

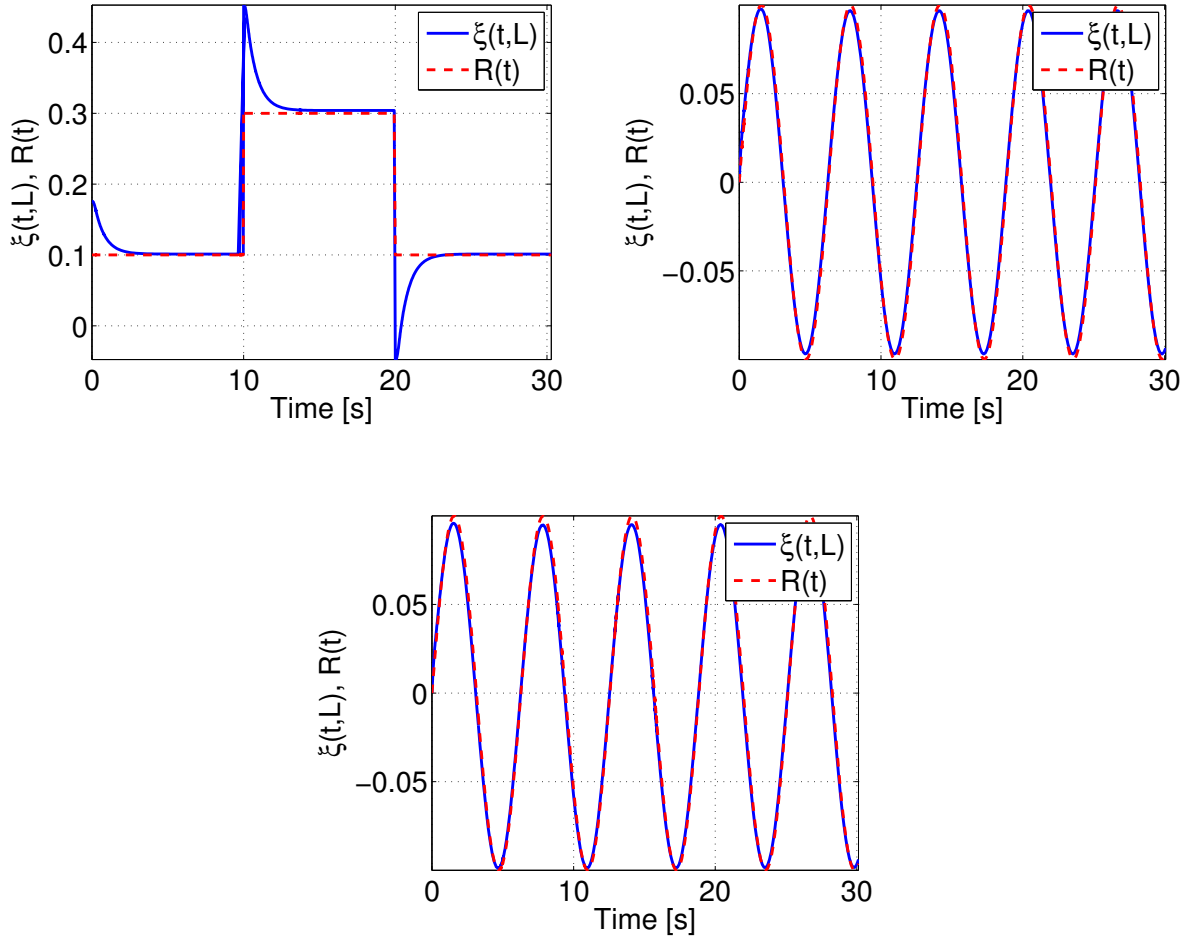


Figure 6.8: Time history of the wing tip displacement for two classes of reference signals: a pulse and a sine wave. The first two plots were obtained with the right hand side set to zero, while the third plot was obtained for a time varying $F(t, y)$ in equation (6.83).

Chapter 7

Conclusions and Open Problems

7.1 Conclusions

The objective of this thesis was to study the unique dynamics and control characteristics of tailless MAV equipped with articulated wings. We studied the performance and stability using a combination of literal approximations, numerical trim and stability computations, and experiments. We showed that the dihedral angle of the wing can be varied symmetrically to obtain an additional degree of freedom, namely the ability to change flight path angle independently of the flight speed. We demonstrated that asymmetric dihedral settings can be used to perform rapid turns and control the sideslip. From the standpoint of control, the most important observation was the discovery of maneuver-dependent control effectiveness reversal.

The performance and stability characteristics of a flexible aircraft were compared with those of a rigid aircraft, assuming that the wings of the flexible aircraft were statically deformed. We presented a metric called the effective dihedral for flexible wings which allows the results from the analysis of a rigid aircraft to be extended to flexible aircraft. Moreover, it allows us to identify the extent to which conclusions regarding the performance of rigid aircraft apply to a flexible-winged aircraft. Although we did not observe any difference in stability characteristics, there were interesting differences in the turn performance. Although wing flexibility was shown to help reduce the sideslip significantly, it was also shown to reduce the maximum attainable turn rate under a zero-sideslip constraint compared to a rigid aircraft with identical elevator settings. This was attributed to the reduction in flight speed due to wing twist.

The open loop characteristics of a tailless MAV were tested experimentally to verify the analytical predictions. Control laws motivated by dynamic inversion were designed and tested on an experimental aircraft. The experiments exposed the impediments that arise due to the reversal of

control effectiveness. At the same time, they demonstrated the ability of articulated wings to aid steep descents and perching maneuvers, as well as their capability for yaw control.

Finally, we designed PDE-based control laws for controlling the deformation of a flexible wing to achieve a net aerodynamic force or moment. We considered cases where the actuators were based at the wing root as well as the tip. PDE backstepping-based control laws were developed for controlling wing twist using root-based actuators. We showed that a tracking controller could bring about a significant improvement in the stability margin of the wing dynamics, measured by the critical flight speed or elastic modulus for the onset of instability. We showed that the time scale separation between the bending and twisting dynamics depends primarily on the aspect ratio of the wing and the flight speed. We designed a controller for bending independently of the one for wing twist. The controller designed for bending used a novel idea based on splitting a perturbation-observer into two parts, one of which accommodated the external forces and the other which accommodated the boundary control. Thereafter, motion planning was used to design the boundary controller, with the understanding that it could be added readily on top of a stabilizing controller if required.

7.2 Future Work

Although we have proved the feasibility of dihedral-based control for articulated wing MAVs, more research is needed before this scheme can be implemented on a “field-ready” aircraft.

- The problem of control reversal is the most important impediment. It needs to be addressed theoretically - using a modification of Nussbaum gain or supervisory control techniques, although we have presented a trailing edge flap-based solution to this problem.
- We designed independent controllers for wing twist and bending, and these can be used directly in cases where the time scale separation between the twisting and bending dynamics is sufficient. Time scale separation may not be present if extremely thin wings are designed using highly flexible material. The controllers designed in this thesis may need to be adapted for that case.

References

- [1] N. Ananthkrishnan and S. Unnikrishnan, “Literal approximations to aircraft dynamic modes,” *Journal of Guidance, Control and Dynamics*, vol. 24, no. 6, pp. 1196 – 1203, 2001.
- [2] A. Azuma, *The Biokinetics of Flying and Swimming*, 2nd ed. American Institute of Aeronautics and Astronautics, 2006.
- [3] N. Baghdadi, M. H. Lowenberg, and A. T. Isikveren, “Analysis of flexible aircraft dynamics using bifurcation methods,” *Journal of Guidance, Control and Dynamics*, vol. 34, no. 3, pp. 795 – 809, 2011.
- [4] M. J. Balas, “Feedback control of flexible systems,” *IEEE Transactions on Automatic Control*, vol. 23, no. 4, pp. 673 – 679, 1978.
- [5] S. Bieniawski and I. M. Kroo, “Flutter suppression using micro-trailing edge effectors,” in *44th AIAA/ASME/ASCE/AHS Structures, Structural Dynamics, and Materials Conference*, 2003, AIAA 2003–1941.
- [6] R. L. Bisplinghoff, A. Holt, and R. L. Halfman, *Aeroelasticity*, 1st ed. Dover, Mineola, NY, 1996.
- [7] M. A. Bolender, “Rigid multi-body equations-of-motion for flapping wing mavs using Kanes equations,” in *Proc. AIAA Guidance, Navigation and Control Conference, Chicago, IL*, 2009, AIAA Paper 2009–6158.
- [8] D. Borglund and J. Kuttenkeuler, “Active wing flutter suppression using a trailing edge flap,” *Journal of Fluids and Structures*, vol. 16, no. 3, pp. 271 – 294, 2002.
- [9] P. Bourdin, A. Gatto, and M. Friswell, “Aircraft control via variable cant-angle winglets,” *Journal of Aircraft*, vol. 45, no. 2, pp. 414 – 423, 2008.
- [10] F. Bucci and I. Lasiecka, “Optimal boundary control with critical penalization for a PDE model of fluid-solid interactions,” *Calculus of Variations*, vol. 37, pp. 217 – 235, 2009.
- [11] A. Chakravarthy, A. A. Paranjape, and S.-J. Chung, “Control law design for perching an agile mav with articulated wings,” in *Proc. AIAA Atmospheric Flight Mechanics Conference, Toronto, ON, Canada*, 2010, AIAA Paper 2010–7934.
- [12] A. Cheng and K. Morris, “Well-posedness of boundary control systems,” *SIAM Journal of Control and Optimization*, vol. 42, no. 4, pp. 1244 – 1265, 2003.
- [13] P. D. Christofides and P. Daoutidis, “Feedback control of hyperbolic PDE systems,” *AIChE Journal*, vol. 42, no. 11, pp. 3063–3086, 1996.

- [14] ——, “Finite-dimensional control of parabolic PDE systems using approximate inertial manifolds,” in *Proceedings of the 36th IEEE Conference on Decision and Control*, 1997, pp. 1068–1073.
- [15] S.-J. Chung and M. Dorothy, “Neurobiologically inspired control of engineered flapping flight,” *Journal of Guidance, Control and Dynamics*, vol. 33, no. 2, pp. 440–453, 2010.
- [16] R. Cory and R. Tedrake, “Experiments in fixed-wing UAV perching,” in *Proc. AIAA Guidance, Navigation and Control Conference, Honolulu, HI*, 2008, AIAA Paper 2008–7256.
- [17] W. J. Crowther, “Perched landing and takeoff for fixed wing UAVs,” Tech. Rep., 2000.
- [18] R. F. Curtain and H. J. Zwart, *An Introduction to Infinite-Dimensional Linear Systems Theory*, ser. Texts in Applied Mathematics. Springer-Verlag, 1995, no. 21.
- [19] J. D. DeLaurier, “An aerodynamic model for flapping-wing flight,” *Aeronautical Journal*, vol. 97, no. 964, pp. 125 – 130, 1993.
- [20] X. Deng, L. Schenato, and S. S. Sastry, “Flapping flight for biomimetic robotic insects: Part II: Flight control design,” *IEEE Transactions on Robotics*, vol. 22, no. 4, pp. 789 – 803, 2006.
- [21] X. Deng, L. Schenato, W. C. Wu, and S. S. Sastry, “Flapping flight for biomimetic robotic insects: Part I-system modeling,” *IEEE Transactions on Robotics*, vol. 22, no. 4, pp. 776 – 788, 2006.
- [22] D. B. Doman, M. Oppenheimer, and D. Sigthorsson, “Wingbeat shape modulation for flapping-wing micro-air-vehicle control during hover,” *Journal of Guidance, Control and Dynamics*, vol. 33, no. 3, pp. 724 – 739, 2010.
- [23] D. B. Doman, C. P. Tang, and S. Regisford, “Modeling interactions between flexible flapping-wing spars, mechanisms, and drive motors,” *Journal of Guidance, Control and Dynamics*, vol. 34, no. 5, pp. 1457 – 1473, 2011.
- [24] M. Dorothy, A. A. Paranjape, P. D. Kuang, and S.-J. Chung, *Towards Bio-inspired Robotic Aircraft: CPG-based Control of Autonomous Flapping and Gliding Flight*, ser. AIAA Progress in Aeronautics and Astronautics. American Institute of Aeronautics and Astronautics (AIAA), Reston, VA, to be published Spring 2012.
- [25] M. P. Fard and S. I. Sagatun, “Exponential stabilization of a transversely vibrating beam by boundary control via Lyapunov’s direct method,” *Journal of Dynamic Systems, Measurement, and Control*, vol. 123, pp. 195 – 200, 2001.
- [26] A. Gatto, P. Bourdin, and M. Friswell, “Experimental investigation into articulated winglet effects on flying wing surface pressure aerodynamics,” *Journal of Aircraft*, vol. 47, no. 5, pp. 1811 – 1816, 2010.
- [27] M. Goman and A. Khrabrov, “State-space representation of aerodynamic characteristics of an aircraft at high angles of attack,” *Journal of Aircraft*, vol. 31, no. 5, pp. 1109 – 1115, 1994.
- [28] M. G. Goman, G. I. Zagaynov, and A. V. Khramtsovsky, “Application of bifurcation theory to non-linear flight dynamics problems,” *Progress in Aerospace Sciences*, vol. 33, no. 9, pp. 539 – 586, 1997.

- [29] M. Hamamoto, Y. Ohta, K. Hara, and T. Hisada, “A fundamental study of wing actuation for a 6-in-wingspan flapping microaerial vehicle,” *IEEE Transactions on Robotics*, vol. 26, no. 2, pp. 244 – 255, 2010.
- [30] W. He, S. S. Ge, B. V. E. How, Y. S. Choo, and K. S. Hong, “Robust adaptive boundary control of a flexible marine riser with vessel dynamics,” *Automatica*, vol. 47, pp. 722 – 732, 2011.
- [31] D. H. Hodges and A. G. Pierce, *Introduction to Structural Dynamics and Aeroelasticity*, ser. Cambridge Aerospace Series. Cambridge University Press, 2002, no. 15.
- [32] N. Hovakimyan, E. Lavretsky, and A. Sasane, “Dynamic inversion for nonaffine-in-control systems via time-scale separation. Part I,” *Journal of Dynamical and Control Systems*, vol. 13, no. 4, pp. 451 – 465, 2007.
- [33] S. A. Hubbard, D. M. McFarland, L. A. Bergman, and A. F. Vakakis, “Targeted energy transfer between a model flexible wing and nonlinear energy sink,” *Journal of Aircraft*, vol. 47, no. 6, pp. 1918 – 1931, 2010.
- [34] W. Johnson, *Helicopter Theory*. Dover New York, 1980.
- [35] J. D. Keller, R. M. McKillip Jr, and S. Kim, “Aircraft flight envelope determination using upset detection and physical modeling methods,” in *Proc. AIAA Atmospheric Flight Mechanics Conference, Hilton Head, SC*, 2009, AIAA Paper 2009–6259.
- [36] J. D. Keller, R. M. McKillip Jr, and D. A. Wachspress, “Physical modeling of aircraft upsets for real-time simulation applications,” in *Proc. AIAA Atmospheric Flight Mechanics Conference, Honolulu, HI*, 2008, AIAA Paper 2008–6205.
- [37] H. K. Khalil, *Nonlinear Systems*, 3rd ed. Pearson Education, Upper Saddle, NJ, 2000.
- [38] M. Krstic, B.-Z. Guo, A. Balogh, and A. Smyshlyaev, “Control of a tip-force destabilized shear beam by observer-based boundary feedback,” *SIAM Journal of Control and Optimization*, vol. 47, no. 2, pp. 553 – 574, 2008.
- [39] M. Krstic, I. Kanellakopoulos, and P. V. Kokotovic, *Nonlinear and Adaptive Control Design*. Wiley, 1995.
- [40] M. Krstic and A. Smyshlyaev, *Boundary Control of PDEs: A Course on Backstepping Designs*. Advances in Design and Control, SIAM, 2008.
- [41] ——, *Adaptive Control of PDEs*. Princeton University Press, 2010.
- [42] P. D. Kuang, M. Dorothy, and S.-J. Chung, “Robobat: Dynamics and control of a robotic bat flapping flying testbed,” in *AIAA Infotech at Aerospace Conference, St. Louis, MO*, 2011, AIAA Paper 2011–1435.
- [43] A. M. Kuethe and C.-Y. Chow, *Foundations of Aerodynamics*, 4th ed. John Wiley, NY, 1986.
- [44] R. F. Larijani and J. D. DeLaurier, *A Nonlinear Aeroelastic Model for the Study of Flapping Wing Flight*. AIAA, 2001, pp. 399 – 428.

- [45] R. K. Liefer, J. Valasek, D. P. Eggold, and D. R. Downing, “Fighter agility metrics, research and test,” *Journal of Aircraft*, vol. 29, no. 3, pp. 452 – 457, 1992.
- [46] W. Lohmiller and J. J. E. Slotine, “Contraction analysis of nonlinear distributed systems,” *International Journal of Control*, vol. 78, no. 9, pp. 678 – 688, 2005.
- [47] M. Lowenberg, *Bifurcation and Continuation Method*. Springer-Verlag, 2002, pp. 88 – 106.
- [48] B. W. McCormick, *Aerodynamics, Aeronautics and Flight Mechanics*, 2nd ed. Wiley, 1994.
- [49] O. J. McMillan, R. G. Schwind, J. N. Nielsen, and M. F. E. Dillenius, “Rolling moments in a trailing vortex flow field,” NEAR TR 129, also NASA CR-151961, 1977.
- [50] L. Meirovitch and H. Baruh, “On the problem of observation spillover in self-adjoint distributed-parameter systems,” *Journal of Optimization and Applications*, vol. 39, no. 2, pp. 269 – 291, 1983.
- [51] L. Meirovitch and I. Tuzcu, “Unified theory for the dynamics and control of maneuvering flexible aircraft,” *AIAA Journal*, vol. 42, no. 4, pp. 714 – 727, 2004.
- [52] C. C. Merrett and H. H. Hilton, “Influences of starting transients, aerodynamic definitions and boundary conditions on elastic and viscoelastic wing and panel flutter,” *Mathematics in Engineering, Science and Aerospace*, vol. 2, no. 2, pp. 121 – 144, 2011.
- [53] T. J. Mueller, *Fixed and Flapping Wing Aerodynamics for Micro Air Vehicle Applications*, ser. Progress in Aeronautics and Astronautics. American Institute of Aeronautics and Astronautics (AIAA) Reston VA, 2001, no. 195.
- [54] N. Nguyen and I. Tuzcu, “Flight dynamics of flexible aircraft with aeroelastic and inertial force interactions,” in *Proc. AIAA Atmospheric Flight Mechanics Conference, Chicago, IL*, 2009, AIAA Paper 2009–6045.
- [55] B. Obradovic and K. Subbarao, “Modeling of dynamic loading of morphing wing aircraft,” in *Proc. AIAA Atmospheric Flight Mechanics Conference 2010, Toronto, ON, Canada*, 2010, AIAA Paper 2010–8236.
- [56] M. Ol, G. Parker, G. Abate, and J. Evers, “Flight controls and performance challenges for MAVs in complex environments,” in *Proc. AIAA Guidance, Navigation and Control Conference, Honolulu, HI*, 2008, AIAA Paper 2008–6508.
- [57] B. N. Pamadi, *Performance, Stability, Dynamics, and Control of Airplanes*, ser. AIAA Education Series. AIAA Reston VA, 1998.
- [58] B. N. Pamadi and L. W. Taylor Jr, “Estimation of aerodynamic forces and moments on a steadily spinning airplane,” *Journal of Aircraft*, vol. 21, no. 2, pp. 943 – 954, 1984.
- [59] A. Paranjape, E. Xargay, N. Hovakimyan, and C. Cao, “Adaptive controller for nonlinear strict feedback systems,” in *Proceedings of Mediterranean Conference on Control and Automation, Thessaloniki, Greece*, 2009, pp. 229–234.
- [60] A. A. Paranjape and N. Ananthkrishnan, “Aircraft level turn performance, including stability constraints, using EBAC method,” in *Proc. AIAA Atmospheric Flight Mechanics Conference, San Francisco, CA*, 2005, AIAA Paper 2005–5898.

- [61] ——, “Combat aircraft agility metrics - a review,” *Journal of Aerospace Sciences and Technologies*, vol. 58, no. 2, pp. 1 – 16, 2006.
- [62] A. A. Paranjape and S.-J. Chung, “Flight mechanics of a tailless articulated wing aircraft,” in *Proc. AIAA Atmospheric Flight Mechanics Conference, Toronto, Ontario, Canada*, 2010, AIAA Paper 2010–7633.
- [63] A. A. Paranjape, S.-J. Chung, H. H. Hilton, and A. Chakravarthy, “Dynamics and performance of a tailless MAV with flexible articulated wings,” *AIAA Journal*, 2011, to appear.
- [64] A. A. Paranjape, S.-J. Chung, and M. Krstic, “PDE boundary control for flexible articulated wings on a robotic aircraft,” *IEEE Transactions on Robotics*, 2011, in review, also available as AIAA Paper 2011–6486.
- [65] A. A. Paranjape, S.-J. Chung, and M. S. Selig, “Flight mechanics of a tailless articulated wing aircraft,” *Bioinspiration & Biomimetics*, vol. 6, no. 2, 2011.
- [66] A. A. Paranjape, J. Kim, N. Gandhi, and S.-J. Chung, “Experimental demonstration of perching by a tailless articulated wing MAV,” in *Proc. AIAA Guidance Navigation and Control Conference 2011, Portland, OR*, 2011, AIAA Paper 2011–6486.
- [67] A. A. Paranjape, N. K. Sinha, and N. Ananthkrishnan, “Use of bifurcation and continuation methods for aircraft trim and stability analysis - a state-of-the-art,” *Journal of Aerospace Sciences and Technologies*, vol. 60, no. 2, pp. 1 – 12, 2008.
- [68] V. Patel, C. Cao, N. Hovakimyan, K. Wise, and E. Lavretsky, “ \mathcal{L}_1 adaptive controller for tailless unstable aircraft in the presence of unknown actuator failures,” *International Journal of Control*, vol. 82, no. 4, pp. 705 – 720, 2009.
- [69] M. J. Patil and D. H. Hodges, “Flight dynamics of highly flexible flying wings,” *Journal of Aircraft*, vol. 43, no. 6, pp. 1790 – 1798, 2006.
- [70] D. A. Peters, S. Karunamoorthy, and W. M. Cao, “Finite state induced flow models part I: Two-dimensional thin airfoil,” *Journal of Aircraft*, vol. 32, no. 2, pp. 313 – 322, 1995.
- [71] A. P. Poppen Jr, “A method for estimating the rolling moment due to spin rate for arbitrary planform wings,” NASA TM-86365, 1985.
- [72] M. D. Queiroz, D. M. Dawson, M. Agarwal, and F. Zhang, “Adaptive nonlinear boundary control of a flexible link robotic arm,” *IEEE Trans. Robotics and Automation*, vol. 15, no. 4, pp. 779–787, 1999.
- [73] B. Raghavan and M. J. Patil, “Flight dynamics of high-aspect-ratio flying wings: Effect of large trim deformation,” *Journal of Aircraft*, vol. 46, no. 5, pp. 1808 – 1812, 2009.
- [74] ——, “Flight control for flexible, high-aspect-ratio flying wings,” *Journal of Guidance, Control, and Dynamics*, vol. 33, no. 1, pp. 64 – 74, 2010.
- [75] P. K. Raghavendra, T. Sahai, P. A. Kumar, M. Chauhan, and N. Ananthkrishnan, “Aircraft spin recovery, with and without thrust vectoring, using nonlinear dynamic inversion,” *Journal of Aircraft*, vol. 42, no. 6, pp. 1492 – 1503, 2005.

- [76] M. Rais-Rohani, R. T. Haftka, B. Grossman, and E. R. Unger, “Integrated aerodynamic-structural-control wing design,” *Computing Systems in Engineering*, vol. 3, no. 6, pp. 639 – 650, 1992.
- [77] J. A. Ramsey, R. T. Ratliff, K. A. Wise, and E. Lavretsky, “Departure resilient control for autonomous air vehicles,” in *Proc. 2009 American Control Conference, St. Louis, MO*, 2009, pp. 5386 – 5391.
- [78] G. W. Reich, O. Wojnar, and R. Albertani, “Aerodynamic performance of a notional perching MAV design,” in *Proc. AIAA Aerospace Sciences Meeting and Exhibit, Orlando, FL*, 2009, AIAA Paper 2009–63.
- [79] W. P. Rodden, “Dihedral effect of a flexible wing,” *Journal of Aircraft*, vol. 2, no. 5, pp. 368 – 373, 1965.
- [80] D. L. Russell, “Controllability and stabilizability theory for linear partial differential equations: Recent progress and open questions,” *SIAM Review*, vol. 20, no. 4, pp. 639 – 739, 1978.
- [81] G. Sachs, “What can be learned from unique lateral-directional dynamics properties of birds for mini-aircraft,” in *Proc. AIAA Atmospheric Flight Mechanics Conference 2007, Hilton Head, SC*, 2007, AIAA Paper 2007–6311.
- [82] ———, “Why birds and miniscale airplanes need no vertical tail,” *Journal of Aircraft*, vol. 44, no. 4, pp. 1159 – 1167, 2007.
- [83] G. Sachs and F. Holzapfel, “Flight mechanic and aerodynamic aspects of extremely large dihedral in birds,” in *Proc. AIAA Aerospace Sciences Meeting and Exhibit 2007, Reno, NV*, 2007, AIAA Paper 2007–46.
- [84] D. Salamon, “Realization theory in hilbert space,” *Mathematical Systems Theory*, vol. 21, pp. 147 – 164, 1989.
- [85] H. Sano, “Output tracking control of a parallel-flow heat exchange process,” *Systems and Control Letters*, vol. 60, no. 11, pp. 917 – 921, 2011.
- [86] M. S. Selig, “Modeling full-envelope aerodynamics of small UAVs in realtime,” in *Proc. AIAA Atmospheric Flight Mechanics Conference, Toronto, ON, Canada*, 2010, AIAA Paper 2010–7635.
- [87] ———, “Modeling propeller aerodynamics and slipstream effects on small UAVs in realtime,” in *Proc. AIAA Atmospheric Flight Mechanics Conference, Toronto, ON, Canada*, 2010, AIAA Paper 2010–7938.
- [88] L. F. Shampine, M. W. Reichelt, and J. Kierzenka, “Solving boundary value problems for ordinary differential equations with `bvp4c`,” available from <http://www.mathworks.com/bvp-tutorial>.
- [89] C. M. Shearer and C. E. S. Cesnik, “Nonlinear flight dynamics of very flexible aircraft,” *Journal of Aircraft*, vol. 44, no. 5, pp. 1528 – 1545, 2007.

- [90] Y. Shtessel, J. Buffington, and S. Banda, “Tailless aircraft flight control using multiple time scale reconfigurable sliding modes,” *IEEE Trans. Control Systems Technology*, vol. 10, no. 2, pp. 288 – 296, 2002.
- [91] W. Shyy, H. Aono, S. K. Chimakurthi, P. Trizila, C.-K. Kang, C. E. S. Cesnik, and H. Liu, “Recent progress in flapping wing aerodynamics and aeroelasticity,” *Progress in Aerospace Sciences*, vol. 46, pp. 284 – 327, 2010.
- [92] A. A. Siranosian, M. Krstic, A. Smyshlyaev, and M. Bememt, “Gain scheduling-inspired boundary control for nonlinear partial differential equations,” *Journal of Dynamic Systems, Measurement, and Control*, vol. 133, no. 051007, 2011.
- [93] S. A. Snell, D. F. Enns, and W. L. G. Jr, “Nonlinear inversion flight control for a supermaneuverable aircraft,” *Journal of Guidance, Control, and Dynamics*, vol. 15, no. 4, pp. 976 – 984, 1992.
- [94] A. Song, X. D. Tian, E. Israeli, R. Galvao, K. Bishop, S. Swartz, and K. Breuer, “Aeromechanics of membrane wings with implications for animal flight,” *AIAA Journal*, vol. 46, no. 8, pp. 2096 – 2106, 2008.
- [95] G. Stenfelt and U. Ringertz, “Lateral stability and control of a tailless aircraft configuration,” *Journal of Aircraft*, vol. 46, no. 6, pp. 2161 – 2163, 2009.
- [96] ——, “Yaw control of a tailless aircraft configuration,” *Journal of Aircraft*, vol. 47, no. 5, pp. 1807 – 1810, 2010.
- [97] R. H. Stone, “Aerodynamic modeling of the wing-propeller interaction for a tail-sitter unmanned air vehicle,” *Journal of Aircraft*, vol. 45, no. 1, pp. 198 – 210, 2008.
- [98] W. Su and C. E. S. Cesnik, “Nonlinear aeroelasticity of a very flexible blended-wing-body aircraft,” *Journal of Aircraft*, vol. 47, no. 5, pp. 1539 – 1553, 2010.
- [99] T. Theodorsen, “General theory of aerodynamic instability and the mechanism of flutter,” NACA Report 496, 1935.
- [100] A. L. R. Thomas and G. K. Taylor, “Animal flight dynamics i. stability in gliding flight,” *Journal of Theoretical Biology*, vol. 212, pp. 399 – 424, 2001.
- [101] D. T. Tran and R. Lind, “Parameterizing stability derivatives and flight dynamics with wing deformation,” in *AIAA Atmospheric Flight Mechanics Conference 2010*, 2010, AIAA Paper 2010–8227.
- [102] D. Uhlig, A. Sareen, P. Sukumar, A. Rao, and M. S. Selig, “Determining aerodynamic characteristics of a micro air vehicle using motion tracking,” in *Proc. AIAA Atmospheric Flight Mechanics Conference, Toronto, ON, Canada*, 2010, AIAA Paper 2010–8416.
- [103] M. W. Vandegrift, F. L. Lewis, and S. Q. Zhu, “Flexible-link robot arm control by a feedback linearization/singular perturbation approach,” *Journal of Robotic Systems*, vol. 11, no. 7, pp. 591 – 603, 1994.
- [104] R. Vazquez and M. Krstic, “A closed-form feedback controller for stabilization of the linearized 2-D Navier-Stokes Poiseuille system,” *IEEE Transactions on Automatic Control*, vol. 52, no. 12, pp. 2298 – 2312, 2007.

- [105] Q. Wang and R. F. Stengel, “Robust nonlinear flight control of a high-performance aircraft,” *IEEE Trans. Control Systems Technology*, vol. 13, no. 1, pp. 15 – 26, 2005.
- [106] M. R. Waszak and D. K. Schmidt, “Flight dynamics of aeroelastic vehicles,” *Journal of Aircraft*, vol. 25, no. 6, pp. 563 – 571, 1988.
- [107] A. Wickenheiser and E. Garcia, “Longitudinal dynamics of a perching aircraft,” *Journal of Aircraft*, vol. 43, no. 5, pp. 1386 – 1392, 2006.
- [108] ———, “Optimization of perching maneuvers through vehicle morphing,” *Journal of Guidance, Control and Dynamics*, vol. 31, no. 4, pp. 815 – 823, 2008.
- [109] R. J. Wood, “The first takeoff of a biologically inspired at-scale robotic insect,” *IEEE Transactions on Robotics*, vol. 24, no. 2, pp. 341 – 347, 2008.
- [110] J. R. Wright and J. E. Cooper, *Introduction to Aircraft Aeroelasticity and Loads*, ser. Aerospace Series. John Wiley & Sons, England, 2007.